CORA Cork Open Research Archive
Cartlann Taighde Oscailte Chorcaí

Title	Remote powering and signalling using photovoltaic power converter and reflective electroabsorption modulator
Authors	Baskaran, Meena
Publication date	2026-01-06
Original Citation	Baskaran, M. 2026. Remote powering and signalling using photovoltaic power converter and reflective electroabsorption modulator. PhD Thesis, University College Cork.
Type of publication	Doctoral thesis
Rights	© 2026, Meena Baskaran. - https://creativecommons.org/licenses/by-nc-nd/4.0/
Download date	2026-11-15 11:37:43
Item downloaded from	https://hdl.handle.net/10468/19270

UCC
University College Cork, Ireland
Coláiste na hOllscoile Corcaigh

Remote powering and signalling using photovoltaic power converter and reflective electroabsorption modulator

Meena Baskaran



Thesis submitted in partial fulfilment of the requirements
of the degree of Doctor of Philosophy

at the
Department of Engineering Science,
University College Cork,
National University of Ireland

Supervisor: Brian Corbett
Co-supervisor: Brendan Roycroft
Head of Department: Fatima Gunning

January 2026

Contents

List of Figures iv

List of Tables x

List of Acronyms xi

List of Symbols . . . xiv

List of Publications xvi

Declaration of Authorship xviii

Acknowledgements xx

Dedication xxi

1 Introduction 1

1.1 Motivation . . . 1

1.2 Power over fiber technology . . . 3

1.2.1 High power laser source . . . 4

1.2.2 Optical fiber . . . 4

1.2.3 Photovoltaic power converter (PPC) . . . 5

1.2.3.1 Material characteristics and reported efficiencies . . . 6

1.2.3.2 Series-Connection Strategies for High-Voltage Output . . . 6

1.2.3.3 Recent performance of series connected PPC . . . 7

1.3 Power and data over fiber technology . . . 8

1.4 Thesis Objective . . . 11

1.5 Thesis Outline . . . 14

2 Experimental study on photovoltaic power converter in edge coupled configuration 16

2.1 Introduction . . . 16

2.2 Edge coupling configuration . . . 17

2.2.1 PPC parameter . . . 19

2.3 Single junction edge coupled PPC . . . 22

2.3.1 Edge coupling between 1480 nm to 1540 nm receiver laser . . . 22

2.3.2 Results and discussion . . . 23

2.3.2.1 PV characteristics . . . 23

2.3.3 Receiver PPC lasing under optical pumping . . . 26

2.3.3.1 Remote Data Transmission . . . 28

2.3.4 Edge coupling between 980 nm to 1064 nm device . . . 30
2.3.5 Result and discussion . . . 31
2.3.5.1 I–V characterization of on chip LPC . . . 31
2.4 Edge coupling between 850 nm to 905 nm device triple junction PPC . . . 34
2.4.1 Result and discussion . . . 35
2.4.1.1 I–V characterization of the triple junction LPC . . . 35
2.5 Conclusion and Discussion . . . 41

3 Surface normal photovoltaic power converter under annular and quasi-Gaussian illumination 43
3.1 Introduction . . . 43
3.2 Surface normal configuration on PPC . . . 45
3.2.1 Device Description . . . 47
3.2.2 Optical losses in segmented PPC . . . 48
3.2.3 Fiber to device distance determination . . . 49
3.3 Experimental design on quasi-Gaussian and annular illumination on four segment PPC . . . 50
3.3.1 Generation of Annular Illumination . . . 51
3.3.2 Beam Characterization and Calibration . . . 53
3.3.3 Quasi-Gaussian and annular beam analysis . . . 54
3.3.4 Distance-Dependent Illumination Performance on Chip 1 . . . 57
3.3.4.1 I–V characteristics . . . 57
3.3.4.2 Analysis of open-circuit voltage and short circuit current . . . 58
3.3.4.3 Voltage at maximum power point V_{max} . . . 60
3.3.4.4 Efficiency and fill factor . . . 61
3.4 Validation and extended-distance analysis using chip 2 . . . 62
3.4.1 Beam characterization and illumination analysis on chip 2 . . . 63
3.4.2 Distance-dependence on-chip beam confinement . . . 65
3.5 PV response of chip 2 under quasi-Gaussian and annular illumination . . . 66
3.5.1 I_{sc} Dependence on Fiber-to-Device Distance . . . 66
3.5.2 Open circuit and maximum operating condition of Chip 2 . . . 68
3.5.3 Distance and illumination dependent η and FF performance of Chip 2 . . . 69
3.6 Conclusion and Discussion . . . 71

4 Remote signalling using transfer printed electroabsorption modulator on a reflector 74
4.1 Introduction . . . 74
4.2 Principles of SNEAM Operation and State of the Art . . . 75
4.2.1 Asymmetric FP Reflection operation in SNEAM . . . 77
4.3 Reflective SNEAM device design . . . 79
4.3.1 SNEAM device design . . . 80
4.3.2 Asymmetric FP Cavity Design . . . 80
4.4 Fabrication of Asymmetric FP SNEAM Devices . . . 83
4.4.1 Source fabrication . . . 83
4.4.2 Target fabrication . . . 83
4.4.3 Micro transfer printing . . . 84
4.5 Result and discussion . . . 86

4.5.1 Photoabsorption response . . . 86
4.5.2 Reflection spectrum . . . 87
4.5.3 Capacitance-voltage measurements . . . 90
4.5.4 SNEAM electro-optic response . . . 91
4.5.5 Eye diagram analysis of the modulated signal . . . 94
4.6 Conclusion and discussion . . . 95

5 Conclusions and future work **98**
5.1 Overview of the results . . . 99
5.2 Future Work . . . 101

A Appendix **109**
A.1 Python Code for Gaussian Power Distribution Analysis . . . 109
A.2 SPICE analysis of series junction current limitation . . . 113
A.3 Epitaxial details and layout of the four-segment PPC . . . 114
A.4 Camera specification . . . 114
A.5 Single junction micro PPC in surface normal illumination . . . 115
A.6 Image Analysis and Intensity Quantification Algorithms . . . 116
A.6.1 Two-Dimensional Gaussian Beam Fits . . . 116
A.6.2 Radial Ridge Extraction and Circle Fitting . . . 118
A.6.3 Intensity Outside a Fixed Physical Radius . . . 120
A.6.4 Bootstrap Estimation of Uncertainty . . . 121
A.7 Cavity simulation parameter . . . 123
A.8 Epitaxial layer details of EAM . . . 125

B Appendix **126**
B.1 Per-layer mask design of source . . . 126
B.2 SNEAM source with tether design . . . 127
B.3 Complete source GDS mask overview . . . 128
B.4 GDS mask of target fabrication . . . 129
B.5 Source mask design aligned to target pattern . . . 130

Bibliography **131**

List of Figures

1.1 Schematic illustration of cross-section of optical fibers used in POF application. (a) SMF, (b) MMF, (c) MCF and (d) DCF. 5
1.2 Schematic illustration of the POF system. 9
1.3 (a) Schematic of an optically powered microcamera system in which a surface-normal illuminated MMF delivers optical power to four laterally series-connected PV cell that electrically supply the microcamera. The PPC chip has a 250 µm active diameter within a 1 mm × 1 mm chip; the inset shows the illumination fiber attached to the PPC device. (b) Picture of a 2 mm outer-diameter optically powered chip-on-tip positioned over a tissue phantom.(c) Microcamera image showing a 1 mm-scale feature in the tissue phantom [55]. 12

2.1 Schematic of the waveguide receiver laser operating as a photovoltaic (PV) converter, where incident optical power P_{illum} is absorbed in the MQW region generates carriers that produce a photocurrent I_{ph} driving an external load. 18
2.2 Schematic I–V characteristic of a PV device under illumination, shown by the red curve. The maximum power point, indicated by P_{max}, is used to calculate η and FF. 20
2.3 (a) Schematic of laser-to-laser power conversion through edge coupling using a SMF. (b) Experimental setup showing both lasers in packaged form, where the pump laser optically pumps the receiver laser and the resulting electrical current is measured using mini hook test leads connected to the receiver laser anode and cathode. 23
2.4 (a) I–V characterization of edge coupled waveguide PPC under no optical incident illumination (black curve-top) and with variation of absorbed optical power from 6.4 mW (red- top second curve) to 70 mW (bright-green-bottom). (b) Variation of V_{oc} and I_{sc} as a function of absorbed optical power, showing the logarithmic increase of V_{oc} and the linear dependence of I_{sc} with optical power. 24
2.5 (a) Output P-V characteristics of the receiver laser PPC under different absorbed optical powers from 6.4 mW (red-top) to 70 mW (bright-green-bottom). (b) Variation of η and FF as a function of absorbed optical power, showing a gradual decrease at higher optical injection due to carrier density dependent effects. . . 25
2.6 Schematic of the receiver laser PPC setup used to characterize lasing behavior under optical pumping through an optical circulator. Black lines indicate electrical connections, and yellow lines represent SM optical fibers. 26
2.7 Emission spectrum of receiver laser near 1540 nm under zero bias and reverse bias condition with optically pumped by 1427 nm (a) 0 mA (b) -10 mA (c) -20 mA and (d) -30 mA. 27

2.8 (a) Plot of the inverse differential current $\frac{1}{dI}$ versus current for absorbed optical powers ranging from 0 mW (no pumping) to 70 mW The curves are colour-coded from black (right) to light green (left), indicating increasing absorbed optical power. (b) Threshold current (I_{th}) as a function of absorbed optical power. 28
2.9 Schematic of the experimental setup for optical pumping and data modulation of the receiver laser using a pulse pattern generator through an optical circulator, demonstrating upstream data transmission operation. Black lines indicate electrical connections, and yellow lines represent SM optical fibers. 29
2.10 Data transmission from the receiver laser. (a) Detected 100 Mbps modulated signals from the receiver laser under varying absorbed optical powers, showing modulation onset above 40 mW. Eye diagrams of the received signal at varying data rates, illustrating the transition from a wide-open eye at lower bit rates (b) 100 Mbps and partially closed eye at higher bit rates (c) 500 Mbps. (d) Bit error rate (BER) plotted as a function of data rate, showing stable data transmission 200 Mbps to 300 Mbps. 30
2.11 Experimental setup for optical power transfer using an edge-coupled waveguide laser receiver. A SMF–coupled pump laser is focused onto the receiver facet through a tapered lensed fiber mounted on an XYZ stage. The absorbed optical power generates photocurrent across the device terminals. Insets show the bare chip (top right) and needle probe placed on the chip indicating polarity (bottom right). 31
2.12 (a) I–V and (b) P-V characteristics of the 1060 nm waveguide laser operating as a PPC under different levels of incident optical power. The curves show the transition from dark to illuminated conditions, with photocurrent and output electrical power increasing proportionally with optical intensity. The curves are colour-coded from black (top) to olive-green (bottom), corresponding to incident optical powers ranging from 0 to 74 mW, obtained from pump power steps of 10 mW after normalization. 32
2.13 (a) Variation of of the 1060 nm single-junction PPC with incident optical power. (a) V_{oc} and I_{sc} showing a steady increase with illumination. (b) η and FF, with peak values of 23% and 70% at 10 mW, respectively. FF error bars denote the propagated I–V uncertainty used in the FF extraction, assuming 1.5% current and 0.5% voltage uncertainty, corresponding to a relative FF uncertainty of 2.24%. The slight FF increase near 40 mW lies within this uncertainty and is attributed to coupling fluctuations. 33
2.14 (a) Experimental setup for optical power transfer using an 850 nm pump laser and a 905 nm triple-junction waveguide receiver. The fiber-coupled pump laser is collimated (focal length f = 8.1 mm; spot size = 1.74 mm) and focused onto the receiver facet through a lens (f = 3.1 mm; spot size = 5 µm) in an edge-coupled configuration. The inset shows the packaged 905 nm triple-junction receiver diode. 34
2.15 (a) I–V characteristics of the 905 nm triple-junction waveguide PPC under varying incident optical power from 9.4 mW (top curve) to 65.8 mW (bottom curve), showing increased photocurrent with illumination. Variations in the curves arise from optical coupling instability during measurement. (b) Variation of V_{oc} V_{mpp} with incident optical power, demonstrating voltage multiplication from the three series-connected p–n junctions and a maximum output of 3.1 V at 9.4 mW. . . 35
2.16 Efficiency of the triple-junction waveguide receiver plotted as a function of incident optical power. 36

2.17 Numerical analysis of Gaussian beam coupling to a triple p–n junction waveguide receiver. (a–d) Simulated spatial intensity distributions at the receiver facet for increasing Gaussian beam waist values (w = 4, 6, 8, and 10 µm), together with the corresponding fraction of optical power incident on each segment of the p–n junction stack within the 10 µm-high waveguide. 37
2.18 Calculated power transfer efficiency as a function of Gaussian beam waist, showing an optimum efficiency of approximately 72% at $w \approx 6$ μm due to the balance between junction current matching and optical spillover losses. 38

3.1 (a) Cross-sectional schematic of a laterally segmented, surface-normal GaAs PPC, showing the vertical layer structure, isolation trench with SiN for encapsulation, series interconnection metal, and anode and cathode contacts under surface-normal laser illumination. (b) Front view of the circular four-segment laterally connected PPC showing the device layout with isolation trenches (black cross lines) and metal connections; the red arrow indicates the device active diameter. 46
3.2 (a) Picture of 1 mm × 1 mm chip with four segments laterally interconnected PPC with active diameter of 350 µm. 47
3.3 Schematic of the surface-normal illumination geometry showing the fiber-to-device distance (G). The emitted beam diverges from the fiber core at an angle θ, expanding to a diameter D_{sample} that defines the illuminated area on the PPC surface. 49
3.4 Experimental setup for annular beam illumination on the PPC. SMF; Single mode fiber coupled laser, L1 collimator focal length= 18.4 mm, L2 Biconvex lens focal length= 25 mm, DCF; double clad fiber (DCF-13 Thorlabs).The inserted picture shows diced chip under annular illumination at a fiber to device distance of 600 µm, recorded using a Dino-Eye Edge digital microscope (AM4025X model). 52
3.5 One-dimensional line scans along the x and y direction through the center of the quasi-Gaussian beam recorded on a diffusive imaging surface at a fiber to imaging plane distance of 600 µm. The profiles show a centrally peaked, Gaussian-like intensity distribution with superimposed fluctuations arising from multimode speckle. 55
3.6 Normalized two-dimensional intensity distributions of the beams recorded at fiber-to-device distances of 400 µm, 500 µm, and 600 µm (left to right), with a 350 µm circular disk overlaid to represent the PPC active area. Each panel corresponds to an independently acquired beam image at the indicated fiber-to-device distance. (a) Quasi-Gaussian beam. (b) Annular beam. 56
3.7 Comparison of the I–V characteristics of the 350 µm diameter four-segment PPC under Gaussian and annular illumination at 851 nm, measured for varying DCF output power levels (P_{illum}) from 0 mW to 60 mW at a fiber-to-device separation of 600 µm. 58
3.8 Comparison of quasi-Gaussian and annular beam illumination on the four segment PPC at fiber to device separations of 400 µm, 500 µm, and 600 µm for varying incident optical powers: (a) V_{oc} and (b) I_{sc}. 59
3.9 Voltage at the maximum power point V_{max} of the four-segment PPC under quasi-Gaussian and annular beam illumination at an incident power of 60 mW. Measurements were performed for fiber to device separations of 600 µm, 500 µm, and 400 µm. The annular illumination exhibits a higher V_{max} 4.18 V at 60 mW of incident power. 61

3.10 Variation of power conversion efficiency η and FF with incident optical power for the four segment PPC under annular and quasi-Gaussian illumination at fiber to device separations of (a) 400 µm, (b) 500 µm and (c) 600 µm. 62
3.11 Quasi-Gaussian beam intensity distributions overlapped with a 350 µm circular disk representing the PPC active region, plotted for fiber-to-device distances ranging from 0.4 mm to 2 mm. 64
3.12 Annular beam intensity distributions overlapped with a 350 µm circular disk representing the PPC active region, plotted for fiber-to-device distances ranging from 0.4 mm, 0.5 mm and 0.6 mm. 64
3.13 Illumination on the four segment GaAs PPC captured at a 45 degrees angle under quasi-Gaussian illumination for varying fiber-to-device distances. 66
3.14 Annular beam illumination on the four segment GaAs PPC device captured at a 45 degrees angle for fiber to device distances of 0.4 mm, 0.5 mm, and 0.6 mm (images shown from left to right). 66
3.15 Variation of I_{sc} of Chip 2 as a function of fiber-to-device distance for incident optical powers ranging from 10 mW to 60 mW. The I_{sc} values under annular beam illumination are shown in black (dashed trace), while those under quasi-Gaussian illumination are shown in red (solid trace). 67
3.16 (a) V_{oc} and (b) V_{max} as functions of incident optical power for different fiber-to-device distances under quasi-Gaussian and annular illumination. 68
3.17 PV characteristics of the four-segment, 350 µm active diameter PPC, measured at the fiber-to-device separations corresponding to maximum power extraction for each illumination profile. Solid lines correspond to annular illumination at a distance of 0.4 mm, while dashed lines represent quasi-Gaussian illumination at a distance of 1 mm. Curve colour denotes the incident optical power, varied from 10 to 60 mW (bottom to top curve). 69
3.18 η and FF of chip 2 as a function of incident optical power under quasi-Gaussian and annular illumination for fiber to device distances of 1 mm and 0.4 mm, respectively. The results highlight that the device exhibits peak performance at these distances for each illumination condition. 70
3.19 η plotted as a function of incident optical power for fiber to device distance of 0.6 mm to 1.2 mm under quasi-Gaussian illumination on Chip 2. 71

4.1 (a) Band diagrams illustrating the electron and hole wavefunction in a single QW, under no bias and reverse condition. (b) Schematic absorption spectra showing the QCSE-induced redshift and reduction of the excitonic peak under reverse bias, with λ_{op} indicating the wavelength of maximum modulation. (c) Schematic of surface normal EAM under transmission design. 76
4.2 Schematic illustration of light reflection in the asymmetric Fabry–Perot operation of SNEAM. The top reflection R_t exhibits a 180-degree phase shift, and the bottom reflection R_b, after passing through the cavity, ideally returns with an opposite phase and an amplitude comparable to R_b, enabling destructive interference in the reflected signal. 78
4.3 (a) Schematic of asymmetric FP resonance in the SNEAM device, (b) The simulated cavity response plotted for comparing reflection intensity with increase in reverse bias. 81

4.4 Thin-film simulation results of the multilayer PIN–BCB–SiN–Au structure obtained using Essential Macleod. (a) Reflectance spectra showing the variation in reflectance minimum for quarter-wavelength (195 nm) and half-wavelength (390 nm) SiN thicknesses at a fixed BCB thickness of 90 nm, highlighting the resonance near 1560 nm. (b) Spectral reflectance as a function of wavelength for different BCB thicknesses with the SiN thickness fixed at 390 nm. 82
4.5 Overview of the fabrication process flow for the source wafer. 84
4.6 (a) Microscope image of the transferred coupon on the target wafer prior to GSG pad metallization, showing the alignment accuracy. (b) Schematic illustration of the printed device on the target wafer following completion of the GSG pad metallization. 85
4.7 EAM device with an active diameter of 30 µm printed onto the target wafer: (a) Scanning electron microscope (SEM) image of the device following bondpad metallization on the transferred coupon. (b) Microscope image of the completed device showing the GSG pad configuration. 85
4.8 (a) The QCSE effect of SNEAM with presence of asymmetric FP condition. Voltage induced exciton shift tested for 30 µm diameter device and (b) Exciton wavelength shift versus reverse bias applied to the device. 87
4.9 (a) Schematic of reflection experimental setup for the SNEAM device. The inset shows the fibre aligned device during testing. (b) Experimental setup showing a single-mode fiber aligned surface normal to the top surface of the device under test (DUT), which is probed using a GSG probe. 88
4.10 SEM image of the 30 µm SNEAM device. The active area is surrounded by a circular P-metal ring, which defines the optical access aperture relevant to fibre alignment during measurement. 89
4.11 ((a) Normalized reflection spectra of the 30 µm active diameter device SNEAM device measured at reverse biases of -1 V, -5 V and -7 V, (b) Transfer characteristic showing the normalized reflected power as a function of applied reverse bias for the same device. 89
4.12 (a) C-V measurement for a variation of active diameter and (b) Effect of mesa-to-n-contact spacing on the capacitance of a 30 µm active diameter device, comparing spacings of 2 µm and 3 µm. 91
4.13 Schematic of experimental setup for electro-optic measurement. 92
4.14 Normalized electro-optic bandwidth S_{21} of SNEAM devices measured for (a) 20 µm and 30 µm active diameters at -5 V bias, and (b) a 30 µm active diameter at -3 V and -5 V bias. 93
4.15 (a) Schematic of Eye diagram measurement and (b) The SNEAM device modulated with NRZ-OOK signal at 1 Gbps. 95

5.1 Layout showing the centrally positioned SNEAM with 30 µm on four segmented PPC with 350 µm. 102
5.2 Schematic of single fiber solution using a DCF and a DC1300LQ2FA 2 × 1 DCF coupler to simultaneously launch 850 nm annular illumination into the inner cladding and support bidirectional 1550 nm signal transmission through the single mode core of DCF-13. 104
5.3 Power ratios calculated from raw annular beam images using background corrected integrated intensities extracted in ImageJ for a 350 µm diameter annular beam on a diffuse target. The highlighted rectangle indicates (a) the annular beam and background region and (b) 30 µm wide region used to estimate the fraction of optical power present at the beam center. 105

5.4 Block diagram illustrating the voltage distribution through the power management integrated circuit (PMIC) to the various system components, highlighting the supply requirements of the customized CMOS image sensor. 106
5.5 Suggested integrated layout of three single-junction PPCs (26 µm active diameter) connected in series and a central EAM (20 µm active area). (a) Detailed device-level layout adapted for MCF illumination. (b) Chip-level overview showing the overall chip dimensions 1.65 mm × 1.8 mm, including fiber ferrule and wire bonding for packaging. 107
5.6 Schematic of experimental design on MCF as single fiber solution on illumination of PPC and bidirectional single transmission. 107

A.2.1 SPICE-based circuit models and simulated I-V and P-V characteristics illustrating current limitation in series connected diode circuits. (a) single junction circuit driven by a current source with I_{ext}=100 mA, delivering of 60 mW; (b) three series connected diode circuits driven by equal current sources, resulting in voltage addition with I_{ext}=33.3 mA and unchanged output power of 60 mW; (c) three series connected diode circuits driven by unequal current sources, where I_{ext}=20 mA, leading to reduced output power of 40 mW. 113
A.3.1 Layout design of 350 µm active diameter PPC in 1 mm × 1 mm chip. 114
A.5.1 Single junction GaAs PPC performance with a 26 µm active diameter and different mesa sizes. (a) Conversion efficiency and (b) maximum output current as functions of incident optical power, measured with a fiber to device separation of 40 µm during probing. (c) Picture of SMF aligned surface normal to device with 365 µm Mesa diameter. 115

B.1.1 Seven-layer lithography mask layout used for source wafer fabrication of the SNEAM device, with panels (a)–(g) showing the sequential mask layers. Coloured regions indicate areas exposed during the corresponding lithography step, while features from previous steps are retained for reference to illustrate layer alignment. Black arrow markers denote the lateral dimensions of the mesa and coupon features. The layouts correspond to a device aperture of 30 µm. 127
B.2.1 GDS mask layouts showing coupon designs with different tether configurations used for source wafer fabrication. From (a)–(c) illustrate coupons incorporating two, four, and eight tethers, respectively. Shaded regions indicate areas exposed during lithography, while unshaded regions represent protected regions. 128
B.3.1 Complete GDS mask layout for the SNEAM source wafer, showing the arrangement of multiple device geometry. The layout incorporates devices with different active diameters, n-metal–to–mesa gaps, and tether configurations. The designed mask occupies one quarter of the source wafer. 128
B.4.1 Overview of the GDS mask layout for target-wafer fabrication. The mask includes definitions for the bottom reflector as well as GSG and GS bond pads to support multiple device testing and characterization. The designed mask occupies one quarter of the target wafer. 129
B.5.1 Alignment of a source coupon, including the PIN device layout extracted from the GDS mask, with the patterned target location, as targeted during the transfer-printing process and observed after transfer printing. 130

List of Tables

2.1 Summary of edge-coupled laser power conversion configurations investigated in this chapter. 40

3.1 Performance comparison of the four-segment, 350 µm active diameter PPC under quasi-Gaussian and annular illumination at their respective optimal fiber-device spacings. 71

5.1 Comparison of wavelength and illumination configurations for integrated PPC–SNEAM POF link. 103

A.3.1 Epitaxial layer stack for the four-segment GaAs PPC. 114
A.7.1 Intrinsic layer parameters used for the EAM epitaxial layer design and cavity simulation under zero bias. 123
A.7.2 Intrinsic layer parameters used for the EAM epitaxial layer design and cavity simulation under reverse bias of 4 V. 124
A.8.1 Epitaxial EAM stack designed for μTP [88]. 125

List of Acronyms

ASIC .....Application-specific integrated circuit

AlInAs .....Aluminium indium arsenide

AlInGaAs .....Aluminium indium gallium arsenide

BCB .....Benzocyclobutene

BERT .....Bit error rate tester

BNC .....Bayonet Neill-Concelman

BSF .....Back surface field

CMOS .....Complementary Metal-Oxide-Semiconductor

CV .....Capacitance-Voltage

DCF .....Double clad fiber

DUT .....Device under test

EAM .....Electroabsorption Modulator

EDFA .....Erbium-Doped Fiber Amplifier

FBH .....Ferdinand-Braun-Institut

FP .....Fabry–Pérot

FSF .....Front surface field

GaAs .....Gallium arsenide

GSG .....Ground-signal-ground

InGaAs .....Indium gallium arsenide

InP .....Indium phosphide

I-V .....Current-Voltage

LCL .....Lateral conduction layer

LD .....Laser diode

LED .....Light emitting diode

MCF .....Multicore fiber

MMF .....Multimode fiber

MTP .....Micro-Transfer Printing

MOCVD .....Metal Organic Chemical Vapour Deposition

MQW .....Multiple quantum well

nid .....not-intentionally doped

NRZ .....Non-Return-to-Zero

OOK .....On-Off Keying

OSA .....Optical spectrum analyzer

PCB .....Printed circuit board

PDMS .....Polydimethylsiloxane

PECVD .....Plasma-Enhanced Chemical Vapor Deposition

POF .....Power over fiber

PPC .....photovoltaic power converter

PPG .....Pulse pattern generator

PRBS .....Pseudo-random bit sequence

PR .....Photoresist

PV .....Photovoltaic

QCSE .....Quantum confined Stark effect

QW .....Quantum well

RC .....Resistance-Capacitance

RF .....Radio frequency

SMF .....Single mode fiber

Si .....Silicon

SiN .....Silicon Nitride

SEM .....Scanning Electron Microscopy

SiO_2 .....Silicon dioxide

SNEAM .....Surface normal electroabsorption modulator

SQW .....Single quantum well

VNA .....Vector network analyzer

USAF .....United States Air Force

List of Symbols

α_{eff} ..... Effective absorption coefficient

α_{mat} ..... Material absorption coefficient

Γ ..... Optical confinement factor

L_{abs} ..... Absorption length

$P_{trans}(x)$..... Optical power at position x

I ..... Output current

I_{ph} ..... Photogenerated current

I_0 ..... Diode saturation current

V ..... Voltage

V_{oc} ..... Open-circuit voltage

q ..... Elementary charge

n ..... Diode ideality factor

k ..... Boltzmann constant

T ..... Absolute temperature

ev ..... Electron Volt

P_{illum}..... Incident optical power

P_{out} ..... Electrical output power

p_{max} ..... Maximum electrical output power

V_{max} ..... Voltage at maximum power point

I_{sc} ..... Short-circuit current

η ..... Power conversion efficiency

θ ..... Beam divergence half-angle

G ..... Fiber-to-device separation

D_{core} ..... Fiber core diameter

D_{sample} ..... Beam diameter on device

r_{core} ..... Fiber core radius

r_{sample} ..... Beam radius on device

r_t ..... Top-mirror amplitude reflection coefficient

r_b ..... Bottom-mirror amplitude reflection coefficient

R_t ..... Top-mirror power reflectivity

R_b ..... Bottom-mirror power reflectivity

r_{tot} ..... Total reflected field amplitude

L ..... Cavity length

ϕ ..... Round-trip phase

f ..... Modulation frequency

f_{RC} ..... RC-limited cutoff frequency

R ..... Resistance

C ..... Capacitance

ϵ_0 ..... Permittivity of free space

A ..... Device area

d ..... Dielectric thickness

List of Publications

First author publications

1. **Meena Baskaran**, Hui Ma, Sanathana Konugolu, Brendan Roycroft, John Justice, Jérôme Garnier, Pascal Doguet, Stefan Andersson-Engels and Brian Corbett, *"Enhanced performance of segmented photovoltaic laser power converter under annular beam illumination"*, in process.

2. Asif Khan^{+}, **Meena Baskaran**$^{+}$, Owen Moynihan, James O'Callaghan, Paul Townsend and Brian Corbett,*"Half duplex transmission with asymmetric surface normal electro absorption modulator-based optical transceiver for camera-on-tip surgical endoscopes"*, in Optic Express, pp.31181–31194, 2025. DOI: 10.1364/OE.566896. $^{+}$These authors contributed equally.

Other publications

1. Brendan Roycroft, **Meena Baskaran**, David McMahon, Brian Corbett, *"Laser to laser power conversion with remote signaling"*, in Optics Express, pp.16611–16618, 2021.

2. Hasti Yavari, **Meena Baskaran**, Hui Ma, Noreen Nudds, Marc Rensing, Kamil Gradkowski, Yineng Wang, Peter O'Brien, Brian Corbett, Stefan Andersson-Engels, and

Sanathana Konugolu Venkata Sekar *"Towards all optically powered miniature devices in remote locations of the body"*, in Optics Letters, pp.1263–1266, 2026.

Conference presentation and poster

1. **Meena Baskaran**, Ava Carroll, Brendan Roycroft and Brian Corbett*, *"Optically pumped edge-emitting lasers for photovoltaics at extreme concentrations"*, European Semiconductor Laser Workshop, 2023. *Presented by a co-author.

2. **Meena Baskaran**, Hui MA, Sanathana Konugolu, Brendan Roycroft and Brian Corbett, *"Annular beam illumination on a segmented Photovoltaic laser power converter"*, IPIC, 2023.

3. **Meena Baskaran**, Brendan Roycroft, and Brian Corbett, *"Photonic Power Conversion and Direct Modulation in Edge Coupled Laser "*, Photonics Ireland, 2021.

Declaration

I, Meena Baskaran hereby declare that, unless otherwise stated, this work is my own, and that it has not been submitted for another degree, either at University College Cork or elsewhere.

Signed: Meena Baskaran

Abstract

Power-over-fiber (POF) technology is emerging as a promising alternative to conventional electrical power delivery. In remote access networks, photovoltaic power converter (PPC) and modulators are key components for enabling both power and data transfer over fiber. A POF link offers immunity to electromagnetic interference while providing reliable, high-resolution data transmission. These advantages make it particularly well-suited for integration into minimally invasive surgical endoscopes, where precise, real-time diagnostics are essential. As POF advances toward on-chip integration, careful modulator design becomes critical to complement PPC performance and maximize overall system efficiency.

In this work, we investigated remote powering techniques and designed a reflective surface-normal electroabsorption modulator (SNEAM) specifically for integration into distal-end imaging surgical endoscopy tool, enabling both power delivery and high-speed data transmission. The SNEAM design is based on the Quantum Confined Stark Effect (QCSE), offering high modulation depth, low power consumption, and a compact footprint. For remote powering, we explored two optical coupling methods, laser to laser edge coupling and second surface normal coupling to GaAs based PPC. We demonstrated laser to laser edge coupling using commercially available laser sources as efficient PV absorbers. By coupling a 1427 nm pump laser to a 1540 nmsingle-junction receiver laser, an efficiency of 33% was achieved with an open circuit voltage V_{oc} of 0.83 V. With an 850 nm pump laser coupled to a 905 nm triple junction receiver laser, we observed efficiency of 32.7% with V_{oc} of 3.5 V.

In the second method, the multi-segment GaAs based PPC was illuminated under surface normal incidence using Gaussian and annular beam profiles delivered through a double-clad fiber. A Gaussian illumination of 850 nm on 350 μm diameter with 4 junction PPC results in 50% efficiency and V_{oc} of 4.56 V at 10.7 W/cm^2 illumination. For higher illumination on 4 junctions PPC, the annular beam illumination holds a maximum efficiency of 47.3% and V_{oc} of 4.76 V at 52.5 W/cm^2 illumination. We present comparative studies on Gaussian and annular beam illumination for compact design strategies and future improvement scope.

The SNEAM device in the 1560 nm operation were designed and fabricated. The device was successfully transfer printed onto a targeted reflection surface to enable reflection of modulated data using the EAM device. The SNEAM device with 30 µm active diameter and overall dimensions of 80 µm × 87 µm was tested for DC and AC characterization. The DC testing shows an extinction ratio of 6 dB between bias voltages of -2 V to -7 V. The data modulation over a single mode fiber were demonstrated at 1 Gbps with a driving voltage of 6 V. The device exhibits a 3 dB electro-optic bandwidth of 9 GHz at a bias voltage of -5 V.

Future work will focus on the hybrid integration of PPCs and the SNEAM device onto a single chip, packaged with multi-core fiber that supports both channels for power and data transmission. The design will target a compact 1 mm footprint optimized for distal-end imaging surgical tools, thereby advancing the development of miniaturized, high-performance diagnostic systems.

Acknowledgements

I am deeply grateful for my PhD journey, which shaped me both academically and personally, fostering resilience and leaving me with enriching and lasting memories at Tyndall National Institute that I will cherish throughout my life.

I would like to begin by expressing my sincere gratitude to my supervisor, Brian Corbett, for accepting me as his PhD student and for being consistently available for discussions despite his busy schedule. His guidance, patience, and constructive insights helped shape my research direction and strengthened my research skills and decision-making. His unwavering support throughout my thesis, particularly during critical and demanding decisions, played a vital role in the successful completion of this work. I would also like to express my sincere gratitude to my co-supervisor, Brendan Roycroft, for his valuable discussions on experimental design and associated challenges, which helped me overcome key technical difficulties. His insights encouraged me to explore new techniques in the lab and to approach experimental and simulation work with greater confidence and critical thinking.

I would like to sincerely thank James O'Callaghan for completing the device fabrication within a limited timeframe, enabling timely testing and analysis. I also acknowledge the support of the fabrication facility at the Tyndall National Institute, especially Dan and Colin, for their invaluable assistance in realizing the modulator devices. I extend my special thanks to John Justice for his continued support from the beginning of my PhD, particularly with lab equipment, process discussions, and mask design.

I also thank my collaborators at the Tyndall National Institute in the biomedical, systems design, MCCI, and packaging teams for their insightful discussions and collaborative approach, which strongly motivated this work.

I thank the III–V Materials and Devices Group—especially Fatih, Zhi, Samir, Owen, Abi, Ali, Yeasir and Hema—for their support in the cleanroom, assistance with equipment, and for addressing my questions throughout my research, as well as Valentina and Risov for their kind arrangements on my final day.

I sincerely thank my friends Hema, Madhu, and Nidhya, and my hosts in Ireland, Ellenar and the late Christy, for their kindness and support during my stay.

Finally, I express my deepest gratitude to my mother, Kumuda, and my husband, Deviprasath, for their unwavering love and support throughout my journey.

To
my Families and Friends

Chapter 1

Introduction

1.1 Motivation

In the past, advances in photonics have consistently translated into impactful medical applications, with successive technological milestones finding rapid adoption in clinical practice. The introduction of low-loss optical fibers marked a pivotal development, enabling the emergence of fiber-optic endoscopes and minimally invasive imaging systems that fundamentally changed how clinicians access and visualize internal anatomy. Subsequent progress in light-source technology—particularly the development of high-brightness light-emitting diodes (LEDs) and tunable laser sources—has further expanded the capabilities of biomedical imaging. These sources provide wavelength-selectable illumination that enhances image contrast and supports advanced techniques such as multispectral imaging for improved tissue characterization. Depending on the clinical application, illumination wavelengths spanning the ultraviolet to near-infrared regimes are employed, including 460–490 nm blue light for phototherapy, 470 nm for optogenetic activation, and red to near-infrared wavelengths (600–1350 nm) for deep-tissue cardiovascular monitoring and imaging [1].

In parallel with developments in photonic components, complementary metal–oxide–semiconductor (CMOS) image sensor technology has undergone rapid evolution. Driven largely by the smartphone industry's demand for extreme miniaturization, low power consumption, high pixel density, and cost-effective mass production, micro-scale CMOS image sensors have become increasingly capable and accessible. These attributes have been successfully translated into

biomedical imaging, where compact sensors such as the AMS NanEYE2D RGB [2] have enabled high-resolution imaging in highly constrained form factors. As a result, camera-on-tip endoscopes have emerged as a practical solution for delivering real-time visual information in minimally invasive procedures, combining small device footprints with clinically relevant image quality [3, 4]. This convergence of photonics and microelectronics has supported the development of surgical tools aimed at earlier disease detection and improved diagnostic accuracy, thereby facilitating intervention at earlier and potentially more treatable stages.

Conventional surgical endoscopes typically integrate multiple subsystems, including imaging and illumination modules, transmission pathways for data and electrical power, working channels for surgical tools or fluid management, and a flexible or rigid housing with a control interface. As endoscopic systems continue to miniaturize for catheter-based and minimally invasive applications, progress is driven not only by reductions in device size but also by increasing demands on real-time imaging quality at the distal end of the device, where the imaging sensor is positioned at the anatomical target site. In many diagnostic and interventional procedures, relative motion between the imaging tip and the target tissue arises from normal physiological processes, such as cardiac contraction or blood flow, as well as from device advancement during navigation. As imaging is performed closer to these target sites within confined anatomical pathways, such motion can degrade image quality and introduce motion-related blurring. Maintaining clinically useful visualization under these conditions increasingly relies on higher frame-rate imaging to preserve image clarity. Supporting this level of real-time imaging performance requires continuous transmission of image data from the distal imaging electronics to proximal control and processing units located outside the patient, with signals conveyed along the full length of the device.

In long, slender catheter-scale instruments, the electrical connections used for power delivery and data transmission extend along the full length of the device. When such systems are operated in radio-frequency (RF) –active settings, including magnetic resonance imaging (MRI), these continuous conductive paths can interact with MRI RF fields. Experimental studies on intravascular guidewires (thin conductive navigation wires) used in interventional MRI have demonstrated that such interactions can lead to induced currents and localized heating along the device between the patient interface and proximal external equipment [5].

Cardiac MRI studies employing catheter-based imaging (long flexible access tubes) further illustrate both the clinical value of combining local intravascular or intracardiac views with MRI's

ability to reveal tissue structure beneath and surrounding the visible surface—such as vessel wall thickness, plaque burden, or myocardial abnormalities—and the associated susceptibility of long electrical interconnects to RF-induced effects [6, 7].

To mitigate these interactions, conventional electrical interconnect approaches employ galvanic isolation, controlled current return paths, and RF suppression techniques. While effective, these measures typically increase device diameter and stiffness, limiting mechanical flexibility and complicating the integration of advanced distal imaging capabilities. Collectively, these constraints motivate the exploration of alternative interconnect and power delivery strategies, including optical fiber–based solutions, for next-generation chip-on-tip endoscopic systems [8].

Accordingly, the limitations of conventional electrical interconnects in highly miniaturized, RF-sensitive endoscopic systems motivate the exploration of optical fiber–based approaches as an alternative. In addition to providing intrinsic immunity to RF interference, optical fibers offer high data-carrying capacity that is well suited to supporting the increased bandwidth demands associated with real-time, high-frame-rate imaging at the distal tip optical fibers offer a lightweight, flexible, and electromagnetically immune medium capable of transmitting high-bandwidth data and, potentially, optical power. When combined with photonic integration, such approaches open a pathway toward simplifying system architecture while reducing susceptibility to electromagnetic interference and improving compatibility with sensitive clinical environments. Power-over-fiber concepts, in particular, offer the potential to decouple distal devices from conventional electrical wiring, enabling compact and robust systems capable of operating deep within the body. Collectively, these developments point toward a transformative shift in the design of next-generation minimally invasive surgical systems, where photonics plays a central role not only in sensing and imaging, but also in system-level functionality.

1.2 Power over fiber technology

Power-by-light technology, also known as power-over-fiber (POF), offers a remote powering through optical fiber by transferring optical power and converting to electrical power using photovoltaic (PV) cell or photovoltaic power converter at the remote location. Compared to conventional powering methods, the inherent nature of optical fiber leads to galvanic isolation and resistance to electromagnetic interference noise. By combining optical powering with well-established fiber communication systems, such links supports the demands of smart internet of

things [9]. A typical POF system comprises three main components, a high-power laser source, an optical fiber link, and a photovoltaic power converter.

1.2.1 High power laser source

Laser diodes (LDs) are the dominant choice due to their high optical output, commercial availability, compact form factor, and direct compatibility with fiber coupling. The selection of the laser wavelength is guided by the fiber's three main transmission windows and the spectral response of the PV converter [10]. For short-reach links < 1.3 km, GaAs/AlGaAs LD operating near 808 nm are widely used, offering high electrical-to-optical efficiency and excellent spectral matching to GaAs PV cells, although with higher fiber attenuation. Medium-distance transmission benefits from InGaAsP/InP LD at 1310 nm, which combine low attenuation with minimal chromatic dispersion, achieving a favorable balance between transmission performance and PV conversion efficiency. For long-haul links, 1480 nm LD and InAlGaAs/InP LD at 1550 nm are employed, taking advantage of low fiber attenuation and improved eye safety, despite reduced PV conversion efficiency. Higher delivered power in SMF can be achieved through multi-emitter LD arrays, improved coupling optics, and advanced fiber designs such as double-clad or multi-core configurations, which allow high-power transmission in the cladding while maintaining low-loss, high-bandwidth data transmission in the core. Fiber lasers have also been demonstrated to deliver higher continuous optical power in POF applications [11]. For the short-distance transmission of optical power and data considered in this work, with the optical source located at the proximal end of the endoscopic system, attention is restricted to laser diode–based sources.

1.2.2 Optical fiber

The choice of optical fiber strongly influences both power delivery and data transmission performance. Recent reviews have analyzed the various fiber types employed in modern POF applications [11] [12]. Figure 1.1 illustrates the cross-sections of various fibers demonstrating POF operation along with data transmission capability. Conventional single-mode fiber (SMF), with core diameters of approximately 9–10 µm, enable long-distance, low-loss transmission but exhibit limited power tolerance due to their small core size, which can lead to high optical power densities, nonlinear effects, and fiber fuse damage at elevated feed-light levels [13]. Multimode

fibers (MMF), with larger cores diameter of 50–62.5 µm, can support higher power transfer but suffer from modal dispersion, making them more suitable for short-reach applications. Multi-core fibers (MCFs) allow parallel transmission of power and data in separate cores, though each core's small diameter restricts individual power capacity. Double-clad fibers (DCFs) combine a small single-mode core 9 µm for broadband data with a large inner cladding of 105 µm for high-power delivery, enabling simultaneous power transmission and communication in a single fiber link [14]. Step-index plastic optical fibers provide milliwatt-level power delivery alongside multi-gigabit data rates over short ranges, making them attractive for in-home networks [15]. At high optical powers, connector design becomes a critical factor; expanded beam connectors with graded-index terminations and fusion splicing are employed to reduce insertion losses and improve damage thresholds. Fiber selection depends on the required transmission distance, bandwidth, and power capacity, with SMFs favored for long-reach links and DCFs for high-power applications. Notably, SMF based POF links have been demonstrated over 14.43 km with an optical loss of 3.89 dB [16], and later extended to an investigated link length of 25.2 km with remote power delivery of 26.2 dBm [17].

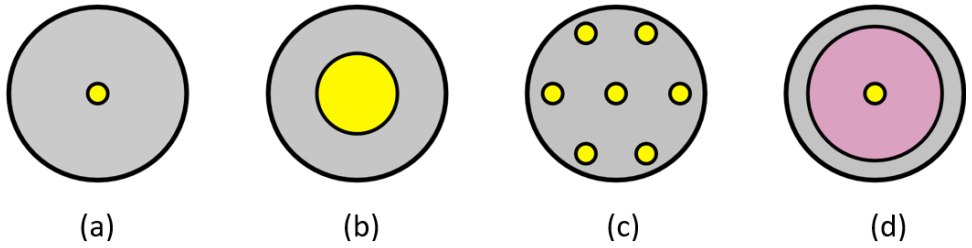


FIGURE 1.1: Schematic illustration of cross-section of optical fibers used in POF application. (a) SMF, (b) MMF, (c) MCF and (d) DCF.

1.2.3 Photovoltaic power converter (PPC)

Efficient PPC are a key requirement for the practical implementation of POF technology. The most widely used semiconductor materials for PPC design include gallium arsenide (GaAs), indium gallium arsenide (InGaAs), gallium antimonide (GaSb), and silicon (Si) [18] [19] [12]. In point-to-point energy transfer systems, the PPC is designed to convert monochromatic light into the required electrical power. Incident photons with energies equal to or greater than the semiconductor bandgap are absorbed, generating electron–hole pairs that contribute to the external circuit current when separated before recombination.

1.2.3.1 Material characteristics and reported efficiencies

GaAs-based PPCs are widely used due to their large direct bandgap of approximately 1.42 eV, enabling high optical absorption and open-circuit voltages approaching 1 V, with a corresponding spectral cutoff wavelength near 0.87 µm. Silicon, with an indirect bandgap of 1.12 eV, exhibits a cutoff wavelength of approximately 1.1 µm but typically delivers lower open-circuit voltages of around 0.7 V. Lattice-matched $In_{0.53}Ga_{0.47}As$, with a bandgap of approximately 0.74 eV and a cutoff wavelength near 1.68 µm, and GaSb, with a bandgap of approximately 0.72 eV and a cutoff wavelength of about 1.72 µm, extend the PV response toward longer wavelengths.

Recent work [20] reports that, in 2021, a GaAs-based single-junction PPC achieved an efficiency exceeding 68.9% at 858 nm by employing a backside reflection technique to maximize photon recycling. A single-junction InGaAs PPC grown on an InP substrate demonstrated 34% efficiency [21] at 1550 nm and 47.5% efficiency at 3.2 W/cm^2 under eye-safe operation [22]. In addition to InGaAs, GaSb has also been explored as a PV material for infrared laser illumination, and related studies have reported performance under monochromatic excitation near the material absorption edge. GaSb-based PV cells optimized for 1550–1700 nm operation achieved up to 49% efficiency at 1680 nm, corresponding to near-band-edge operation, decreasing to 45% at 1550 nm and 39% at 1315 nm due to reduced photoresponse [23]. Diffused GaSb cells with a 2 mm^2 photosensitive area optimized for 1550 nm have reached 28.4% measured efficiency, with potential efficiencies of 40% estimated for output powers of 20 W/cm^2, after reducing front metal shadowing [24, 25]. Silicon PPC have been experimentally demonstrated to achieve efficiencies approaching and exceeding 40% under near-infrared monochromatic illumination (λ= 0.9–1.0 µm) [26]. Given their low cost and mature manufacturing infrastructure, silicon cells are highly attractive for POF system; however, their indirect bandgap and lower output voltage compared to I–V semiconductors limit their suitability for designs requiring high voltage density.

1.2.3.2 Series-Connection Strategies for High-Voltage Output

At a remote sensor node the common supply voltage for integrated electronics is the delivery of 3.3 V or 5 V [27, 28]. In order to provide increased voltage output over the 1 V of a single-segment GaAs based PPC [28, 29], series-connected PPC subcell are required. Such

configurations can be implemented using either laterally series-connected multi-segment designs or vertically stacked multijunction architectures.

- **Lateral series-connected multi-segment converters:** Multiple segments are fabricated side-by-side on a semi-insulating substrate and connected in series by metal interconnects. The laser beam from an optical fiber is spread over the entire segmented active area, with each segment generating equal current and adding its voltage to the total. This reduces operating current and increases voltage output; however, insulation trenches between segments cause optical losses and make the device sensitive to misalignment and non-uniform illumination [30].

- **Vertically stacked multijunction converters:** Multiple subcells are grown in a vertical stack within the same semiconductor wafer and connected in series by transparent tunnel junctions. Monochromatic light passes through the stack, with each subcell thickness optimized for equal photocurrent generation. This design eliminates trench losses and provides high tolerance to beam misalignment, while achieving higher voltages in a compact footprint [31, 32]. The practical viability of this approach has been demonstrated through its commercialization by Azastra Opto was acquired by Broadcom Ltd., building on the vertically integrated GaAs PPC concept reported in [29]. However, this design demands precise current matching, making it more sensitive to laser wavelength drift, temperature variation, and fabrication tolerances [33].

1.2.3.3 Recent performance of series connected PPC

For remote powering, both designs present trade-offs, lateral designs are more robust to wavelength drift but suffer from trench losses and alignment sensitivity, while vertical designs achieve higher voltages in smaller areas but require stricter operating control. Ongoing experimentation and demonstration of PPC-based systems are expected to drive further design improvements and enhance conversion efficiency. Vertically stacked multijunction PPC technology has been successfully commercialized, with Broadcom being a leading supplier.

In [28], a monolithic laterally series-connected four-segment GaAs PPC with chip dimensions of 1.6×1.6 mm^2 has been demonstrated, delivering a voltage of 4.14 V and achieving an efficiency of 50.1% and at an incident power density of 51.6 W/cm^2. The same study reported a six-segment device with active diameter of 2 mm, which achieved a voltage of 6 V and an efficiency

of 42.7% at 22 W/cm^2. An application-specific laterally segmented GaAs PPC was designed for implantable neural stimulation, employing four series-connected segments for stimulation and two additional segments for active charge recovery, thereby enabling direct optical powering without electrical leads or external voltage conversion [34].

Using a vertical epitaxial heterostructure design [35], a record conversion efficiency of 74.7% has been demonstrated at a cryogenic temperature of 150 K for a five-junction GaAs-based PPC device with a chip area of 3 mm^2, illuminated at 808 nm. A recent study on 1520 nm illumination of an eight-junction vertically stacked $In_{0.53}Ga_{0.47}As$ cell achieved 36.96% efficiency at 53.9 W/cm^2, demonstrating strong potential for free-space and fiber-based long-distance laser power transmission [36]. InP based PPC operation at 1480 nm has also been demonstrated for POF transmission over SMF, with 870 mW of optical power delivered after a 10 km link, corresponding to 226.2 mW of electrical output based on a reported PPC conversion efficiency of 26% [37]. At the closely related wavelength of 1470 nm, a vertical multijunction PPC was demonstrated using ten thin InGaAs subcells interconnected by transparent tunnel junctions was demonstrated under cryogenic operation at 77 K, achieving a maximum conversion efficiency of 67.5% and delivering 1.35 W of electrical output at an average optical input intensity of approximately 62 W/cm^2 [38].

Building on these device-level results, a 1470 nm POF demonstration reported in 2024 [39], using standard 50 µm step-index and OM2 MMF, achieving delivered electrical powers of up to 179 mW over 300 m and 44.4 mW over 5.855 km with a 2 W input, with scalability projected to over 9 km for 150 mW delivery using higher-power lasers. This study also showed that Broadcom's multijunction PPC outperforms a commercial Kyosemi device, achieving 47.5% efficiency and handling up to 2 W of optical input.

1.3 Power and data over fiber technology

The use of optical fiber in place of electrical cabling enables power delivery that is immune to electromagnetic interference, eliminates the risk of electrical sparking, reduces system weight, and supports long-distance transmission due to the low attenuation of SMF (∼0.2 dB/km). By combining optical power and data transmission through fiber finds interest in diverse applications. The concept is explained in schematic diagram in Figure 1.2, where high-power laser and

a data transmitter send optical power and downstream communication signals. The two different wavelengths are combined through wavelength-division multiplexing and transmitted over a single optical fiber. At the remote end, a PPC performs optical-to-electrical power conversion, while an optical receiver recovers the transmitted data signal. For upstream communication, a separate data laser at the remote end transmits information back through the same fiber to a photodetector at the source side, enabling simultaneous bidirectional data transfer and remote power delivery through one optical link.

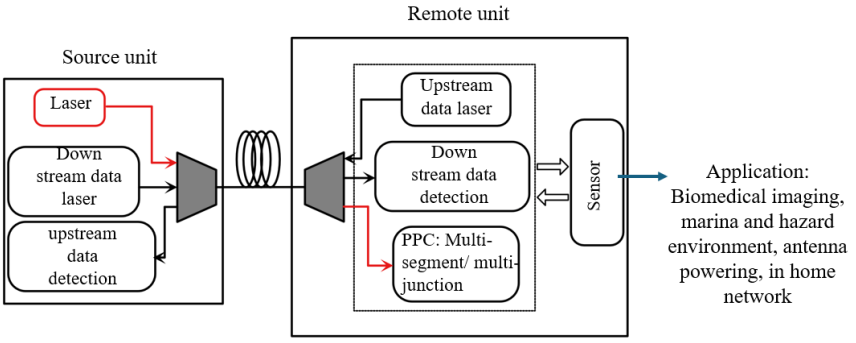


FIGURE 1.2: Schematic illustration of the POF system.

Here, we highlight the application demonstrated the remote sensor functioning using POF technology. The first reported demonstration dates back to 1978, when DeLoach et al. [40] built an optically powered sound alerter driven by a GaAlAs laser through a fiber to a PV detector, achieving 33%–36% optical-to-acoustic efficiency at 2 mW output power provide the feasibility of powering telephone ringers over fiber. From there, POF evolved across multiple applications, an early demonstration showed an optically powered video camera link over 100 m of multimode fiber using a GaAs PPC and DC–DC converter to provide 100 mW to a remote circuit [41]. POF has since been applied to challenging environments, such as an integrated system for seafloor observation from shore that used SMF to transmit high-power light at 1480 nm together with bidirectional data over an 8 km link, delivering 190 mW electrical power from a 31 W input while maintaining a 3.6 Mb/s data rate to operate acoustic and turbidity sensors [42]. Subsequent work demonstrated that the available delivered power and data robustness could be further improved by introducing optical isolation at the high-power laser output, enabling increased pump power while suppressing backscattering-induced spectral distortion and preserving bidirectional data transmission [43].

High-power implementations using MMF and DCF have achieved electrical outputs in the multiwatt range while maintaining communication integrity. A system transmitting 14 W of laser power over MMF to multiple PPCs produced 6 W electrical output with simultaneous

downlink data transmission [44], while another MMF based POF demonstration using 100 m of 200 µm core MMF delivered 1.7 W to the load from 5.4 W of launched optical power [45]. DCF-based single-fiber architectures have combined data transfer with delivery of up to 10 W electrical power over 300 m and 1 km to remote antenna units using multiple PPCs [46, 47]. Advances in MCF have enabled POF links to simultaneously transport analog radio frequency signals and deliver optical power. A 10 km, 7-core MCF link has been demonstrated to supply 133 mW optical power to a sensor node while maintaining coexistent analog RF transmission [48]. In another MCF based demonstration, a 1480 nm optical feed was transmitted through a 200 m, 4-core MCF with 300 mW of optical power launched per core and approximately 100 mW delivered at the remote node. The same study showed that a 2.6 Gbps data signal could be transmitted either through a separate core or multiplexed with the optical feed in the same core without measurable signal degradation [49].

Recent work has demonstrated the feasibility of simultaneously delivering optical power and data using wavelength-division multiplexing over standard SMF. Using this approach, it was shown that up to approximately 870 mW of optical power can be delivered to a remote site after 10 km, while increasing launched power degrades data transmission due to nonlinear effects, most notably stimulated Raman scattering [37]. Experimental investigations of wavelength-division-multiplexed transmission in single-core fibers further demonstrated that, even with spectral separation between power and data channels, intensity noise from the high-power feed light can be transferred to the data signal and lead to measurable performance degradation, as shown using MMF links [50]. Comparative studies across different fiber platforms reported that this power-induced noise transfer is intrinsic to single-core silica fibers, whereas MCF mitigate such effects through spatial separation of power and data channels and hollow-core fibers suppress nonlinear interactions altogether, with achievable power delivery in both cases primarily limited by fiber attenuation rather than data-quality constraints [51].

In the biomedical domain, POF has been employed to power miniaturized, conductor-free implants using 850 nm lasers, including retinal prostheses for vision restoration [52], nerve stimulators for epilepsy treatment [34], and intravascular minimally invasive surgical instruments such as catheters [53], where the elimination of conductive leads enhances patient safety and enables full MRI compatibility. More recently, catheter-based systems have incorporated a compact ASIC at the distal catheter tip that optically harvests power delivered from a proximal light source and employs an on-chip LED at the distal end for upstream optical data transmission, thereby realizing a fully optical, MRI-compatible intravascular interface [54]. Advancements in

POF device efficiency, system integration, and application-specific engineering are accelerating the transition of this technology toward broader deployment, supporting its adoption in an expanding range of remote, safety-critical, and electromagnetically sensitive applications.

1.4 Thesis Objective

The overall goal of this research is to enable optical power delivery and high-speed data transmission over a single optical fiber for minimally invasive endoscopic imaging systems operating under stringent constraints on device size, available electrical power, and in-body reliability.

The objective of this thesis is to develop and experimentally evaluate the key components required to support this goal. Specifically, the work focuses on PPC and optical modulators, assessing their electrical, optical, and dimensional performance. Rather than demonstrating full system-level integration, the scope of the thesis is limited to establishing the technical feasibility and performance limits of these individual components, with the aim of enabling future integration within catheter-scale endoscopic imaging systems targeting an overall footprint on the order of 1 mm $\times$ 1 mm.

Conventional endoscopic systems typically rely on two separate long copper wires for powering and real-time imaging, which can limit navigation flexibility, particularly when accessing millimeter-scale arteries and veins and micrometer-scale microvasculature within the cardiovascular system, and can also restrict their use in other anatomical regions. Recent demonstrations of optically powered microcameras integrated at the distal end of endoscopes with diameters as small as 2 mm have shown successful imaging of tissue mimicking phantoms (representative of biological tissue), establishing the feasibility of fiber-based power delivery for chip-on-tip endoscopic imaging as shown in Figure 1.3. In these demonstrations, a tissue-like phantom was imaged using the optically powered endoscope, with Fig. 1.3 (b) and (c) showing a feature measuring $\sim$1 mm. These results validate the use of lateral series-connected PV architectures to support miniature CMOS cameras, such as the 1 mm $\times$ 1 mm ams NanEye2D, which operates from 1.6 V to 2.4 V, requires 3 mW to 11 mW of electrical power, and supports data rates up to 100 Mbps. The PPC provides an output voltage of approximately 4 V, which is conditioned by on-camera electronics to meet the camera's operating voltage range, while the delivered current is adjusted through optical illumination power to satisfy the required power consumption.

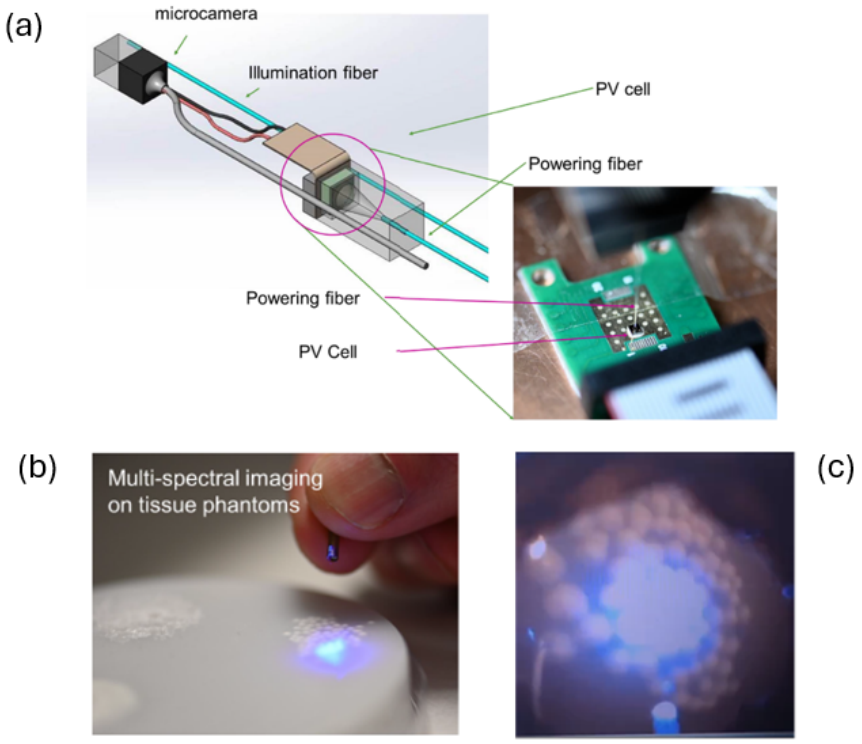


FIGURE 1.3: (a) Schematic of an optically powered microcamera system in which a surface-normal illuminated MMF delivers optical power to four laterally series-connected PV cell that electrically supply the microcamera. The PPC chip has a 250 µm active diameter within a 1 mm × 1 mm chip; the inset shows the illumination fiber attached to the PPC device. (b) Picture of a 2 mm outer-diameter optically powered chip-on-tip positioned over a tissue phantom.(c) Microcamera image showing a 1 mm-scale feature in the tissue phantom [55].

While fiber-based optical power delivery has been successfully demonstrated for chip-on-tip endoscopic imaging systems, extending this approach to support simultaneous data and power transmission under the same stringent power, voltage, and size constraints remains an active area of investigation. Conventional laser-based transmitters, including vertical-cavity surface-emitting laser (VCSEL), Fabry–Pérot (FP) lasers, and distributed feedback lasers, are widely employed in short-reach optical links and are typically operated using direct current modulation. Such devices require continuous electrical bias above the lasing threshold, resulting in non-negligible static power consumption [56, 57]. In addition, current-driven modulation necessitates dedicated biasing networks and high-speed driver circuitry, along with careful electrical and thermal design, which increases system complexity and footprint [58]. These requirements pose significant challenges for optically powered, catheter-scale endoscopic systems, where the available electrical power and voltage at the distal end are severely limited, motivating the exploration of alternative optical modulation approaches compatible with low-voltage and low-power operation.

In this context, surface-normal electroabsorption modulators (SNEAM) operate without stimulated emission or a lasing threshold and can be driven using low-voltage electrical signals [59]. This enables significantly reduced electrical power consumption compared to laser-based transmitters, making SNEAMs well suited for optically powered endoscopic systems in which the optical carrier is delivered remotely and only minimal local electrical power is available. SNEAMs also provide a compact device footprint and polarization-insensitive operation under surface-normal incidence, supporting compact distal-end integration for highly miniaturized, fiber-powered endoscopic imaging probes.

Building on this foundation, this thesis focuses on the systematic development, experimental characterization, and integration of PPC and a SNEAM for fiber-based powering and data transmission in minimally invasive endoscopic applications. The work targets microcamera systems operating under stringent electrical, optical, and physical constraints imposed by catheter-scale geometries. Achieving efficient remote powering and high-speed data transmission within these dimensional limits requires careful consideration of optical wavelength selection, achievable PV output voltage, illumination configuration, fiber architecture, and distal-end integration.

In this work, PPC device are implemented and experimentally assessed under two optical coupling configurations—edge-coupled and surface-normal illumination to determine their ability to deliver sufficient voltage and power while remaining compatible with compact distal-end implementation. The performance of each configuration is characterized in terms of optical coupling efficiency, illumination uniformity, and electrical output characteristics relevant to microcamera operation. Guided by the electrical requirements identified from the PV studies and the spatial and packaging constraints imposed by the ams NanEye2D microcamera and catheter-scale instrumentation, including the need for electrical and physical integration with the PPC, a reflective SNEAM is designed, fabricated, and experimentally characterized to enable high-speed optical data transmission under low-voltage and low-power operating conditions. The SNEAM architecture is selected to ensure compatibility with PV-powered CMOS imaging systems and surface-normal optical interfaces.

The results from the individual device studies are combined to identify an integrated distal-end configuration that enables efficient power delivery and high-speed data transmission over a single optical fiber. This configuration supports compact packaging of the PV converter, modulator, and optical fiber, providing a practical solution for next-generation optically powered

chip-on-tip endoscopic imaging systems.

1.5 Thesis Outline

The thesis includes five chapters. Following the introduction, Chapter 2 introduces and experimentally investigates PPC using an edge-coupled waveguide geometry, beginning with telecom-wavelength 1550 nm infrared experiments using commercially packaged fiber-coupled lasers to demonstrate remote power delivery and upstream data transmission. The study is then extended to shorter near-infrared pumping configurations using unpackaged receiver devices, including single-junction and triple-junction receivers, to investigate high-voltage operation under compact optical coupling arrangements.

Chapter 3 explores remote powering using surface-normal illumination from a DCF onto a multi-segment GaAs-based PPC. The study compares the performance of a laterally interconnected four-segment PPC under quasi-Gaussian illumination and annular beam shaping, the latter achieved by angularly tilting the DCF to concentrate light on the edges of the active area rather than the center, thereby reducing losses in trenches and metal lines. Current–voltage characteristics are measured at various fiber-to-device spacings to evaluate their impact on cell parameters. At the nominal optimum spacing, Gaussian illumination achieves peak performance at an irradiance of 20.8 W/cm^2 but degrades with increasing power, whereas annular illumination maintains performance and demonstrates superior voltage and fill factor, with current output improved through enhanced beam confinement.

Chapter 4 presents the design and transfer printing of a reflective SNEAM operating in the C-band. The device is characterized through photoresponse measurements, reflection spectrum analysis, capacitance–voltage analysis. High-speed performance testing, including bandwidth evaluation (S_{21} parameter) and eye diagram analysis. The chapter also addresses the design challenges of realizing a compact SNEAM with an air–semiconductor interface as the top reflector, without a protective front layer.

Chapter 5 summarizes the key results of the thesis and outlines future work on the hybrid integration of PPC and the SNEAM device onto a single chip, targeting a compact 1 mm footprint optimized for distal-end imaging surgical tools.

Note: The laterally interconnected four-segment GaAs PPC was originally designed and fabricated as part of a separate research project and was used by the author for experimental

characterization in this thesis. Fabrication of the SNEAM devices was performed by James O'Callaghan at Tyndall National Institute, based on device designs and process flow developed by the author. High-frequency characterization of the SNEAM devices was performed by Asif Khan at Tyndall National Institute. Further details of this work will be reported in his PhD thesis.

AI-based language tools were used for grammar refinement and coding assistance during manuscript preparation; all scientific content, analysis, interpretation, and conclusions are solely the author's own.

Chapter 2

Experimental study on photovoltaic power converter in edge coupled configuration

2.1 Introduction

The conversion efficiency of incident photons to electrical power in a PPC device is determined not only by the material properties and bandgap alignment with the illumination wavelength, but also by how the device design facilitates efficient carrier transport and minimizes recombination losses. In conventional surface-normal photovoltaic configurations, front-side metallization is required for current collection. Front-side metal fingers are employed to facilitate carrier extraction, with total metal coverage scaling with the number of fingers. Increased metallization improves lateral carrier collection and reduces series resistance, but also introduces optical shadowing that limits photon absorption and carrier generation in the active region, leading to a fundamental trade-off between optical and electrical performance.

To overcome these limitations, and as considered in this work, a lateral or edge-coupled geometry can be employed, where light is guided parallel to the active region, often realized as a multiple quantum well (MQW) waveguide, allowing photon absorption along the propagation path. In this design, light travels laterally through the active region while the electrical contacts are positioned on the top and bottom surfaces for current collection. This short spatial separation between the optical absorption region and the electrical contacts can potentially

enhance carrier transport efficiency and reduce resistive losses. In addition, the edge-coupled geometry enables optical coupling using a SMF, supporting efficient power delivery in compact device structures. An understanding and careful selection of PPC coupling geometries, whether edge-coupled or surface-normal, are essential for POF systems. In endoscopic tools, the remote optical link depends on the chosen PPC geometry, which defines the design constraints, as the limited tool diameter restricts the available space and determines whether single or multiple fibers can be employed for simultaneous power delivery and data transmission. Therefore, system integration and overall performance are strongly influenced by the selected device geometry and packaging configuration.

This chapter presents an experimental study of an edge-coupled PPC realized using commercially available waveguide laser sources. The work demonstrates optical to electrical power conversion achieved by optically pumping a receiver laser that acts as an absorber in the edge-coupled configuration. The experiments were designed to evaluate PPC performance through current–voltage (I–V) characterization at both telecom and near-infrared wavelengths. At the telecom wavelength, a pump laser operating at 1427 nm and a receiver laser at 1540 nm were used to achieve a conversion efficiency of 33%, delivering a maximum voltage of 0.6 V and an open-circuit voltage V_{oc} of 0.83 V. The same configuration also enabled upstream data transmission up to 500 Mbps, demonstrating the feasibility of simultaneous optical power and data transfer over fiber.

To extend this demonstration into the near-infrared regime, two additional pump–receiver laser pairs were studied. In the first case, a 980 nm pump laser was coupled to a 1064 nm single-junction receiver laser, achieving a conversion efficiency of 23.8% with a V_{oc} of 1 V. In the final case, an 850 nm pump laser was coupled to a 905 nm triple-junction receiver laser, achieving a higher conversion efficiency of 32.7% and a V_{oc} of 3.5 V. The I–V characterization performed in these experiments is used to extract key PPC parameters, including open-circuit voltage, short-circuit current, fill factor, maximum power point, and overall power conversion efficiency, which are discussed in the following sections.

2.2 Edge coupling configuration

The approach of employing a waveguide laser as a PPC follows from the principle of thermodynamic reciprocity, originally derived from Kirchhoff's law of thermal radiation, which states that an efficient emitter is also an efficient absorber. Consequently, a PPC optimized

for maximum radiative efficiency would, in principle, also be capable of lasing under population inversion, reflecting the intrinsic symmetry between light emission and absorption in such structures. This work utilizes a waveguided MQW laser structure as both the absorber and converter in an edge-coupled configuration as illustrated in Figure 2.1. The incident illumination P_{illum} is laterally coupled into the active region, where photon absorption generates electron–hole pairs. Under illumination, electrons drift and diffuse from the p-type toward the n-type region, while holes move in the opposite direction. These photo-generated carriers are separated by the built-in electric field and collected at the contacts, giving rise to the photo-generated current I_{ph}. The absorption behavior of a semiconductor material is fundamentally

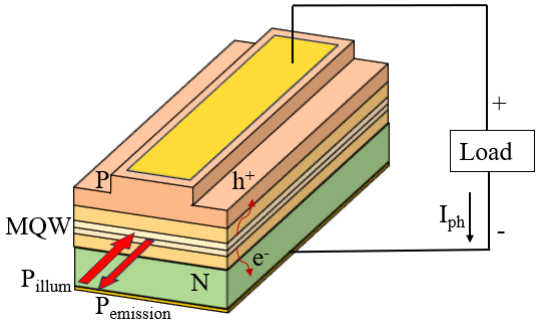


FIGURE 2.1: Schematic of the waveguide receiver laser operating as a photovoltaic (PV) converter, where incident optical power P_{illum} is absorbed in the MQW region generates carriers that produce a photocurrent I_{ph} driving an external load.

governed by its bandgap energy E_g, which defines the minimum photon energy required to generate electron–hole pairs. Photons with energies below E_g pass through the material without contributing to carrier generation, while those with energies significantly above E_g lose their excess energy through carrier thermalization. Thus, the optimum conversion efficiency is achieved when the incident photon energy closely matches the bandgap of the absorber. Furthermore, the absorption coefficient α, which quantifies the ability of a material to absorb light per unit length, determines how efficiently photons of a given wavelength are absorbed within the active region. Materials with higher absorption coefficients enable thinner devices to achieve strong absorption, whereas materials with lower absorption coefficients require longer effective optical paths or enhanced confinement to ensure sufficient photon absorption and carrier generation. Hence, the choice of absorber material and its corresponding absorption strength is critical to achieving effective light–matter interaction within the active region, thereby enhancing the overall efficiency and performance of the PPC.

In waveguide-based PPC structures, the effective absorption of the guided optical mode depends on both the intrinsic material absorption coefficient and the fraction of the optical field

confined within the absorbing MQW. In the absence of detailed device design parameters of commercially available waveguide lasers, these quantities can be approximated using representative material data and typical confinement factors reported in the literature. The effective absorption coefficient and the corresponding absorption length can be expressed as

$$\alpha_{\text{eff}} = \Gamma\, \alpha_{\text{mat}}, \qquad L_{\text{abs}} = \frac{1}{\alpha_{\text{eff}}} \tag{2.1}$$

where α_{mat} is the intrinsic material absorption coefficient and Γ is the optical mode-overlap factor representing the fraction of the optical field confined within the MQW region. Both α_{mat} and Γ are functions of the optical wavelength and polarization, and consequently the effective absorption coefficient depends on the wavelength and polarization of the guided mode.

The transmitted optical power along the propagation path, x, follows Beer–Lambert's law,

$$P_{trans}(x) = P_{illum} e^{-\alpha_{\text{eff}} x} \tag{2.2}$$

where P_{illum} is the optical power coupled into the waveguide at $x = 0$. The absorption length L_{abs} corresponds to the propagation distance at which P_{trans} decreases to $1/e$ (approximately 37%) of its initial value. This relation describes the decay of optical power along the propagation direction and provides an estimate of the absorption and carrier generation profiles would be used in design optimization across different device configurations.

2.2.1 PPC parameter

The performance of an illuminated PV device is commonly evaluated through I–V characterization, as illustrated in Figure 2.2. Key parameters extracted from the I–V curve such as the **short-circuit current (I_{sc})**, **open-circuit voltage (V_{oc})**, **fill factor (FF)**, and **conversion efficiency (η)** are used to describe and compare the electrical performance of PV devices.

These parameters are derived from the illuminated diode equation, which expresses the net current under illumination as

$$I = I_0 \left[\exp\left(\frac{qV}{nkT} \right) - 1 \right] - I_{ph} \tag{2.3}$$

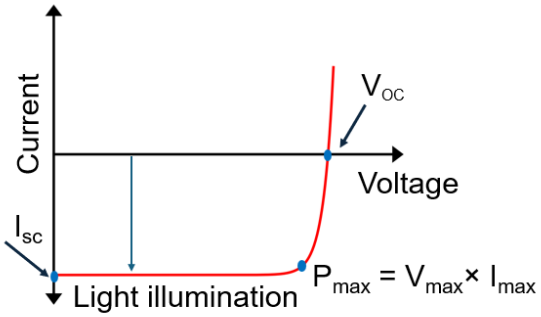


FIGURE 2.2: Schematic I–V characteristic of a PV device under illumination, shown by the red curve. The maximum power point, indicated by P_{max}, is used to calculate η and FF.

where I_{ph} is the photogenerated current, I_0 is the diode dark saturation current, q is the elementary charge of an electron, n is the ideality factor, k is the Boltzmann constant, and T is the absolute temperature in Kelvin.

Short-Circuit Current I_{sc}: Under short-circuit conditions ($V = 0$), the collected photocurrent is measured as the short-circuit current. For the ideal illuminated diode described by Equation 2.3, the short-circuit current corresponds to the magnitude of the photogenerated current ($I_{sc} = I_{ph}$) and represents the maximum current generated by the PV device under illumination. In this condition, the entire photogenerated current flows through the external circuit since there is no voltage to drive a significant dark current in the opposite direction. The short-circuit current is governed by the rate of carrier generation due to incident photons and the efficiency of carrier collection at the junction before recombination occurs. Consequently, I_{sc} depends on the incident light intensity, the spectral response of the semiconductor material, and carrier transport properties such as carrier lifetime and diffusion length. It is also directly proportional to the illuminated active area of the device, as a larger area allows absorption of more photons and generation of more carriers. Therefore, I_{sc} is a fundamental parameter for assessing the photocurrent generation capability of a PV cell.

Open-Circuit Voltage V_{oc}: The open-circuit voltage represents the voltage at which no current flows through the external circuit, corresponding to the maximum potential that a PPC can deliver under illumination. Physically, V_{oc} corresponds to the forward-bias condition where the diode (dark) current exactly compensates the photogenerated current, resulting in zero net current. Under this condition, it can be expressed from the illuminated diode equation as

$$V_{oc} = \frac{nkT}{q} \ln\left(\frac{I_{ph}}{I_0} + 1\right) \tag{2.4}$$

According to this relation, V_{oc} increases logarithmically with the photogenerated current and decreases with increasing saturation current. The magnitude of I_0 is determined by carrier recombination processes within the device and is influenced by factors such as defect density, carrier lifetime, and temperature. Thus, V_{oc} reflects the recombination behavior of the PV device and indicates how efficiently photogenerated carriers are separated and collected within the absorber and junction regions.

Fill Factor FF: When the PPC operates under either short-circuit ($V = 0$) or open-circuit ($I = 0$) conditions, no electrical power is delivered to the external circuit. Therefore, the operating point must be chosen such that the output power ($P = IV$) is maximized. The point on the I–V characteristic where this condition occurs is known as the maximum power point (MPP), defined by $\frac{dP}{dV} = 0$, as shown in the I–V curve. The fill factor is a dimensionless parameter that describes the squareness of the I–V curve, indicating how closely the characteristic approaches the ideal rectangular shape of an ideal diode. It is defined as

$$\mathrm{FF} = \frac{I_{\mathrm{max}} V_{\mathrm{max}}}{I_{\mathrm{sc}} V_{\mathrm{oc}}} \tag{2.5}$$

where the subscript "max" denotes the values of current and voltage at the maximum power point. The fill factor is strongly influenced by resistive losses within the device. The series resistance and shunt resistance are the two main parasitic resistances that affect the curvature of the I–V characteristic. A high series resistance causes voltage drops at higher current levels, reducing the slope of the I–V curve near the open-circuit region. In contrast, a low shunt resistance introduces leakage paths that reduce the current under short-circuit conditions ($V \approx 0$), decreasing the slope of the I–V curve around I_{sc}. Both effects reduce the sharpness of the I–V knee, lower the fill factor, and decrease the maximum power output of the device. In practical PV systems, operation near the MPP is maintained using maximum power point tracking algorithms, which adjust the operating voltage and current dynamically under varying illumination and temperature conditions.

Conversion Efficiency η: The conversion efficiency is a key parameter that quantifies how effectively a photovoltaic device converts incident optical power into electrical power. It is defined as the ratio between the maximum electrical power output P_{max} and the total incident

optical power P_{illum} received by the active area of the device,

$$\eta = \frac{P_{\text{max}}}{P_{\text{illum}}} \tag{2.6}$$

The efficiency provides a direct measure of device performance, enabling comparison of photovoltaic materials, device architectures, and fabrication processes.

2.3 Single junction edge coupled PPC

Following the discussion of photovoltaic parameters, this section presents the experimental realization of a single-junction edge-coupled PPC operating at telecom wavelengths and near infrared wavelength. The study is based on an edge-coupled laser-to-laser power conversion configuration, where one laser functions as the optical transmitter and the second as the optically pumped receiver. This arrangement enables compact optical power delivery while simultaneously allowing remote optical data transmission, thereby demonstrating the dual functionality of power conversion and communication within a single photonic device.

2.3.1 Edge coupling between 1480 nm to 1540 nm receiver laser

The laser-to-laser power conversion experiment was carried out using two commercially available QW waveguide lasers coupled through single-mode optical fibers, as illustrated in Figure 2.3 (a). The transmitting laser operated at a wavelength of 1427 nm and served as the optical pump, while the receiving laser, emitting at 1540 nm, functioned as the PPC. The pump wavelength was chosen so that the photon energy exceeds the bandgap of the receiving photovoltaic converter by a slight offset, limiting thermalisation losses and improving conversion efficiency. Both devices were butterfly-packaged and directly connected without an optical isolator, forming a compact edge-coupled configuration. The optical coupling efficiency between the transmitter and receiver waveguides was measured to be $65 \pm 1\%$, determined by operating the receiver laser as a photodetector. The loss is due to the fiber connection, the lens coupling within the package, and the coating on the front facet of the receiving laser. The PPC measurement on the receiver laser was performed using mini hook test leads with BNC cable connected to anode and cathode pins on the receiver laser as shown in Figure 2.3 (b). All measurements were performed with the receiver laser temperature stabilized at 20 °C.

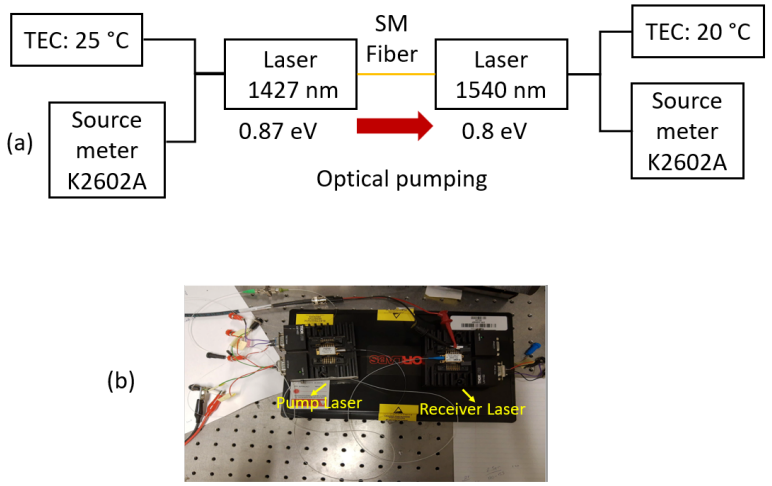


FIGURE 2.3: (a) Schematic of laser-to-laser power conversion through edge coupling using a SMF. (b) Experimental setup showing both lasers in packaged form, where the pump laser optically pumps the receiver laser and the resulting electrical current is measured using mini hook test leads connected to the receiver laser anode and cathode.

2.3.2 Results and discussion

2.3.2.1 PV characteristics

The I–V characteristics shown in Fig. 2.4 (a) were measured for the receiver laser operating as a photovoltaic converter under various absorbed optical powers. The incident optical power launched from the pump laser was varied from 10 mW to 110 mW in steps of 10 mW. The optical coupling efficiency from the transmitting laser into the receiver waveguide was calibrated to be 64% by operating the receiver laser as a photodetector. This coupling efficiency accounts for losses due to the fiber connection, lens coupling, and the front-facet coating of the receiver laser. Accordingly, the absorbed optical power within the MQW waveguide ranged from approximately 6.4 mW to 70 mW. The effect of optical illumination on the PPC is evident in the I–V curve, where a photocurrent is generated in the reverse direction relative to the diode dark response (black line) recorded with under no light condition. The voltage across the diode was swept using a source meter (Keithley 2602A), while the corresponding current was measured over a bias range from –0.5 V to 1 V to capture the complete photovoltaic response.

The key PPC parameters were extracted from the measured current–voltage characteristics. Figure 2.4 (b) shows a linear increase in I_{sc} and a logarithmic increase in V_{oc} with absorbed optical power. In this waveguide based PPC, the I_{sc} reaches nearly 80 mA at an absorbed power of 70 mW, indicating efficient carrier generation and collection within the active region, where the photogenerated carrier density scales directly with the absorbed photon flux. This behavior

is achieved even though the effective absorption length in the MQW region is relatively short, approximately 25 µm for 63% absorption. The absorption length is estimated by assuming an optical mode overlap of about 5% with the MQW region for a waveguide geometry of approximately 1 µm × 3 µm and an absorption coefficient near wavelength of 1.5 µm of about 8000 cm^{-1}, which are typical parameters for commercially available MQW waveguide lasers. The limited absorption length does not restrict carrier collection in the edge-coupled geometry, as the generated carriers are redistributed along the device through the low-resistance metal contacts. This mechanism enables uniform carrier extraction across the entire active region, minimizing spatial non uniformities associated with localized absorption near the input facet.

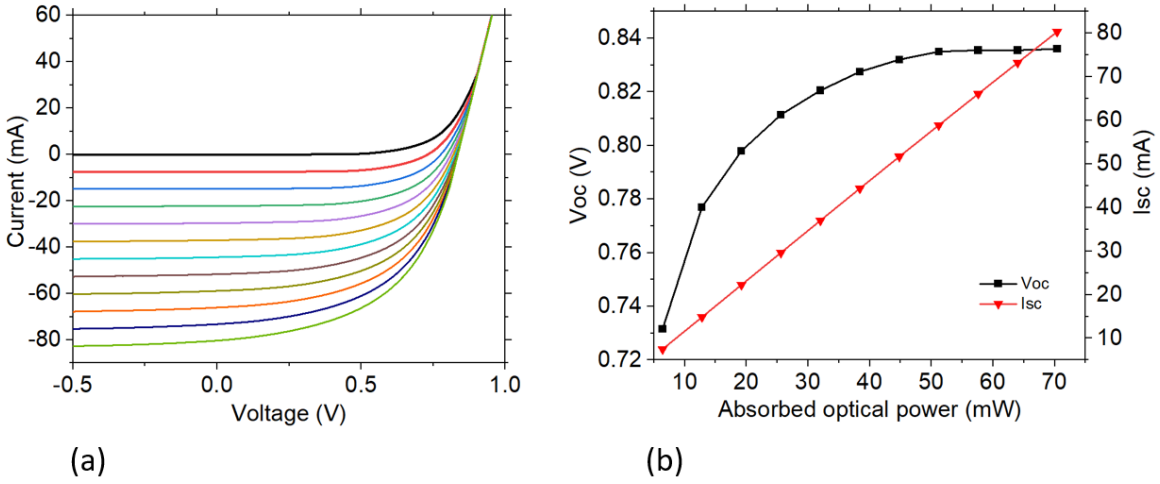


FIGURE 2.4: (a) I–V characterization of edge coupled waveguide PPC under no optical incident illumination (black curve-top) and with variation of absorbed optical power from 6.4 mW (red-top second curve) to 70 mW (bright-green-bottom). (b) Variation of V_{oc} and I_{sc} as a function of absorbed optical power, showing the logarithmic increase of V_{oc} and the linear dependence of I_{sc} with optical power.

The V_{oc} increases rapidly at low absorbed power due to the rise in carrier concentration and gradually saturates near 0.83 V for absorbed powers above 45 mW. This saturation occurs as carrier screening within the MQW limits further voltage buildup. This value significantly exceeds the open-circuit voltages typically reported for single-junction 1550 nm PPC (0.4–0.5 V) [60] [24]. The achieved voltage of 0.83 V exceeds the photon energy of the waveguide receiver laser emission (0.8 eV), which indicates that strong optical pumping generates carrier densities high enough to approach population inversion. Under these conditions, the separation between electron and hole populations corresponds to an electrical potential greater than the photon energy associated with the bandgap transition. As a result, the observed V_{oc} reflects a non-equilibrium carrier distribution established under intense optical injection rather than an equilibrium bandgap limited behavior. Beyond this point, additional optical power primarily

enhances the stimulated emission instead of further increasing V_{oc}, leading to the observed voltage clamping. The PPC is capable of delivering voltage at maximum power point was 0.6 V, representing the highest reported value for single-junction converters operating at 1540 nm.

Figure 2.5 (a) shows the electrical output power from the photovoltaic converter as a function of voltage for various absorbed optical powers. The electrical power increases with voltage up to a maximum point and then decreases toward the open-circuit condition, forming a distinct peak that defines the maximum power point for each illumination level from 6.4 mW to 70 mW. As the absorbed optical power increases, both the maximum electrical output and the corresponding operating voltage rise, indicating enhanced carrier generation and a higher V_{oc}. The curvature of the plot becomes steeper at higher power levels, reflecting stronger current generation, while increased carrier screening limits further increases in the operating voltage. A maximum electrical output of 35 mW is achieved at an absorbed optical power of 70 mW. These characteristics are used to extract the power conversion efficiency η and fill factor FF

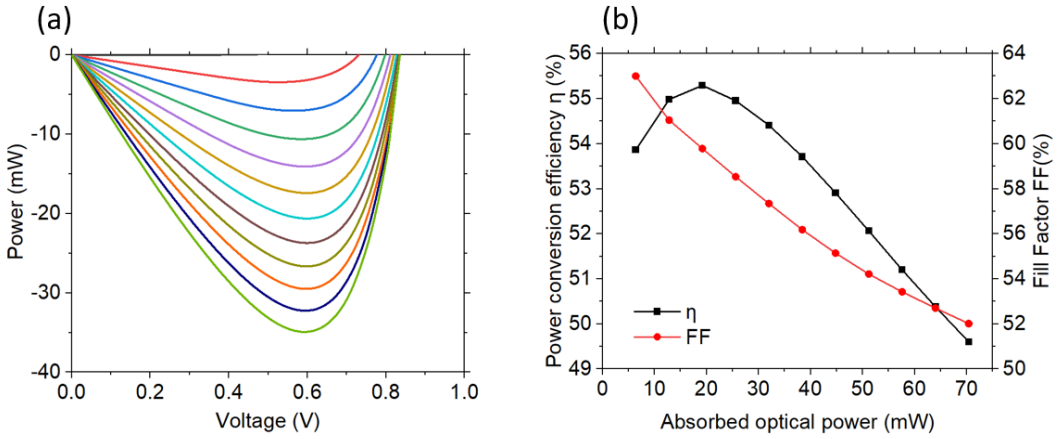


FIGURE 2.5: (a) Output P-V characteristics of the receiver laser PPC under different absorbed optical powers from 6.4 mW (red-top) to 70 mW (bright-green-bottom). (b) Variation of η and FF as a function of absorbed optical power, showing a gradual decrease at higher optical injection due to carrier density dependent effects.

presented in Figure 2.5 (b). The efficiency of the waveguide PPC, (η), calculated as the internal power transfer efficiency, is defined as the ratio of the measured electrical output power to the absorbed optical power in the waveguide. A maximum η of 55.3% is achieved at an absorbed power of 19 mW and decreases to 49.6% at 70 mW, primarily due to carrier screening at higher excitation levels. The overall fiber to device conversion efficiency is 35%, calculated as the ratio of the measured electrical power to the optical power delivered through the fiber before coupling into the receiver waveguide PPC.

FF decreased from 63% at 6.4 mW of absorbed optical power to 52% at 70 mW of absorbed optical power. At high optical injection from the pump laser, the waveguide PPC generates very high carrier densities in the MQW region, which strongly affect carrier transport and extraction. The accumulated charge partially screens the internal electric field, thereby reducing the efficiency of field-assisted carrier collection. As the carrier density increases further, non-radiative Auger recombination becomes the dominant loss mechanism due to its strong dependence on carrier concentration compared with radiative or defect-related processes. The combined effects of field screening and enhanced Auger recombination shorten the carrier lifetime and limit the extractable current near the maximum power point, resulting in a reduced squareness of the I–V curve and a corresponding decrease in FF with increasing absorbed optical power.

2.3.3 Receiver PPC lasing under optical pumping

The emission spectra of the receiver laser under reverse-bias conditions and optical pumping were characterized using the experimental setup illustrated in Figure 2.6. The pump and receiver lasers were interconnected via an optical circulator, and the emission from the receiver laser was routed to port 3 for spectral analysis using an optical spectrum analyzer (OSA).

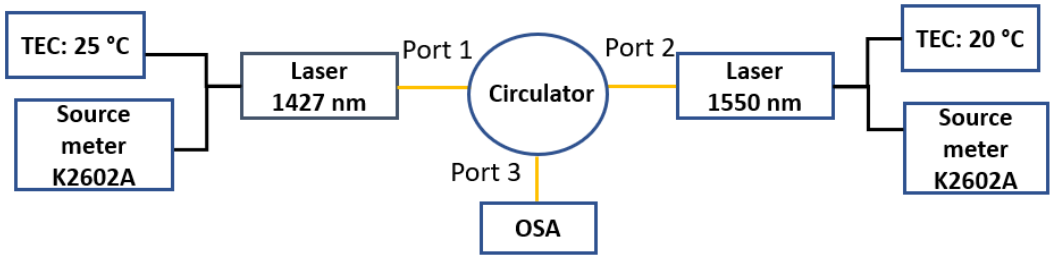


FIGURE 2.6: Schematic of the receiver laser PPC setup used to characterize lasing behavior under optical pumping through an optical circulator. Black lines indicate electrical connections, and yellow lines represent SM optical fibers.

Under open-circuit conditions, the receiver laser transitioned from the absorption regime to the emission regime when the absorbed optical power exceeded 45 mW, as indicated by the clamping of V_{oc} at 0.83 V. This voltage saturation reflects the onset of population inversion and the establishment of optical gain within the receiver cavity.

The emission spectra of the receiver laser were measured at a constant absorbed optical power of 70 mW under varying reverse-bias conditions, as shown in Figure 2.7. Under zero-bias conditions, optical pumping alone was sufficient to achieve lasing, confirming that the injected photon flux exceeded the threshold for stimulated emission shown in Figure 2.7 (a). A residual

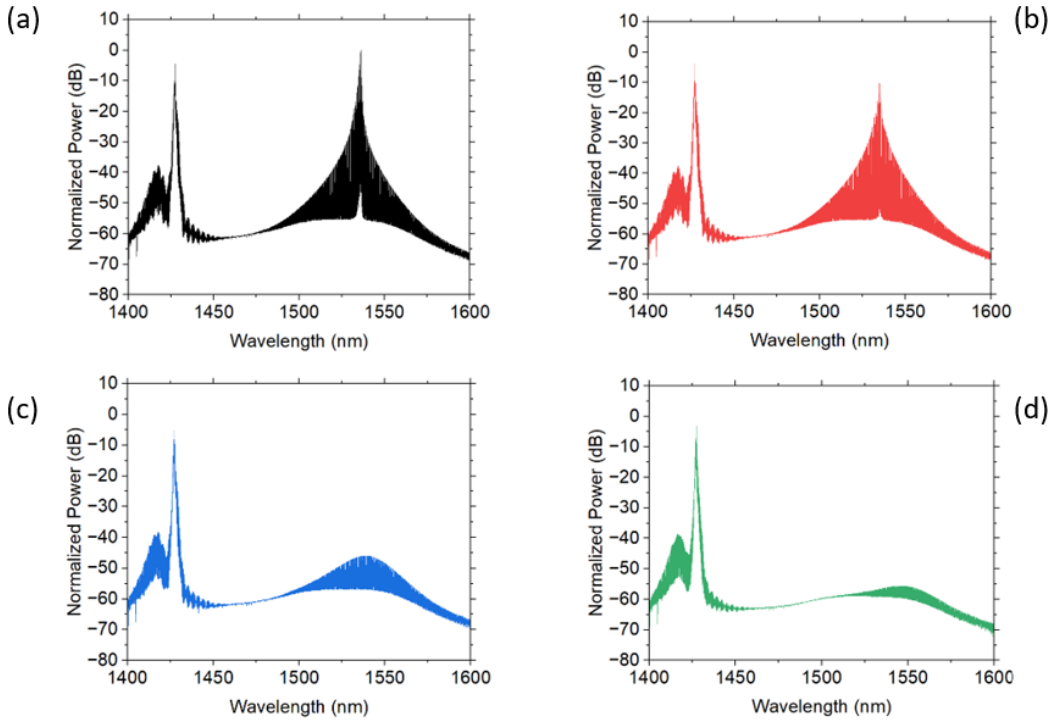


FIGURE 2.7: Emission spectrum of receiver laser near 1540 nm under zero bias and reverse bias condition with optically pumped by 1427 nm (a) 0 mA (b) -10 mA (c) -20 mA and (d) -30 mA.

peak corresponding to the 1427 nm pump laser was also detected at OSA through the circulator due to back reflection from the receiver facet. When a reverse bias of 10 mA was applied, the receiver continued to exhibit lasing along with photocurrent extraction, as shown in Figure 2.7 (b). This demonstrates that carrier extraction and photon generation coexist in the lasing regime of the optically pumped waveguide PPC. As the reverse bias increased further, carrier extraction began to dominate over radiative recombination, leading to a gradual suppression of the lasing peak in Figure 2.7 (c). At sufficiently high reverse bias, stimulated emission was fully quenched and only background noise remained near 1540 nm, indicating the complete depletion of the optical gain region as seen in Figure 2.7 (d).

The variation of the threshold current of the receiver laser with optical pumping was analyzed using the reciprocal differential current extracted from the measured I–V characteristics under different absorbed optical powers, as shown in Fig. 2.8 (a). Since the I–V data were acquired with a constant voltage step between successive bias points, the incremental current change, dI, was calculated as the difference in measured current between adjacent voltage points. The reciprocal, $(\frac{1}{dI})$, was then plotted as a function of the measured current. The resulting curve exhibits a distinct kink that marks the lasing threshold, corresponding to the transition from

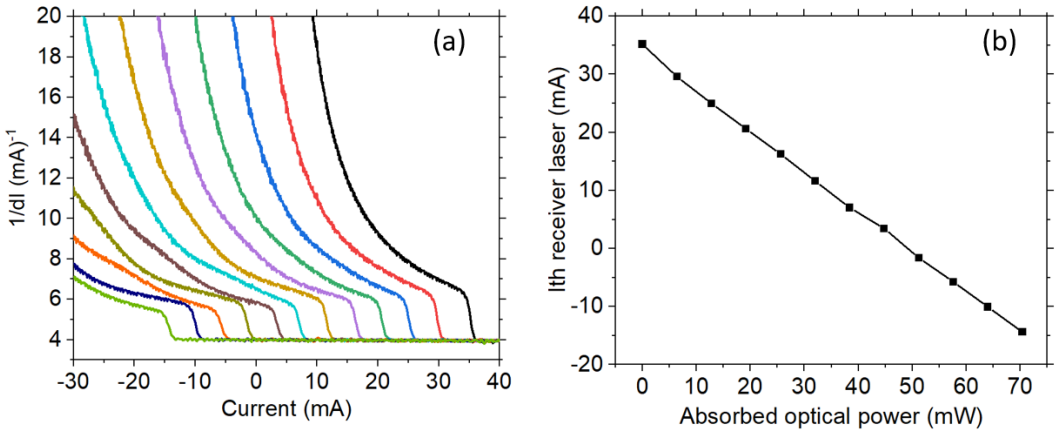


FIGURE 2.8: (a) Plot of the inverse differential current $\frac{1}{dI}$ versus current for absorbed optical powers ranging from 0 mW (no pumping) to 70 mW The curves are colour-coded from black (right) to light green (left), indicating increasing absorbed optical power. (b) Threshold current (I_{th}) as a function of absorbed optical power.

spontaneous to stimulated emission. As the absorbed optical power increases, this kink systematically shifts toward lower electrical current, indicating a reduction in the threshold current I_{th}. This shift occurs because optical pumping contributes to the carrier population in the active region, thereby reducing the electrical injection needed to reach the lasing condition. At higher pump levels, lasing is predominantly sustained by optically generated carriers, leading to a further decrease in I_{th}. The extracted variation of I_{th} with absorbed optical power is summarized in Figure 2.8 (b), where I_{th} becomes negative for absorbed powers exceeding 45 mW and decreases linearly with optical pump power at a rate of approximately 0.7 mA/mW, demonstrating efficient optical carrier injection and stimulated emission in the receiver laser.

2.3.3.1 Remote Data Transmission

To demonstrate the dual functionality of the receiver laser as both a PPC and a data transmitter, optical data transmission experiments were carried out using the same device under optical pumping. The experimental setup, illustrated in Figure 2.9, consists of a pump laser providing optical excitation to the receiver laser through an optical circulator. The receiver laser was connected to a pulse pattern generator (PPG) through a 10 dB electrical attenuator and a DC blocking capacitor to prevent DC shunting through the PPC caused by the 50 Ω output impedance of the PPG. A 2^9 -1 pseudo-random bit sequence (PRBS9) signal was applied from the PPG to the receiver laser, providing a small AC modulation (measured as 22 mV_{pp} delivered to the laser) at bit rates ranging from 100 Mbps to 500 Mbps. The modulated optical output from the receiver laser was routed back through the circulator (port 3) and detected

by a photoreceiver, while the waveform and corresponding eye diagrams were recorded using a 1 GHz and an 8 GHz bandwidth oscilloscope. During operation, the receiver laser was biased near the V_{oc} and modulated around zero net current, enabling efficient optical data transmission under optical pumping.

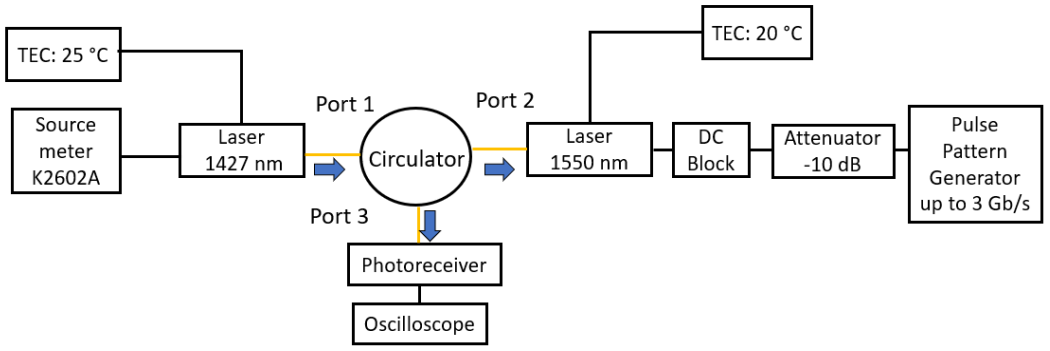


FIGURE 2.9: Schematic of the experimental setup for optical pumping and data modulation of the receiver laser using a pulse pattern generator through an optical circulator, demonstrating upstream data transmission operation. Black lines indicate electrical connections, and yellow lines represent SM optical fibers.

Figure 2.10 (a) shows the effect of absorbed optical pump power on the received data transmission signal recorded from the receiver laser. It is clearly observed that when the absorbed optical power exceeds 40 mW, a distinct modulated signal appears, confirming that under sufficient optical pumping, the receiver laser can operate as a self-powered optical modulator without any external electrical bias at the receiver end. The amplitude of the detected waveform increases with pump power, indicating enhanced optical injection and stronger modulation depth. To further assess the data transmission performance of the receiver laser, eye diagram measurements were performed for observing signal quality and modulation bandwidth of the receiver laser operating under optical pumping.

Eye diagrams were recorded between 100 Mbps and 500 Mbps for an absorbed optical power of 60 mW. A clear eye opening is well seen under 100 Mbps data transmission in Figure 2.10 (b) and under 500 Mbps data transmission the eye diagram exhibits a narrower and partially closed eye, with a visibly reduced vertical opening and increased noise in both logical levels as shown in Figure 2.10 (c). The bit error rate (BER) was estimated from the quality (Q) factor derived from the eye diagram, serving as a key indicator of data transmission performance. As shown in Figure 2.10 (d), stable data transmission was achieved at low bit rates (200–300 Mbps) with a BER of –14.3 on the logarithmic scale (5.4×10^{-15}), indicating error-free operation. With increasing data rate, the BER gradually increased and reached –4.3 on the logarithmic scale (4.79×10^{-5}) at 500 Mbps, which remains within the forward error correction limit for

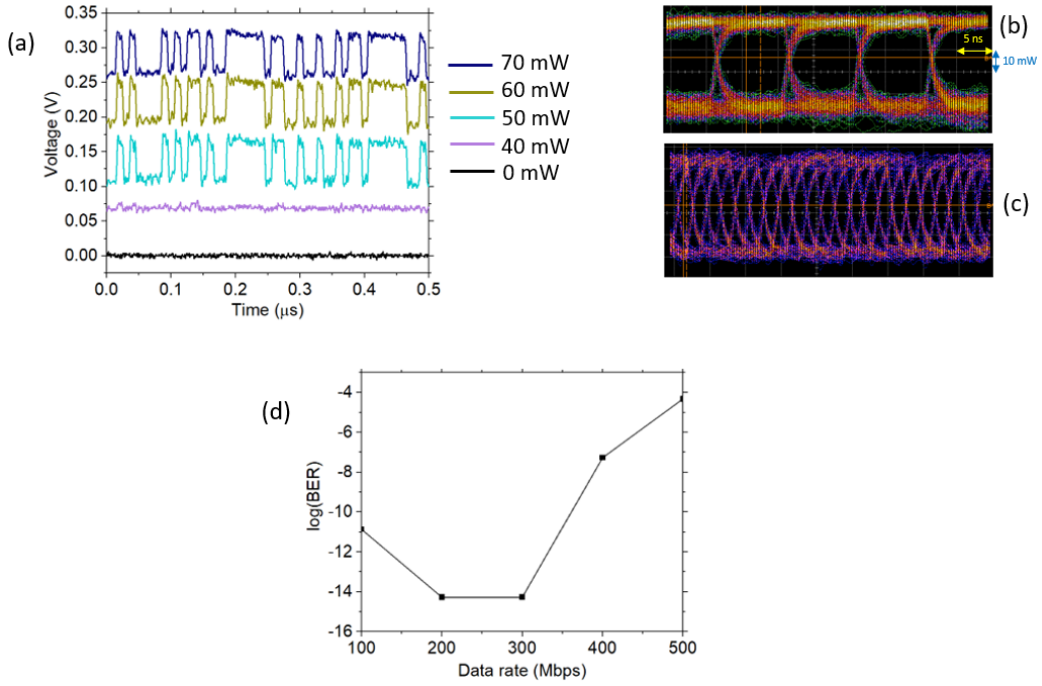


FIGURE 2.10: Data transmission from the receiver laser. (a) Detected 100 Mbps modulated signals from the receiver laser under varying absorbed optical powers, showing modulation onset above 40 mW. Eye diagrams of the received signal at varying data rates, illustrating the transition from a wide-open eye at lower bit rates (b) 100 Mbps and partially closed eye at higher bit rates (c) 500 Mbps. (d) Bit error rate (BER) plotted as a function of data rate, showing stable data transmission 200 Mbps to 300 Mbps.

reliable communication. Consistent with this trend, the BER was calculated to be 10^{-11} at 100 Mbps and 10^{-4} at 500 Mbps, confirming the receiver laser capability for upstream optical data transmission under optical pumping.

2.3.4 Edge coupling between 980 nm to 1064 nm device

Following the demonstration of the PV response of the edge-coupled receiver laser at 1550 nm under 1427 nm optical pumping, the further experiment was aimed to enhance the overall power conversion efficiency. The PPC at shorter wavelength offers stronger absorption compared to the 1427–1550 nm system, owing to the intrinsic material properties of the semiconductor structure. In the previous setup, both the pump and receiver lasers were butterfly-packaged devices, which limited optical coupling efficiency from the pump fiber to the receiver waveguide. To overcome this constraint, subsequent experiments were performed using an unpackaged bare chip receiver laser in an edge-coupled configuration. For this study, a single-junction laser operating at 1060 nm with a wide waveguide was employed as the receiver, and a 980 nm Fabry–Perot (FP) fiber-coupled laser was used as the optical pump.

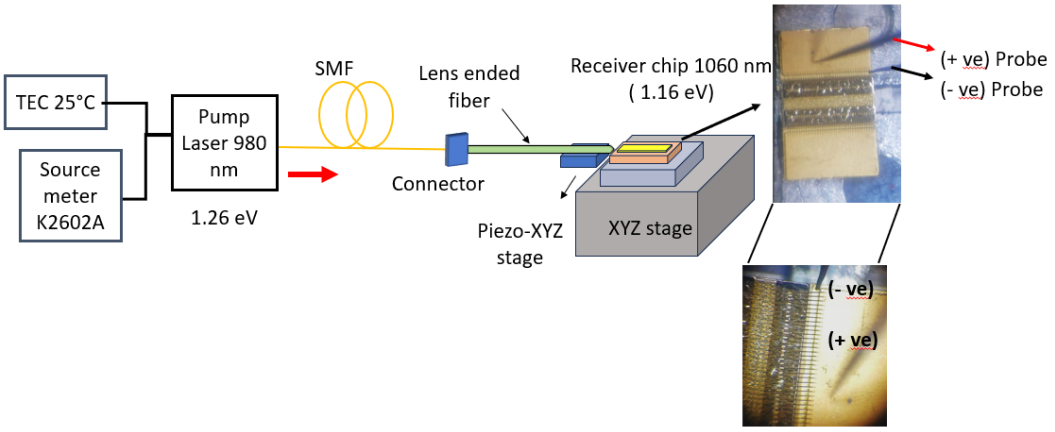


FIGURE 2.11: Experimental setup for optical power transfer using an edge-coupled waveguide laser receiver. A SMF–coupled pump laser is focused onto the receiver facet through a tapered lensed fiber mounted on an XYZ stage. The absorbed optical power generates photocurrent across the device terminals. Insets show the bare chip (top right) and needle probe placed on the chip indicating polarity (bottom right).

Figure 2.11 shows the schematic of the experimental setup used for optical power transfer measurement. A SM fiber (SMF-780 HP) fiber coupled 980 nm pump laser (1.26 eV) serves as the optical source, and its output is connected to a tapered lens end fiber through an optical connector. The tapered lens fiber has a standard spot size ranging from 2 µm to 6 µm. The lensed fiber is mounted on a piezoelectrically controlled stage, enabling fine adjustment and accurate focusing of the beam onto the facet of the 1060 nm (1.16 eV) receiver laser chip. The receiver device, provided by the Ferdinand-Braun-Institut (FBH), is a single quantum well (SQW) 1064 nm ridge waveguide laser featuring a 90 µm stripe width and a 4 mm resonator length, configured in a p-side-down mounting. The device exhibits a vertical far-field divergence of approximately 50° at 95% power content. The laser chip is mounted on an XYZ translation stage to enable precise fiber-to-waveguide alignment and maximize coupling efficiency. Electrical needle probes contacts the positive and negative terminals of the receiver, and I–V characterization performed.

2.3.5 Result and discussion

2.3.5.1 I–V characterization of on chip LPC

The incident optical power on the 1060 nm waveguide PPC is defined as the launched pump laser power. The optical pump power at 980 nm was varied from 0 to 80 mW in steps of 10 mW. Due to the photon energy difference between the pump wavelength (980 nm, 1.26 eV) and the

receiver wavelength (1060 nm, 1.16 eV), a down-conversion loss of 7.9% is introduced. This loss is incorporated through normalization of the incident optical power to the receiver wavelength, such that all reported incident optical powers correspond to corrected values ranging from 0 to 74 mW for the data presented.

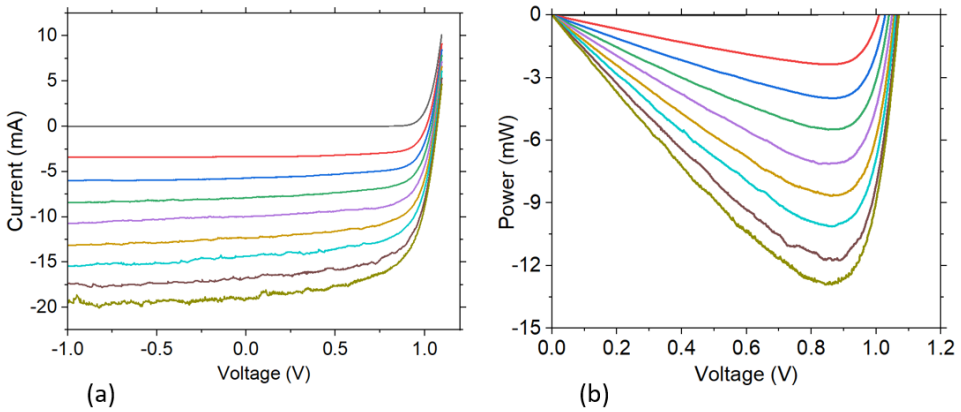


FIGURE 2.12: (a) I–V and (b) P-V characteristics of the 1060 nm waveguide laser operating as a PPC under different levels of incident optical power. The curves show the transition from dark to illuminated conditions, with photocurrent and output electrical power increasing proportionally with optical intensity. The curves are colour-coded from black (top) to olive-green (bottom), corresponding to incident optical powers ranging from 0 to 74 mW, obtained from pump power steps of 10 mW after normalization.

Figure 2.12 (a) shows the I–V characteristics of the 1060 nm waveguide laser operating as a PPC, illustrating the variation from the dark response to illuminated conditions with incident optical power ranging from 10 mW to 74 mW. The photocurrent increases with incident optical power, confirming carrier generation within the thin SQW active region. Beyond 40 mW of incident optical powers, the I–V curves exhibit slight fluctuations near the short-circuit region and clearly visible at 74 mW of incident optical power, which would be attributed from coupling instability and reflection-induced interference in the optical setup, as well as pump-laser power variations. The I–V curves exhibit a reduced incremental change in current near the open-circuit region at higher optical injection levels, suggesting high-injection effects that limit the voltage build-up. This behavior is consistent with carrier screening and increased recombination in the MQW region, which can modify the junction field and reduce the FF. The corresponding P–V characteristics in Fig. 2.12 (b) show that the maximum electrical output power increases with absorbed optical power. For an absorbed optical power of 74 mW, the device delivers 13 mW of electrical power to the external circuit.

Under open-circuit conditions for the single-junction PPC, as shown in Figure 2.13 (a), the V_{oc} shows a steady increase with incident optical power, consistent with the characteristic diode

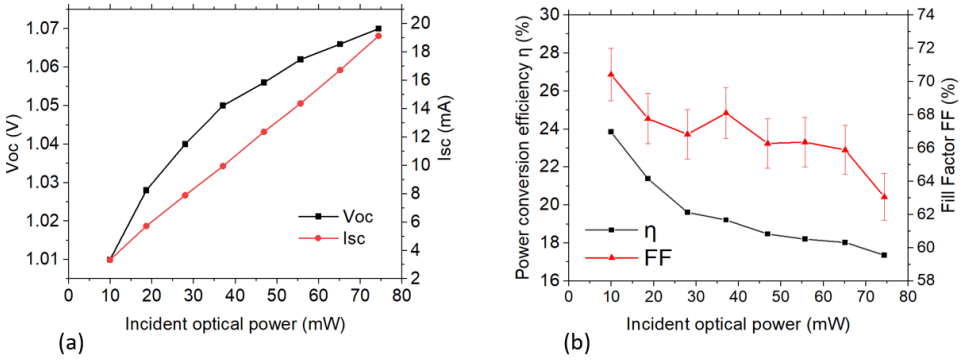


FIGURE 2.13: (a) Variation of of the 1060 nm single-junction PPC with incident optical power. (a) V_{oc} and I_{sc} showing a steady increase with illumination. (b) η and FF, with peak values of 23% and 70% at 10 mW, respectively. FF error bars denote the propagated I–V uncertainty used in the FF extraction, assuming 1.5% current and 0.5% voltage uncertainty, corresponding to a relative FF uncertainty of 2.24%. The slight FF increase near 40 mW lies within this uncertainty and is attributed to coupling fluctuations.

behavior of a photovoltaic device. A V_{oc} of 1.01 V is measured at 10 mW of incident optical power, which rises to 1.07 V at 74 mW. The I_{sc} increases from 3.3 mA at 10 mW to 19.1 mA at 74 mW, indicating carrier generation with increasing illumination. The maximum voltage at the operating point is observed to be 0.86 V at 18.6 mW of incident power. Figure 2.13 (b) shows that the maximum power conversion efficiency reaches 23% at 10 mW and decreases to 17.3% at 74 mW. The FF follows a similar trend, decreasing from 70% to 63% with increasing optical power. A slight increase in FF from 66.8% to 68.1% is observed near 40 mW. This local increase is not considered a systematic improvement in device performance, but is attributed to minor fluctuations in the measured photocurrent caused by variations in optical coupling as the incident optical power is increased. To indicate the significance of this variation, error bars were added to the FF values. The FF uncertainty was estimated from the measurement uncertainties in I_{max}, V_{max}, I_{sc}, V_{oc}, which are the parameters used to extract FF from the I–V curve. Voltage and current uncertainties of 0.5% and 1.5%, respectively, were used for this estimate, giving an overall propagated FF uncertainty of approximately 2.24%. The small FF rise near 40 mW lies within this uncertainty range, supporting the interpretation that it arises from measurement and coupling fluctuations rather than from a physical increase in FF. Overall, these results indicate that, while strong carrier accumulation supports high voltage generation, carrier extraction becomes increasingly limited at higher optical injection levels and is highly sensitive to the beam coupling geometry between the lensed fiber and the waveguide facet. Small variations in the optical injection profile or coupling efficiency can therefore significantly influence carrier generation and extraction across the device aperture

2.4 Edge coupling between 850 nm to 905 nm device triple junction PPC

In PPCs, the output voltage can be increased either by lateral series connection of multiple PV segments, as in surface-normal configurations, or by vertically stacking multiple p–n junctions within a single device structure. In the waveguide-based PPC, stacking p–n junctions in series provides an effective approach to boost the overall open-circuit voltage. To demonstrate this concept and achieve output voltages approaching 3 V typically required for low power electronic applications, a 905 nm Osram Nanostack laser diode with three epitaxially stacked p–n junctions, commonly used as a pulsed emitter in LiDAR (Light Detection and Ranging) systems, was employed in this experiment as the PPC. The device was optically pumped using an 850 nm fiber-coupled laser diode, as illustrated in Figure 2.15. The 852 nm pump laser

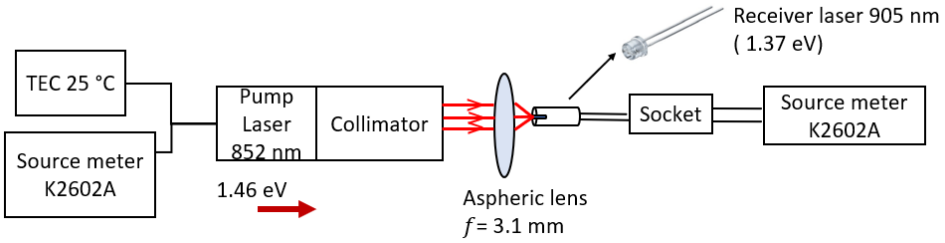


FIGURE 2.14: (a) Experimental setup for optical power transfer using an 850 nm pump laser and a 905 nm triple-junction waveguide receiver. The fiber-coupled pump laser is collimated (focal length f = 8.1 mm; spot size = 1.74 mm) and focused onto the receiver facet through a lens (f = 3.1 mm; spot size = 5 µm) in an edge-coupled configuration. The inset shows the packaged 905 nm triple-junction receiver diode.

output is coupled into the waveguide of the receiver laser, which consists of three epitaxially stacked p–n junctions designed for lasing at 905 nm. Since the pump laser is fiber-coupled while the receiver operates in free-space, a collimator and focusing lens was implemented to form an edge-coupling configuration between the two devices. The 4.4 µm spot size from the pump laser is expanded and collimated using a collimator and an aspheric lens, producing a focused beam with a 5 µm spot size. The beam is then coupled into the receiver laser waveguide with dimensions of 200 µm × 10 µm (W × H) housed inside plastic package. The optical path consists of a fiber collimator (850 nm, f = 8.1 mm) and an aspheric lens (Thorlabs C330TMD-B, f = 3.1 mm at 830 nm) to ensure efficient coupling into the receiver facet. The incident optical power from the pump laser was measured at the position of the aspheric lens using a photodetector prior to illuminating the receiver laser. The edge-coupling setup was placed inside a laser safety enclosure, as the operating wavelength is not eye-safe. The photon energy

mismatch between the 905 nm pump laser (1.37 eV) and the 850 nm receiver laser (1.46 eV) introduces a down-conversion loss of approximately 6%. The launched pump power was varied from 10 mW to 70 mW in steps of 10 mW, and the reported incident optical power corresponds to the effective power at the receiver facet after applying this down-conversion correction. As a result, the effective incident optical powers used in the characterization plots range from 9.4 mW to 65.8 mW.

2.4.1 Result and discussion

2.4.1.1 I–V characterization of the triple junction LPC

Optical coupling from the lens system to the receiver waveguide was optimized by setting the receiver under short-circuit conditions and adjusting the XYZ translation stage of the waveguide mount while monitoring the increase in short-circuit current I_{sc}. Once the maximum I_{sc} was obtained, the alignment was fixed, and the laser safety enclosure was closed.

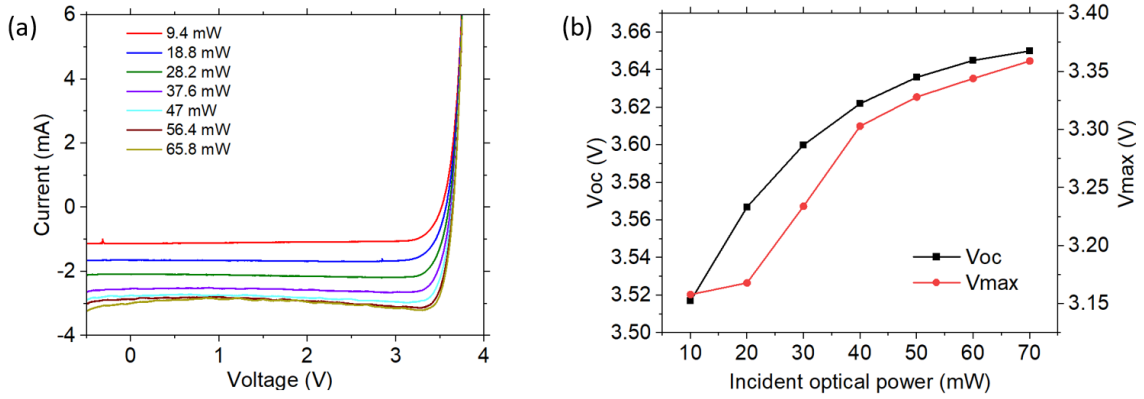


FIGURE 2.15: (a) I–V characteristics of the 905 nm triple-junction waveguide PPC under varying incident optical power from 9.4 mW (top curve) to 65.8 mW (bottom curve), showing increased photocurrent with illumination. Variations in the curves arise from optical coupling instability during measurement. (b) Variation of V_{oc} V_{mpp} with incident optical power, demonstrating voltage multiplication from the three series-connected p–n junctions and a maximum output of 3.1 V at 9.4 mW.

Figure 2.15 (a) shows the I–V characteristics of the 905 nm triple-junction waveguide PPC under different levels of incident optical power. The photocurrent increases with illumination, rising from 9.4 mW (red curve) to 28.2 mW (green curve) and higher power levels, indicating enhanced carrier generation across the stacked junctions. However, during the course of data acquisition, slight coupling instability to the receiver lasers was observed. The receiver

alignment gradually shifted over time, leading to major variations in the measured I–V characteristics between successive measurements from 9.4 mW to 65.8 mW of incident optical power. In a triple-junction configuration, equal optical illumination and current generation across all three p–n junctions are essential, as the total current is limited by the junction generating the lowest photocurrent. Any misalignment or nonuniform optical coupling therefore results in unequal excitation of the stacked junctions, reducing the measured photocurrent and overall device performance. The V_{oc} at 9.4 mW and 28.2 mW of incident optical power, observed to be 3.52 V and 3.6 V demonstrating the expected voltage multiplication from the three series connected p–n junctions. The variation of V_{mpp} with incident optical power, shown in Figure 2.15 (b), follows a near-logarithmic trend with increasing illumination V_{oc}. The receiver waveguide is capable of delivering 3.1 V at 9.4 mW of incident optical power.

The efficiency of the receiver waveguide was determined as the ratio of the electrical output power from the receiver laser to the incident optical power. Figure 2.16 shows that the triple-junction PV receiver exhibits a maximum efficiency of 35% at an incident optical power of 10 mW, which decreases to 24.6% at 28.2 mW. Under 9.4 mW illumination, the FF is observed to be 82%. As the illumination power increases, both the I_{sc} and the current at the maximum power point V_{mpp} and I_{mpp} are influenced by gradual misalignment of the optical coupling over time. Consequently, the FF calculation is also affected at higher incident optical powers due to coupling instability.

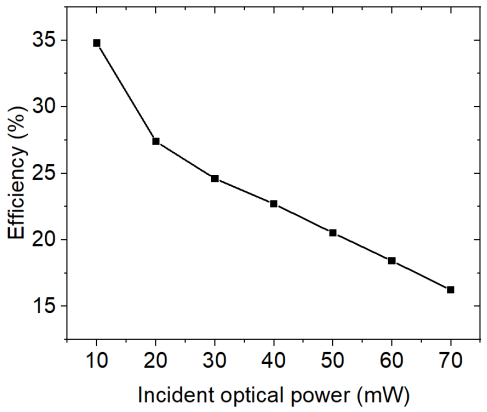


FIGURE 2.16: Efficiency of the triple-junction waveguide receiver plotted as a function of incident optical power.

The impact of non-uniform optical illumination on the performance of a triple p–n junction stack integrated within a 10 µm-high waveguide was analysed using a Python-based numerical model A.1, as shown in Fig. 2.17. The model evaluates the overlap between a Gaussian optical

field and the segmented waveguide aperture comprising the top cladding, active region, and bottom cladding. The active region contains three stacked p–n junctions, represented as Seg 1, Seg 2, and Seg 3. This analysis captures the trade-off between underfilling and overfilling of the active region. Figures 2.17 (a)–(d) show the calculated spatial intensity distributions at the receiver facet for increasing Gaussian beam waist values, together with the corresponding fraction of the total incident optical power distributed across the waveguide layers and the three p–n junction segments. For small beam waists, the optical field underfills the aperture, leading to a highly nonuniform power distribution in which the central junction receives a dominant fraction of the optical power, while the remaining junctions are weakly illuminated. As the beam waist increases, the optical power is redistributed more evenly across the three junctions, with each junction receiving a comparable fraction of the total incident power which is 25% in Figure 2.17 (b)). For larger beam waists, the optical field overfills the waveguide aperture, and an increasing fraction of the incident power is lost to the top and bottom cladding regions, reducing the power available to the active junctions.

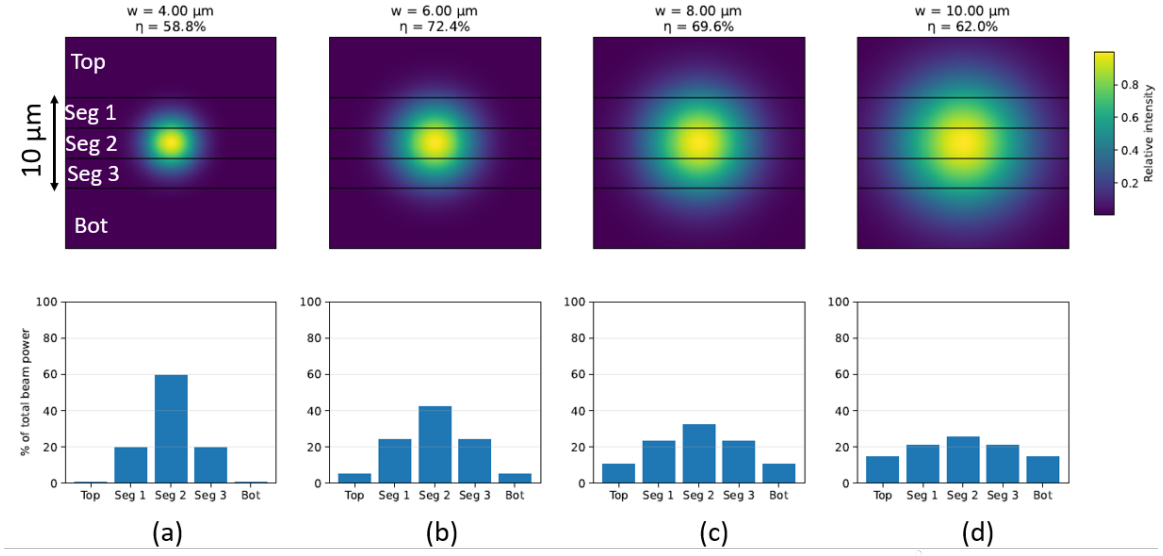


FIGURE 2.17: Numerical analysis of Gaussian beam coupling to a triple p–n junction waveguide receiver. (a–d) Simulated spatial intensity distributions at the receiver facet for increasing Gaussian beam waist values (w = 4, 6, 8, and 10 µm), together with the corresponding fraction of optical power incident on each segment of the p–n junction stack within the 10 µm-high waveguide.

In a series-connected junction stack, current continuity requires the same current magnitude to flow through all junctions, such that the extractable electrical current is limited by the junction generating the lowest photocurrent, while the output voltage scales with the number of junctions through voltage addition. Accordingly, the effective power transfer efficiency η is determined by the minimum optical power fraction delivered to any of the three junctions

multiplied by the number of stacked junctions. As the beam waist increases and the power distribution across Seg 1–Seg 3 becomes more uniform, the minimum power fraction rises, resulting in an increase in η. This response leads to a maximum efficiency of approximately 72% at a beam waist of about 6 µm, where the three junctions receive nearly equal optical power. For smaller beam waists, strong non uniformity limits the output to lower values, while for larger beam waists, optical spillover into the cladding regions reduces the power available to the junctions and causes η to decrease again to 69% and 62%. These results show that the efficiency trend is governed by the balance between junction current matching and optical spillover losses inherent to Gaussian beam coupling.

Figure 2.18 summarizes the dependence of the calculated η on the Gaussian beam waist incident on the receiver facet. The efficiency exhibits a clear maximum at a beam waist of 6 µm, where η reaches about 72%, corresponding to near equal power distribution across the three junction segments. For smaller beam waists, underfilling of the waveguide aperture leads to strong nonuniformity in the power distribution and a reduced efficiency, while for larger beam waists, overfilling of the aperture results in increasing optical spillover into the cladding regions and a corresponding decline in η. Validating SPICE-based circuit analysis, presented in

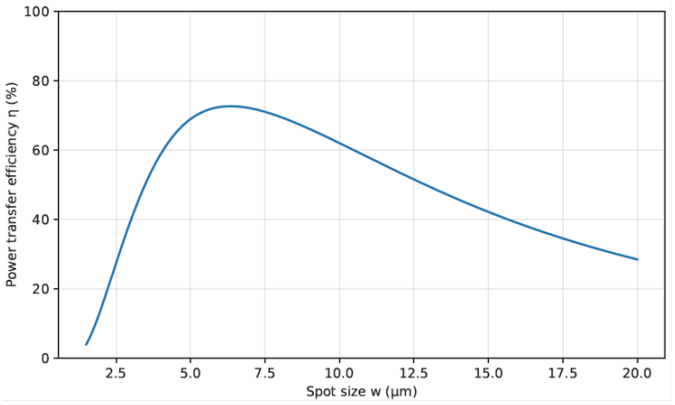


FIGURE 2.18: Calculated power transfer efficiency as a function of Gaussian beam waist, showing an optimum efficiency of approximately 72% at $w \approx 6$ μm due to the balance between junction current matching and optical spillover losses.

Appendix A.2.1, confirms that the external current in series-connected p–n junction circuits is limited by the junction associated with the minimum absorbed optical power. The numerical results are in good agreement with the experimentally observed maximum conversion efficiency of 35% obtained through optimization of beam focus and alignment. The numerical model indicates that Gaussian coupling limits the fraction of incident optical power that can be effectively converted to electrical power to 72%. When this limitation is taken into account, the

corresponding intrinsic photovoltaic efficiency of the triple-junction device under uniform optical excitation is estimated to be approximately 48%. This indicates that further improvements in power transfer efficiency could be achieved by tailoring the optical field distribution at the receiver facet. Although beam-shaping techniques capable of transforming Gaussian beams into flat-top profiles are available, their stringent alignment requirements and sensitivity to source–target geometry limit their applicability in endoscopic power transfer systems, while remaining potentially suitable for other remote optical power delivery applications.

Table 2.1 consolidates the results of this section along with those from the other sections of the chapter, highlighting the key observations.

TABLE 2.1: Summary of edge-coupled laser power conversion configurations investigated in this chapter.

Pump (nm)	**Receiver** (nm)	**Receiver formate**	**Junction type**	**Optical coupling**	η (%)	V_{oc} (V)	V_{max} (V)	**Key observations**
1427	1540	Commercial butterfly packaged	Single junction	Fiber edge-coupled	33	0.83	0.6	High Voc; strong optical pumping enables simultaneous power and data transmission
980	1064	bare die	Single junction	Fiber edge-coupled	23.8	1	0.86	η limited by light–device coupling
850	905	Nanostack laser	Triple junction	Free space edge coupled	35	3.5	3.1	Voltage scaling; η limited by Gaussian illumination
-	-	-	Triple junction	Gaussian model (numerical)	48 (est.)	–	–	Numerical model estimate higher internal η under uniform optical incident

2.5 Conclusion and Discussion

This chapter demonstrated the experimental realization of single and triple junction edge-coupled PPCs operating from telecom to near-infrared wavelengths. The results confirm efficient laser-to-laser optical power transfer, high open-circuit voltages, and the feasibility of combining optical power conversion and data transmission within a single photonic platform. The 1427–1540 nm configuration, the single-junction receiver laser achieved a record open-circuit voltage of 0.83 V and a voltage at the maximum power point of 0.6 V, corresponding to an internal conversion efficiency of 55.3% and an overall fiber-to-device efficiency of 35%. The same device simultaneously operated as a self-powered optical modulator, enabling upstream data transmission up to 500 Mbps without external electrical bias. The fill factor decreased from 63% to 52% with increasing optical injection due to field screening and Auger recombination within the quantum wells, which limited carrier extraction and reduced current near the maximum power point.

At shorter wavelengths (980–1060 nm), the unpackaged bare-chip receiver achieved stronger absorption and improved coupling, delivering a V_{oc} of 1.07 V, efficiency of 23%, and a fill factor of 70% at 10 mW of incident power. Slight fluctuations in photocurrent and FF at higher optical power were caused by coupling instability and optical feedback between the lensed fiber and the receiver facet, emphasizing the sensitivity of coupling alignment in the edge-coupled geometry. The 905 nm triple-junction converter under 850 nm pumping achieved voltage multiplication across the stacked p–n junctions, delivering V_{oc} = 3.6 V, FF = 82%, and peak efficiency of 35% at 10 mW input. However, uniform illumination across the three junctions could not be achieved using Gaussian beam coupling, leading to nonuniform carrier generation and variations in the I–V response.

Overall, the single and triple junction converters delivered approximately 1 V and 3 V at 10 mW of optical input, with efficiencies of 21% and 36%, respectively. Numerical analysis indicates that optimized Gaussian coupling would permit conversion efficiencies of up to approximately 48%, whereas the experimentally measured efficiency of 36% reflects additional losses associated with practical coupling and alignment.

Performance can be improved by reducing the front mirror reflectivity to near zero at the pump wavelength to enhance coupling efficiency. Carrier extraction can be further enhanced through optimization of the extraction-layer doping and through band-structure engineering approaches, such as the incorporation of multiple stepped quantum wells to reduce effective barrier heights

and facilitate carrier escape. The implementation of high-stability mounting fixtures with sub-micron alignment control would further improve coupling robustness. Addressing these limitations will enable higher conversion efficiency, improved operational stability, and reliable performance of edge-coupled PPC.

For triple-junction converters, performance critically depends on achieving a uniform optical intensity distribution across the stacked junctions. Numerical results indicate that transforming the Gaussian pump beam into a flat-top intensity profile would significantly reduce junction-to-junction current imbalance and enable efficiencies beyond the Gaussian-limited value. However, the sub-10 µm receiver aperture is incompatible with commercially available beam-shaping optics, necessitating customized micro-optical or on-chip mode-shaping approaches. Integrated solutions such as tapered or mode-expanding waveguide sections positioned before the absorber offer a practical pathway to achieving uniform illumination at the micrometer scale.

Chapter 3

Surface normal photovoltaic power converter under annular and quasi-Gaussian illumination

3.1 Introduction

In POF applications, the most commonly employed configuration uses surface-normal illumination, in which optical power is directed perpendicular to the top surface of the photovoltaic device to uniformly illuminate its active area. In contrast, the previous chapter demonstrated remote optical powering using an edge-coupled configuration between two waveguide laser. The surface-normal configuration offers practical advantages for compact integration, as light can be directly aligned to the device surface and easily coupled using optical fibers or lenses. By comparison, the edge-coupled approach, despite its efficient optical confinement, presents challenges related to precise facet alignment and achieving uniform illumination across stacked p–n junctions.

For remotely powered microsystems that require operating voltages above 1 V, the literature on high-voltage photovoltaic power converters has been addressed through vertically stacked multijunction and laterally interconnected multi-segment architectures, as outlined in Chapter 1. In this work, the focus is on the laterally segmented design due to its ease of epitaxial growth, as it avoids the need for tunnel junctions and the precise sub-cell thickness control required to achieve current matching in vertically stacked multijunction devices [33]. The PPC

investigated here is intended for integration within a medical catheter, incorporates four laterally series connected segments within a maximum active device diameter of 350 µm on a 1 mm × 1 mm chip. The performance of laterally interconnected PPCs is closely governed by the spatial uniformity of illumination and the geometric configuration of the device segments, which together determine the distribution of photocurrent and the extent of optical loss across the cell.

Optical power is typically delivered through a MMF, where a centered, symmetric illumination such as a Gaussian beam is used to satisfy the requirement of equal current generation in each segment. However, power losses occur due to non-absorption of light incident on isolation trenches and metal interconnects [30, 61]. Additional losses can arise from current mismatch when the light spot is misaligned with respect to the segmented junctions [62, 63]. Because a Gaussian beam exhibits higher intensity at the center of the cell, additional metal fingers are required to reduce the series resistance associated with lateral current spreading. This introduces a trade-off, as the increased metal coverage also limits photon absorption and charge collection within the active area. Although a flat-top rectangular illumination could provide uniform intensity across the segments, its optical losses remain proportional to the total area of isolation trenches and metal lines. These effects become increasingly significant as the number of segments increases or as the active area decreases [10, 63].

To address these limitations, this chapter investigates a beam-shaping approach that redistributes optical power toward the edges of the PPC active area rather than the center. Compared with Gaussian illumination, this approach can reduce current mismatch between laterally interconnected segments and optical loss in trenches and metal lines. The extent of this reduction, however, is strongly dependent on accurate fiber to device alignment, which is therefore treated as a key variable and systematically examined in this chapter. The optical power is delivered to the device through a DCF under two distinct illumination profiles: (i) a quasi-Gaussian beam obtained under normal fiber alignment, and (ii) an annular beam was generated by angularly tilting the input (launch) end of the DCF, thereby concentrating optical intensity toward the periphery of the active area at the fiber output. The DCF was chosen for its potential application in guiding power and data simultaneously [64]. We use the term quasi-Gaussian beam, as the multimode illumination for DCF is not the ideal Gaussian profile. Under non-ideal optical field distributions on the device, the annular illumination configuration is expected to offer advantages by preferentially generating carriers closer to the segment periphery, thereby reducing the lateral transport distance required for photogenerated holes to reach the

collection contacts. As demonstrated by the experimental results presented in this chapter, annular illumination provides superior voltage and fill factor characteristics compared with the quasi-Gaussian case. An open-circuit voltage of 4.77 V was measured at 60 mW under annular illumination, representing a 1.7% increase relative to Gaussian illumination. A slightly lower short-circuit current observed at the nominal fiber to device spacing is attributed to beam spillage, which was mitigated by reducing the fiber to device separation, resulting in power conversion efficiencies of 48.6% at 20.8 W/cm^2 (20 mW) and 47.5% at 62.4 W/cm^2 (60 mW). The chapter also discusses challenges in achieving robust annular beam formation, highlighting the sensitivity of confinement and alignment precision based on the same set of measurements performed on a different PPC chip with identical design and experimental setup.

In parallel with the segmented PPC investigations presented in this chapter, preliminary studies were conducted on a single-junction GaAs PPC with a micro-scale active diameter of 26 µm, coupled under surface-normal illumination using a SMF, as detailed in Appendix A.5.1. This study was undertaken to assess alignment sensitivity, optical confinement, and efficiency trade-offs at extreme device miniaturization, motivated by emerging MCF platforms for simultaneous optical power and data delivery in highly constrained medical catheter environments. While the micro-PPC demonstrated successful optical power conversion, the measured efficiency was limited to approximately 24%, primarily due to enhanced surface recombination and reduced carrier collection efficiency associated with the high perimeter-to-area ratio of the device. These results highlight the fundamental trade-off between footprint reduction and extraction efficiency in micro-scale PPCs, indicating that further optimization of surface passivation, contact design, and optical coupling will be required before such architectures can be effectively deployed in practical remotely powered microsystems.

3.2 Surface normal configuration on PPC

Figure 3.1 (a) illustrates the schematic of light illumination on a multi-segment PPC. The antireflection coating (ARC) on the top surface minimizes optical reflection due to refractive index mismatch and enhances the transmission of incident light into the underlying semiconductor layers. The transmitted light passes through the cap layer, which forms a low-resistance ohmic contact to the emitter. Beneath the cap layer, a heavily doped front surface field (FSF) with a wider bandgap generates a built-in electric field that suppresses minority-carrier (electron) transport toward the top contact, thereby reducing surface and contact related recombination

losses. Below the FSF lie the emitter and base layers, which together form the p–n junction responsible for photocurrent generation.

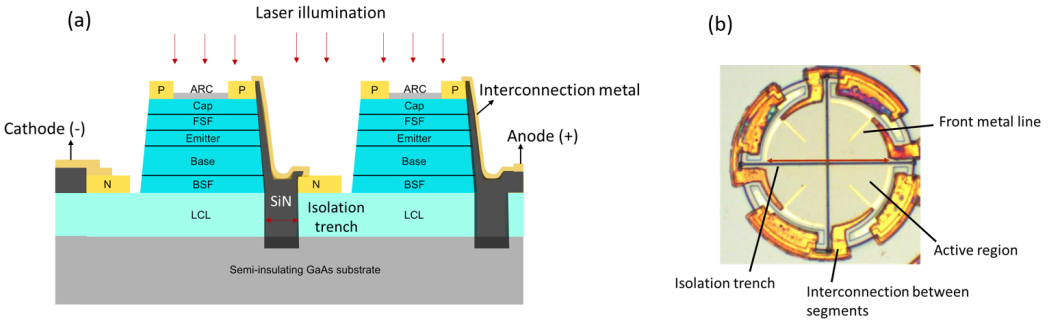


FIGURE 3.1: (a) Cross-sectional schematic of a laterally segmented, surface-normal GaAs PPC, showing the vertical layer structure, isolation trench with SiN for encapsulation, series interconnection metal, and anode and cathode contacts under surface-normal laser illumination. (b) Front view of the circular four-segment laterally connected PPC showing the device layout with isolation trenches (black cross lines) and metal connections; the red arrow indicates the device active diameter.

The thicknesses of the emitter and base layers are selected primarily based on the minority carrier diffusion lengths in each region. In the p-on-n structure employed here, the relatively thin p-type emitter reduces front-surface recombination and allows minority electrons generated near the illuminated surface to reach the depletion region, while the thicker n-type base serves as the primary photon-absorption region and enables minority holes generated within their diffusion length to reach the junction. In the literature, n-on-p configurations are also commonly reported, as the longer diffusion length of minority electrons allows carrier collection over a thicker base region. The vertical layer configuration, with the p-type emitter positioned above the n-type base, enhances carrier collection under surface-normal illumination by generating photocarriers close to the depletion region, where the built-in electric field promotes carrier separation and reduces surface recombination losses. An n-type back surface field (BSF) layer located below the base suppresses minority-carrier recombination at the rear interface by introducing a bandgap induced energy barrier for minority holes. The structure is supported by an n-type lateral conduction layer (LCL) grown on a semi-insulating substrate, which enables lateral current transport between adjacent photoactive segments and allows series interconnection through metallic contacts. The total output voltage in this configuration is equal to the sum of the voltages from the individual segments, while all segments share a common optical path under normal incidence. This is achieved through a laterally segmented device architecture, in which multiple p–n junction segments are defined side by side within the same epitaxial stack and electrically interconnected in series via surface metallization. The active region is divided into four laterally interconnected segments arranged in a pie-shaped geometry to ensure uniform

optical coupling and consistent power distribution across the device, as shown in Figure 3.1 (b). Each segment operates as an independent photovoltaic subcell that is uniformly illuminated, generating a comparable photocurrent, while the series interconnection enables their individual open-circuit voltages to add. As a result, the laterally segmented configuration provides an effective means of voltage scaling that meets system-level power delivery requirements without increasing device thickness or modifying the vertical epitaxial structure.

3.2.1 Device Description

The performance of the PPC under Gaussian and annular illumination was evaluated using a GaAs-based PPC with an active diameter of 350 µm, consisting of four laterally interconnected segments. The epitaxial structure of the device is detailed in Appendix A.3.1, and the device were fabricated at the Tyndall National Institute [34]. The device features a circular active area designed to match the circularly symmetric light spot emitted from the optical fiber under surface-normal illumination.

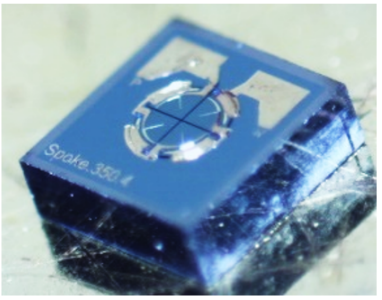


FIGURE 3.2: (a) Picture of 1 mm × 1 mm chip with four segments laterally interconnected PPC with active diameter of 350 µm.

Electrical isolation between the four segments is achieved through isolation trenches etched into the substrate, while interconnection metals bridge these isolated regions, forming a unified circuit configuration that enables efficient current flow and voltage addition across the entire device. The presence of isolation trenches and metal lines introduces optical losses by partially covering the illuminated active area. The areas occupied by the 3 µm wide isolation trenches and metal lines correspond to 2.2% and 1.4% of the total active area, respectively, as calculated from Equations 3.1 and 3.2. These values represent the portions of the active region covered by non absorbing structure reducing the effective area available for optical absorption. Figure 3.2 shows Chip 1, a diced device with lateral dimensions of 1 mm × 1 mm and an overall thickness as 0.37 mm.

3.2.2 Optical losses in segmented PPC

Optical losses in laterally segmented PPC designs arise primarily from isolation trenches and front metal interconnects. Under surface-normal illumination, these non-active regions introduce shadowing, reflection, and scattering losses. The magnitude of such losses is governed by the ratio of non-photoactive area to the total illuminated surface, which increases with both the number of series-connected segments and the width of the isolation and interconnect features.

The isolation trenches, which provide electrical separation between adjacent sub-cells, form optical discontinuities that scatter or absorb a portion of the incident light. In this work, the trench width is constrained to a minimum value determined by the fabrication process which is 3 µm, and the cumulative optical loss associated with these regions therefore increases with the degree of lateral segmentation. Similarly, surface metal interconnects are required to enable series current transport but partially obstruct the optical beam and reflect photons away from the photoactive regions.

Although thicker metallization typically several micrometers is commonly used in conventional photovoltaic designs to reduce series resistance, such an approach is not adopted here due to geometric and optical constraints. Instead, relatively thin metal lines are employed to balance current transport requirements against optical shading losses, a trade-off that becomes increasingly significant as the segment count increases. Collectively, these effects reduce the optical power available for carrier generation within the junction and constitute a key limitation in highly segmented devices.

The magnitude of these losses can be expressed analytically through the fractional area occupied by isolation trenches and metal interconnects. The isolation loss ($L_{\text{isolation}}$) is determined by the fraction of surface area removed for electrical isolation, where A_{trench} denotes the total area of the isolation trenches on the illuminated device surface, and is defined as 3.1.

$$L_{\text{isolation}} = \frac{A_{\text{trench}}}{A_{\text{device}}} \times 100\% \tag{3.1}$$

The shading loss (L_{shading}) represents the reduction in effective illumination caused by metal coverage and is given by 3.2,

$$L_{\text{shading}} = \frac{A_{\text{grid metal}}}{A_{\text{device}}} \times 100\% \tag{3.2}$$

where $A_{\text{grid metal}}$ is the total area covered by the front metal grid and A_{device} is the total illuminated device active area. Increasing the density of metal lines reduces the lateral series resistance but increases optical shadowing, representing a trade-off between electrical performance and optical transparency. As the physical dimensions of the device decrease, the relative contributions of A_{trench} and $A_{\text{grid metal}}$ become more significant, leading to higher fractional optical loss in small area PPC. The total optical loss is therefore determined jointly by the device geometry and illumination parameters, which together define the irradiance uniformity, beam confinement, and optical coupling efficiency under surface-normal operation.

3.2.3 Fiber to device distance determination

The optimum fiber-to-device distance (G) was estimated geometrically from the divergence of light emerging from the fiber core, as illustrated in Figure 3.3. When light exits the fiber into air, it expands conically with an emission half-angle (θ) determined by the numerical aperture (NA) of the fiber, expressed in 3.3,

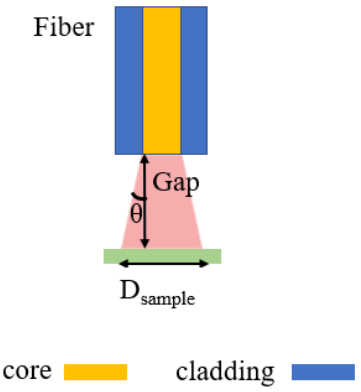


FIGURE 3.3: Schematic of the surface-normal illumination geometry showing the fiber-to-device distance (G). The emitted beam diverges from the fiber core at an angle θ, expanding to a diameter D_{sample} that defines the illuminated area on the PPC surface.

$$\theta = \sin^{-1}\left(\frac{NA}{n_{\text{air}}}\right) \tag{3.3}$$

where n_{air} is the refractive index of air. The NA defines the maximum acceptance angle of guided modes in the fiber and depends on the refractive index contrast between the core (n_{core}) and cladding (n_{clad}) according to 3.4

$$NA = \sqrt{n_{\text{core}}^2 - n_{\text{clad}}^2} \tag{3.4}$$

When the fiber is positioned at a distance G above the PPC surface, the divergent beam expands from the fiber core diameter (D_{core}) to an effective illumination active diameter of sample (D_{sample}). Assuming simple geometric expansion with negligible diffraction, the relationship between these parameters can be written as

$$r_{\text{sample}} = r_{\text{core}} + (G)\tan(\theta), \tag{3.5}$$

or equivalently,

$$G = \frac{r_{\text{sample}} - r_{\text{core}}}{\tan(\theta)}, \tag{3.6}$$

where $r_{\text{core}} = D_{\text{core}}/2$ and $r_{\text{sample}} = D_{\text{sample}}/2$.

Physically, this relation illustrates how the divergence of the optical cone emerging from the fiber determines the illuminated spot size on the photovoltaic power converter (PPC). In this configuration, direct fiber-to-device illumination is employed, and the illumination footprint is controlled by adjusting the fiber-to-device separation. The beam divergence defined by the fiber numerical aperture, together with the short working distance, allows the expanded beam to be matched to the device aperture without the use of additional focusing optics. By appropriately positioning the fiber at a distance from the device surface, effective beam coverage of the designed active area is achieved under surface-normal incidence.

3.3 Experimental design on quasi-Gaussian and annular illumination on four segment PPC

Here, we present a comparative and parametric experimental investigation of two GaAs-based four-segment GaAs PPC devices with identical design layouts and epitaxial structures, evaluated under quasi-Gaussian and annular illumination in a surface-normal configuration. The first device (Chip 1) was employed to compare the two illumination profiles at fiber to device distances up to 600 µm, which corresponds to the theoretically estimated optimal coupling distance to match active diameter (discussed in section 3.3.2). The second device (Chip 2), fabricated from a different wafer but following the same design, was characterized over an

extended distance range (0.4–1 mm) to further examine the effect of beam expansion and to validate the reproducibility of the observed performance trends.

3.3.1 Generation of Annular Illumination

The use of annular illumination in this work is motivated by an initial design concept in which an optical modulator is integrated at the center of the PPC, making an annular (ring-shaped) spatial intensity distribution desirable. In practice, an annular beam can be generated by coupling a laser beam into a multimode optical fiber at a nonzero incidence angle relative to the fiber axis [65–68]. When the input beam enters the fiber off-axis, the guided rays propagate along helical trajectories near the periphery of the multimode region rather than through its center. The interference among these higher-order modes redistributes the optical intensity, producing a dark central region surrounded by a bright annular ring at the fiber output. These higher-order modes exhibit increased field intensity near the core–cladding interface, resulting in a higher modal density toward the fiber periphery and reinforcing the annular intensity distribution. By carefully adjusting the incidence angle, the spatial energy distribution can be optimized to obtain a well-defined annular beam with a smooth intensity profile. This approach provides a practical method for generating ring-shaped beams because the annular profile is produced by controlled mode excitation in the multimode fiber, rather than by using additional beam-shaping optics, such as axicons [69] or phase-modifying elements [68], to redistribute the incident optical field into an annular intensity profile.

Figure 3.4 illustrates the experimental setup for generating and projecting an annular beam onto the PPC under surface-normal illumination. The configuration employs angular launching of an 851 nm laser beam into the input end of the DCF, resulting in an annular intensity profile at the fiber output. A fiber coupled diode laser emitting at a wavelength of 851 nm serves as the optical source. The laser output is delivered through a SMF with a core diameter of 4.4 µm. The output from the SMF is collimated using a plano-convex lens (L1) with a focal length of 18.4 mm, producing a collimated beam of uniform divergence. The collimated beam is then focused into the input facet of the DCF using a biconvex lens (L2) with a focal length of 25 mm. The DCF consists of a 9 µm diameter single mode central core with a NA of 0.12, surrounded by a 105 µm multimode inner cladding with an NA of 0.2. As the central core supports single mode guidance only at 1550 nm, the 851 nm beam propagates in the multimode inner cladding, which effectively acts as the guiding region for this wavelength. Annular beam

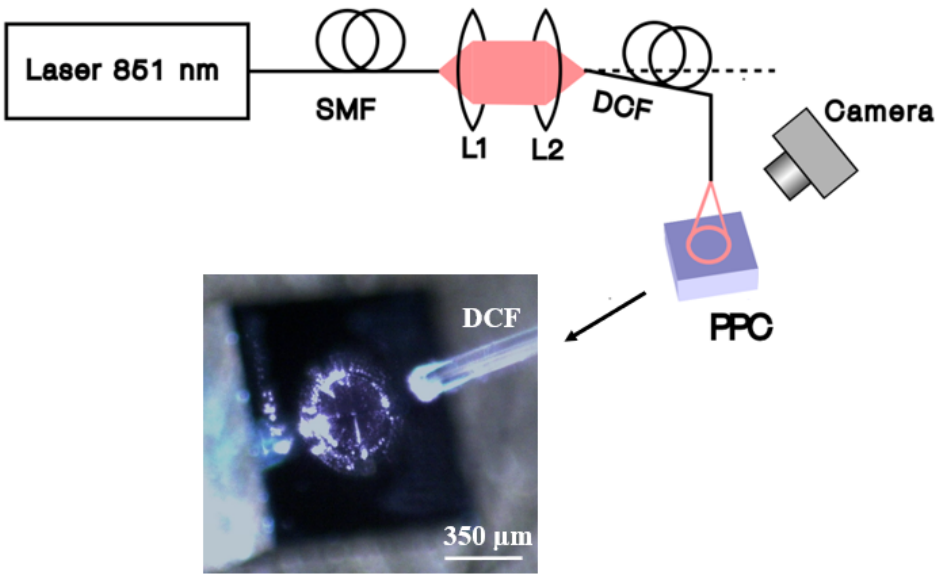


FIGURE 3.4: Experimental setup for annular beam illumination on the PPC. SMF; Single mode fiber coupled laser, L1 collimator focal length= 18.4 mm, L2 Biconvex lens focal length= 25 mm, DCF; double clad fiber (DCF-13 Thorlabs).The inserted picture shows diced chip under annular illumination at a fiber to device distance of 600 µm, recorded using a Dino-Eye Edge digital microscope (AM4025X model).

formation was achieved by introducing an angular launch into the DCF. The input end of the DCF was mounted on a precision XYZ translation and rotation stage, allowing fine angular and positional alignment relative to the optical axis of the focusing lens (L2). The coupling efficiency was maximized by carefully adjusting the DCF position while gradually increasing the launch angle. As the tilt angle increased, the excitation within the multimode inner cladding transitioned from centrally guided modes to higher-order ring modes. At an incidence angle of 18 degrees, an annular intensity distribution was observed at the DCF output, confirming the excitation of the desired annular-mode pattern. At this off-axis launch condition, the coupling efficiency was reduced to approximately 33%, reflecting the known trade-off between optical coupling efficiency and spatial beam shaping. This reduction arises from the increased angular mismatch and partial rejection of rays approaching the acceptance limit of the multimode inner cladding, rather than from misalignment or coupling instability.

Beam characterization and calibration were performed prior to device illumination. The fiber-to-device distance was set to approximately 600 µm, as determined from Equation 3.6 using the DCF parameters of NA = 0.2 and an inner cladding diameter of 105 µm. This configuration ensured that the annular beam illuminates the near the edge of the 350 µm active area of the PPC. The output from the DCF was projected onto a diffuse paper screen, and the resulting pattern was captured using a Dino-Eye Edge A.4 camera positioned at a 45 degrees angle

relative to the surface-normal direction. An absorptive filter is placed before the biconvex lens to reduce the laser power and avoid saturation of the image.

3.3.2 Beam Characterization and Calibration

The USAF 1951 resolution target was used to establish the pixel-to-length calibration of the imaging system by providing a known spatial reference. This calibration enabled conversion of the measured beam dimensions from pixels to micrometers during ImageJ analysis. The image captured by the camera appeared slightly elliptical because the 45 degrees observation angle introduced projection distortion along the viewing axis. To ensure accurate dimensional analysis during calibration, the 1D beam profile was evaluated along the plane unaffected by projection, corresponding to the non-distorted axis that represents the true beam diameter in the PPC plane.

Manual adjustments of the DCF position at the input (launch) end of the fiber, where the laser beam is coupled into the DCF through the launch optics, were performed using an XYZ translation stage to refine the annular beam diameter while continuously monitoring the coupling efficiency. Through this iterative alignment process, the annular beam diameter was adjusted to 350 µm at a fiber to device distance of 600 µm without degrading the optimized coupling condition. The final beam diameter was confirmed through ImageJ profile analysis, which showed consistent fitting results before and after alignment, verifying that the optimized configuration maintained both beam uniformity and maximum coupling efficiency. Under these calibrated conditions, a coupling efficiency of approximately 33% was achieved, defined as the ratio of optical power measured at the DCF output facet prior to device illumination to the optical power delivered by the laser before entering the lens-based launch system. For comparison, previous literature has shown coupling efficiencies greater than 60% using MMF with higher NA (e.g., NA = 0.37) and larger core diameters (up to 800 µm) [70]. Similarly, in a Thorlabs study [71], a 200 µm core multimode fiber with an NA of 0.39 produced an annular beam of approximately 1 mm diameter. In this work, the experimental focus was on generating an annular beam matched to the 350 µm active diameter of the PPC using the DCF configuration described above. Consequently, optimization of coupling efficiency through the selection of a higher-NA fiber was not pursued, as the primary objective was to evaluate the performance of the PPC under controlled annular beam illumination at this beam diameter. Following beam

verification and optimization, the annular beam was directed onto the PPC under surface-normal incidence. This ensured uniform illumination of the device's active region and optical coupling for subsequent evaluation of PPC performance under annular beam illumination.

3.3.3 Quasi-Gaussian and annular beam analysis

A quasi-Gaussian beam was generated using the same optical setup by launching the laser beam on-axis into the DCF at the laser–to–fiber input interface, resulting in a coupling efficiency of approximately 96%. In this configuration, the beam profile emerging from the DCF corresponds to the native multimode output under on-axis excitation, and no additional beam shaping was required prior to device illumination. The launch optics were adjusted solely to maximize the optical power delivered from the DCF onto the PPC at a fixed fiber-to-device separation. As optimization of the Gaussian beam shape was not part of the calibration procedure. In contrast, annular beam formation required off-axis launching of the laser beam into the DCF to excite higher-order modes and redistribute optical power toward the fiber periphery. In this case, the annular beam diameter needed to be matched to the PPC active aperture, and therefore beam calibration and characterization were performed prior to device illumination.

The image was captured for fiber to device distance of 400 µm and 500 µm and the theoretically calculated distance of 600 µm. To estimate beam coverage within the device active region, the quasi-Gaussian beam image was fitted with a two-dimensional Gaussian function to determine the beam center and full width at half maximum. The fitted profile was then overlaid with a 350 µm-diameter circular mask representing the PPC active area, and the integrated optical intensity within this region was calculated. The Python scripts used for beam processing, fitting, and intensity integration are provided in Appendix A.6.

To establish the nature of the beam profile under on-axis excitation, one-dimensional (1D) intensity profiles were extracted along the x and y axis through the beam center at a fiber-to-device distance of 600 µm. As shown in Figure 3.5, the 1D line scans along both directions exhibit a single dominant central maximum with intensity decreasing toward the edges, indicating a centrally weighted intensity distribution in both axes. However, unlike an ideal single-mode Gaussian beam, the measured profiles display pronounced local intensity fluctuations superimposed on the overall intensity distribution. These oscillations arise from speckle generated by multimode interference within the DCF and are clearly visible in both the two-dimensional (2D) intensity map and the corresponding 1D profiles. Despite the presence of

speckle, the overall intensity distribution remains bell-shaped and centrally peaked along both axes when averaged over local fluctuations, indicating that the majority of the optical power is concentrated near the beam center. For the purposes of this work, the beam is therefore described as quasi-Gaussian, reflecting a Gaussian-like spatial energy distribution modified by multimode speckle rather than an ideal Gaussian profile.

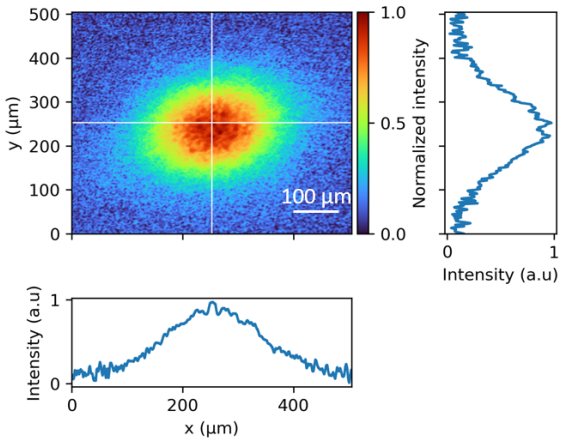


FIGURE 3.5: One-dimensional line scans along the x and y direction through the center of the quasi-Gaussian beam recorded on a diffusive imaging surface at a fiber to imaging plane distance of 600 µm. The profiles show a centrally peaked, Gaussian-like intensity distribution with superimposed fluctuations arising from multimode speckle.

Figure 3.6 (a) presents the corresponding two-dimensional (2D) normalized intensity distributions of the quasi-Gaussian beam at fiber-to-device distances of 400 µm, 500 µm, and the theoretically calculated distance of 600 µm, with a 350 µm circular disk overlaid to represent the PPC active area. The 2D images reveal spatially random speckle patterns with localized high-intensity regions, which arise from multimode propagation within the DCF. As indicated by the 1D line scans in Fig. 3.6, these speckle-induced variations are superimposed on an overall centrally weighted intensity distribution.

At a fiber-to-device distance of 400 µm, the optical intensity is strongly concentrated near the center of the active region, resulting in high beam coverage within the device aperture. As the distance increases to 600 µm, the beam expands laterally and the intensity becomes more broadly distributed across the active area. This redistribution improves the illumination uniformity across the four laterally interconnected segments, but it also causes an increasing fraction of the optical power to extend beyond the active region, resulting in spillage losses. The estimated beam coverage within the 350 µm active diameter decreases from approximately 91% at 400 µm to 86% and 80% at 500 µm and 600 µm, respectively.

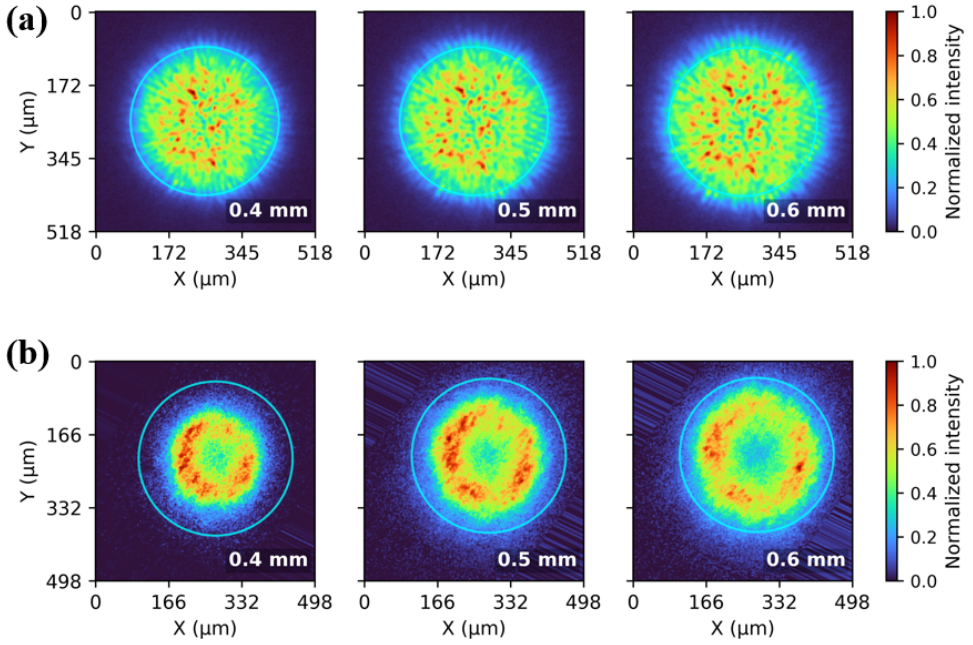


FIGURE 3.6: Normalized two-dimensional intensity distributions of the beams recorded at fiber-to-device distances of 400 µm, 500 µm, and 600 µm (left to right), with a 350 µm circular disk overlaid to represent the PPC active area. Each panel corresponds to an independently acquired beam image at the indicated fiber-to-device distance. (a) Quasi-Gaussian beam. (b) Annular beam.

For annular beam image analysis, the captured images were geometrically corrected through rotation and homographic (projective) transformation, which maps the tilted image plane to an equivalent on-axis view, prior to overlap with the 350 µm circular disk and subsequent intensity integration. Figure 3.6 (b) presents the normalized two-dimensional intensity distributions of the annular beam at fiber-to-device distances of 400 µm, 500 µm, and 600 µm. In contrast to the quasi-Gaussian illumination shown in Fig. 3.6 (a), the annular beam redistributes optical power away from the center of the active area and concentrates intensity along a ring positioned near the periphery of the 350 µm disk, thereby reducing central spillage and improving confinement within the active region.

As the fiber-to-device separation increases from 400 µm to 600 µm, the annular beam expands radially, causing the high-intensity ring to broaden and shift toward the edge of the active area, with a corresponding increase in optical power spillage. At an intermediate separation of 500 µm, the annular ring remains relatively compact and continuous, whereas at 600 µm it becomes less confined and partially extends beyond the active region. Conversely, at smaller separations, the annular ring is narrower and more uniformly confined within the active area, exhibiting a more continuous red–yellow intensity distribution around the circumference.

Quantitatively, the estimated beam coverage within the active region is 97%, 90%, and 85% for fiber-to-device distances of 400 µm, 500 µm, and 600 µm, respectively. In addition to the increased confinement at smaller separations, the annular intensity distribution becomes more radially compact and circumferentially continuous. Since each of the four PPC segments occupies an angular sector of the circular active area, this increased circumferential continuity implies a more uniform average optical power intercepted by each segment. This evolution of the annular beam profile is therefore expected to mitigate photocurrent mismatch in the series-connected PPC, with the corresponding electrical behavior discussed in the following section.

3.3.4 Distance-Dependent Illumination Performance on Chip 1

3.3.4.1 I–V characteristics

Accurate alignment of the DCF output end with the PPC was performed as a calibration step to ensure maximum optical coupling, achieved by monitoring the I_{sc} under illumination. This alignment was carried out using an XYZ motorized stage attached to the DCF fiber end, allowing precise adjustment to match the illuminated profile across all four segments of the device. Any misalignment leads to non-uniform illumination, causing the segment with the lowest current to limit the overall current in the series-connected PPC. The photovoltaic I–V characteristics of the 350 µm diameter four-segment PPC under quasi-Gaussian and annular beam illumination are presented in Figure 3.7. For comparison purposes, the I–V curves are plotted using an inverted current convention so that the operating region is displayed in the first quadrant. The measurements were performed by varying the optical power at the output of the DCF from 0 to 60 mW, which corresponds to the incident optical power (P_{illum}) delivered to the device surface. The same power range was maintained for both illumination profiles to enable a direct comparison of their performance, the upper limit of P_{illum} is limited by the coupling loss associated with generating the annular beam.

An increase in illumination power P_{illum} increases, the I–V characteristics under quasi-Gaussian illumination exhibit a progressive reduction in the slope of the curve in the high-voltage region approaching open-circuit conditions. This behavior is indicative of an increase in the effective series resistance. In the laterally segmented PPC architecture, higher optical power leads to increased photocurrent density concentrated near the center of the device, which in

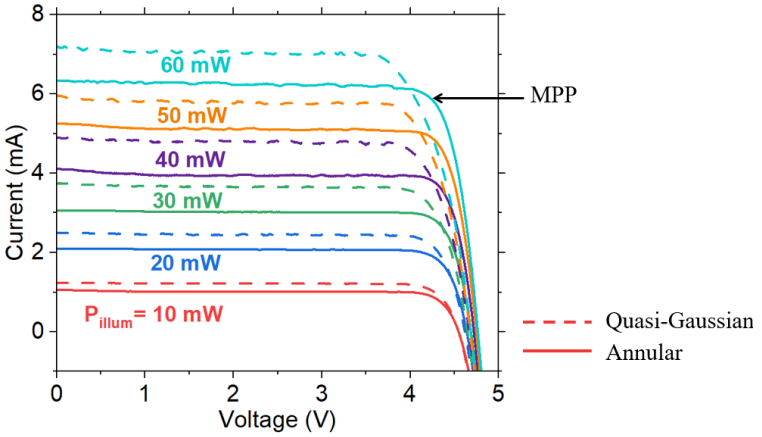


FIGURE 3.7: Comparison of the I–V characteristics of the 350 µm diameter four-segment PPC under Gaussian and annular illumination at 851 nm, measured for varying DCF output power levels (P_{illum}) from 0 mW to 60 mW at a fiber-to-device separation of 600 µm.

turn enhances lateral current spreading toward the interconnection regions. The resulting increase in lateral spreading resistance, together with temperature-dependent resistivity of the semiconductor layers and metal contacts under elevated current densities, contributes to a rise in effective series resistance. This manifests as a reduction in FF and a decrease in the V_{oc} at higher illumination powers. In contrast, annular illumination generates a lower total photocurrent but distributes the optical intensity toward the periphery of the four-segment PPC, closer to the current-collection paths. This spatial redistribution reduces lateral current transport distances and mitigates increases in spreading resistance, resulting in a more stable series resistance with increasing P_{illum}. Although a portion of the annular beam overlaps with the interconnection metal and isolation regions—reducing the effective photoactive area and hence the generated current—the reduced resistive losses enable the annularly illuminated device to maintain a higher V_{oc} at P_{illum} 60 mW compared with the quasi-Gaussian case. Conversely, quasi-Gaussian illumination produces a higher photocurrent due to broader coverage of the active segments, but this comes at the expense of increased series resistance, leading to lower V_{oc} and fill factor at high illumination powers.

3.3.4.2 Analysis of open-circuit voltage and short circuit current

Figure 3.8 (a) presents the variation of V_{oc} as a function of incident optical power for both quasi-Gaussian and annular illumination profiles at different fiber to device separations. The measured V_{oc} representing the combined output of the four-segment PPC and exhibits a logarithmic increase with rising illumination power, consistent with the expected diode behavior

of PV devices described by Equation 2.4. The V_{oc} values obtained in this work are notably higher than those reported for four-junction vertically stacked converters in [72]. Under annular illumination at fiber to device distance of 600 µm, V_{oc} reaches a maximum value of 4.77 V at an incident optical power of 60 mW, corresponding to an average per-cell open-circuit voltage of approximately 1.19 V. This represents an improvement of approximately 1.7% compared to the quasi-Gaussian illumination case at the same optical power. As the fiber-to-device distance increases, variations in V_{oc} remain relatively small due to its logarithmic dependence on the effective illumination level, particularly when compared with the corresponding changes observed in the I_{sc}.

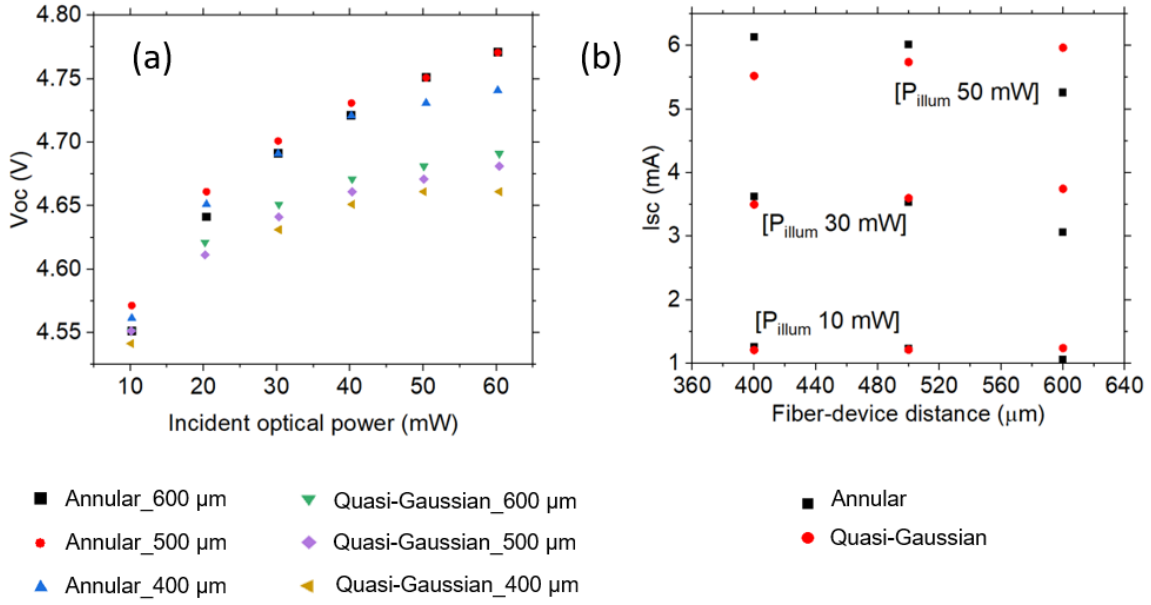


FIGURE 3.8: Comparison of quasi-Gaussian and annular beam illumination on the four segment PPC at fiber to device separations of 400 µm, 500 µm, and 600 µm for varying incident optical powers: (a) V_{oc} and (b) I_{sc}.

The circular PPC segment has a diameter of 350 µm and is illuminated with up to 60 mW, corresponding to an optical power density of approximately 62 W/cm^2. A slight reduction in V_{oc} is observed when the fiber-to-device separation is decreased, with the value dropping to 4.74 V at 60 mW. This behavior can be attributed to the annular beam becoming more confined within the active area at smaller separations, resulting in reduced light spillage but increased localized optical intensity and enhanced recombination losses near the illuminated region. Overall, annular illumination exhibits higher and more gradually saturating V_{oc} values with increasing optical power compared to the quasi-Gaussian beam, indicating a more stable voltage response under annular illumination conditions.

The I_{sc} of the four-segment PPC directly reflects how effectively the quasi-Gaussian and annular beams illuminate the device. Any non-uniform illumination across the segments leads to a reduction in total current. The influence of beam confinement and illumination profile on I_{sc} is shown in Figure 3.8 (b). At a fiber-to-device separation of 600 µm, annular illumination has a slightly lower I_{sc} (1 mA) than the quasi-Gaussian beam (1.24 mW) at 10 mW of illumination. This difference more pronounced at higher illumination power at 50 mW of illumination where annular beam illumination results in an I_{sc} of 5.26 mA, compared to quasi-Gaussian beam of 6 mA. This behavior occurs despite the higher optical confinement achieved by the annular beam within the 350 µm active area and is consistent with the beam analysis in Figure 3.6, which shows that at this separation the annular intensity distribution is confined but not yet evenly distributed around the ring. The resulting segment-to-segment illumination imbalance limits the collected current in the series-connected PPC.

As the fiber-to-device separation is reduced, the annular beam becomes more compact and its intensity distribution more evenly distributed around the active area, as discussed in the beam analysis. At a separation of 500 µm, the improved circumferential distribution of optical power leads to comparable I_{sc} values for annular and quasi-Gaussian illumination. With a further reduction to 400 µm, the annular beam provides a more uniform overlap with all four segments, resulting in a higher measured I_{sc} with increasing P_{illum}. This trend confirms that, in addition to optical confinement, uniform intensity distribution across the segments is a key factor in maximizing current in the four-segment PPC.

3.3.4.3 Voltage at maximum power point V_{max}

The maximum voltage delivered, extracted from the maximum operating point of the I–V curve, is presented in Figure 3.9, showing the variation of V_{max} as a function of incident optical power under quasi-Gaussian and annular beam illumination for different fiber-to-device separations. Under quasi-Gaussian illumination at the 600 µm fiber-to-device distance, V_{max} decreases monotonically from 4.07 V to 3.74 V as the incident optical power increases from 10 mW to 60 mW. This decline is attributed to increased series resistance at higher illumination levels, which introduces resistive voltage losses under high-current operation and limits the effective extraction of charge at the operating point. In contrast, annular illumination exhibits an opposite trend, with V_{max} increasing from 4.07 V to 4.18 V which is 2.7% improvement over the same power range. At 60 mW, V_{max} under annular illumination is approximately 11.7%

higher than that obtained with the quasi-Gaussian beam, indicating superior voltage retention. When the fiber-to-device separation is reduced to 400 µm, under annular illumination V_{max} remains relatively high 4.09 V at 60 mW, compared with 3.72 V for quasi-Gaussian illumination.

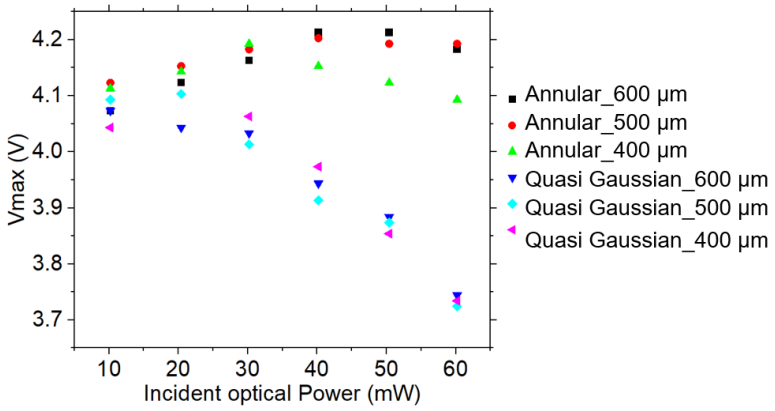


FIGURE 3.9: Voltage at the maximum power point V_{max} of the four-segment PPC under quasi-Gaussian and annular beam illumination at an incident power of 60 mW. Measurements were performed for fiber to device separations of 600 µm, 500 µm, and 400 µm. The annular illumination exhibits a higher V_{max} 4.18 V at 60 mW of incident power.

3.3.4.4 Efficiency and fill factor

Figure 3.10 presents the η and FF of the four-segment PPC, which were extracted for fiber-to-device separations of 400 µm, 500 µm and 600 µm. At lower fiber to device distance 400 µm, annular beam illumination on PPC exbihits higher η of 48.6% and a FF of 84.4% at 20 mW incident power, as shown in Figure 3.10 (a). The relatively high performance at this distance results from the annular beam illuminating uniformly across all four segments, with improved confinement within the active area. In contrast, the quasi-Gaussian beam offers a smaller effective illumination area due to its reduced spot size, even though the beam remains well confined within the active region. As the illumination power increases to 60 mW, η and FF decrease slightly to 47.5% and 81.8%, respectively, indicating minimal performance degradation.

At a separation of 500 µm, the annular beam remains well aligned with the active region, resulting in an η of 47.6% and an FF of 82.6% at 60 mW, as shown in Figure 3.10 (b). In comparison, under quasi-Gaussian illumination at both 400 µm and 500 µm separations, η and FF exhibit a more gradual reduction with increasing optical power, indicating greater sensitivity to power-dependent losses. Across all fiber-to-device distances, the quasi-Gaussian illumination exhibits a more pronounced reduction in fill factor with increasing incident power,

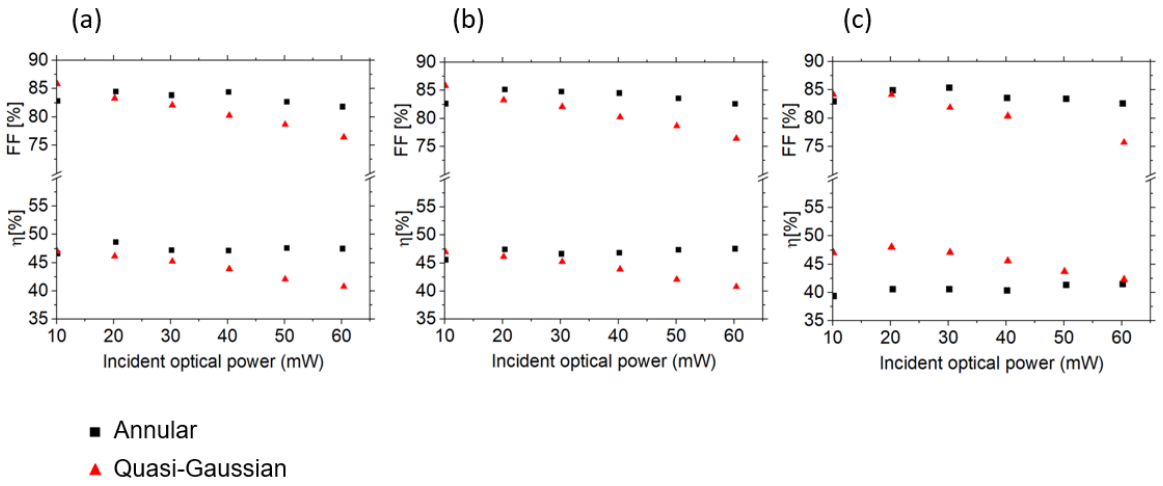


FIGURE 3.10: Variation of power conversion efficiency η and FF with incident optical power for the four segment PPC under annular and quasi-Gaussian illumination at fiber to device separations of (a) 400 µm, (b) 500 µm and (c) 600 µm.

which contributes to the corresponding decrease in power conversion efficiency at higher illumination levels. At the geometrically estimated optimal fiber-to-device distance of 600 µm, the device achieves a maximum η of 48% under quasi-Gaussian illumination and 40% under annular illumination at 20 mW, as shown in Figure 3.10 (c). The lower η observed under annular illumination at this spacing arises from reduced beam confinement within the active area, as a portion of the ring-shaped beam extends beyond the device boundary, thereby decreasing the effective light absorption region and limiting generated electric power.

3.4 Validation and extended-distance analysis using chip 2

Following the characterization of Chip 1, a second device fabricated with the same four-segment GaAs PPC structure was investigated using an identical surface-normal illumination configuration to assess the reproducibility of the observed distance-dependent trends and to explore the effects of increased fiber-to-device separation. For quasi-Gaussian illumination, the separation distance was extended beyond 0.6 mm to examine how beam divergence and speckle evolution from the multimode DCF influence the illumination profile, optical coverage, and resulting photovoltaic response. Although a separation of approximately 0.6 mm corresponds to the theoretically estimated distance that best matches the 350 µm device diameter, extending this range provides insight into the onset of beam overspill and reduced coupling efficiency at larger distances.

In contrast, annular illumination measurements were intentionally limited to fiber-to-device distances of 0.6 mm and below, where effective overlap with the active region is maintained, in order to validate the reproducibility of annular beam confinement and coupling behavior across devices. The setup was calibrated under annular illumination, yielding a coupling efficiency of approximately 35%, closely matching that obtained for Chip 1 under equivalent conditions. Together, these measurements enable a systematic evaluation of beam confinement, active-area coverage, and PV performance on a second device, allowing direct comparison with the trends established using Chip 1.

3.4.1 Beam characterization and illumination analysis on chip 2

The method used for analyzing the images of annular and quasi-Gaussian illumination for Chip 1 was also applied to Chip 2, with the main difference being that both illumination types were captured at a 45° viewing angle to enable a systematic comparison under identical conditions. Figure 3.11 presents the quasi-Gaussian beam intensity distribution for Chip 2 at various fiber-to-device distances ranging from 0.4 mm to 2 mm. The captured images were geometrically corrected through rotation and homographic transformation to represent the intensity profiles in an equivalent on-axis view, as described previously, for consistent analysis. The background in the corrected profiles appears slightly scattered due to diffuse reflections and noise introduced by the diffuse paper used during imaging, and this background noise was accounted for in the beam spillage estimation.

The quasi-Gaussian intensity distributions exhibit characteristic speckled patterns associated with multimode propagation within the DCF, which persist across all distances and become more apparent as the beam expands. As the fiber-to-device separation increases from 0.4 mm to 1 mm, the beam envelope broadens progressively, with localized high-intensity regions distributed across the active area. At shorter distances between 0.4 mm and 0.6 mm, the illumination remains centrally confined within the 350 µm active diameter, indicating effective optical confinement. When the separation is increased to 0.7 mm, the intensity distribution occupies most of the circular disk while remaining largely confined within the 350 µm active diameter, corresponding to approximately 95% active area coverage. This observation suggests that the full NA of the fiber is not sampled, with optical power predominantly carried by near-axis modes. Further increases in separation lead to overspill beyond the device boundary and a corresponding reduction in central intensity.

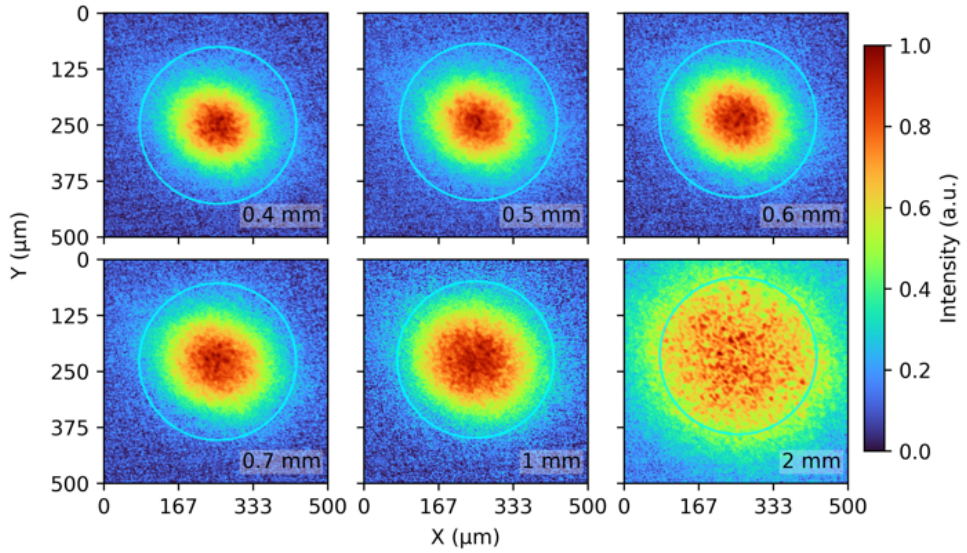


FIGURE 3.11: Quasi-Gaussian beam intensity distributions overlapped with a 350 µm circular disk representing the PPC active region, plotted for fiber-to-device distances ranging from 0.4 mm to 2 mm.

This monotonic increase in beam diameter with propagation distance, as observed in Figure 3.11, is indicative of geometric divergence governed by the numerical aperture of the multimode of DCF. Because the fiber NA fixes the angular distribution of light existing the DCF output end, increasing the fiber-to-device distance converts this angular spread into a larger transverse beam footprint without introducing abrupt changes in beam shape. The presence of speckle at all distances indicates that the DCF output remains multimode, and that the reduced confinement observed at larger separations is mainly caused by geometric beam spreading rather than by changes in the modal distribution.

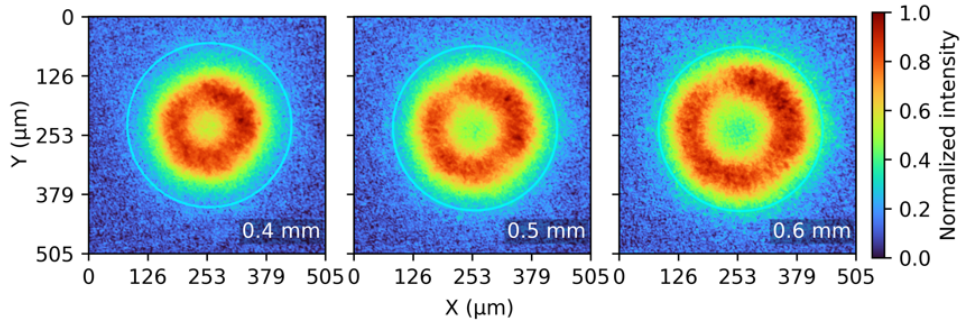


FIGURE 3.12: Annular beam intensity distributions overlapped with a 350 µm circular disk representing the PPC active region, plotted for fiber-to-device distances ranging from 0.4 mm, 0.5 mm and 0.6 mm.

Figure 3.12 shows the annular beam intensity profiles at fiber to device distances of 0.4 mm, 0.5 mm, and 0.6 mm. With increasing fiber to device distance, the annular intensity distribution

becomes more clearly defined, with a high-intensity ring surrounding a lower-intensity central region. At 0.4 mm, the beam provides about 97% coverage of the active area with a strong central confinement. Increasing the spacing to 0.5 mm causes the ring to expand outward, with the high-intensity region approaching the disk edge and the outer intensity beginning to spill beyond it. At 0.6 mm, the annular diameter nearly coincides with the boundary, showing greater overspill compared to smaller spacings. This progression illustrates how adjusting the fiber-to-device distance influences the annular beam diameter and spatial confinement. It should be noted, however, that the coverage estimates are approximate, as the beam images were captured under 45° conditions. Subsequent on-axis correction through homographic transformation may lead to a marginal reduction in apparent beam size due to the soft beam edges and projection effects.

3.4.2 Distance-dependence on-chip beam confinement

Figure 3.13 shows the illumination distribution on the four segment GaAs PPC captured by a camera positioned at a 45 degrees angle with respect to the device surface. The output end of the DCF was positioned at different fiber-to-device distances ranging from 0.4 mm to 2 mm to observe the evolution of the quasi-Gaussian beam on the device surface. At larger separations of 2 mm, the optical beam clearly overspills the 350 µm active area, and strong reflections from the interconnection metals and the central trench-intersection region, are visible. At a distance of 1 mm, the beam remains distributed across the four segments but partial overspill onto the metallic interconnections can still be observed. When the spacing is reduced to 0.7 mm, the beam becomes more confined within the device boundary, and reflections from the interconnection metals are no longer visible.

Further decreasing the distance from 0.6 mm to 0.4 mm results in the illumination shifting toward the device center, producing a more concentrated and uniform intensity profile across the active region. These observations indicate that, under quasi-Gaussian illumination, optimal beam coverage on the PPC surface occurs at a fiber-to-device spacing of approximately 0.7 mm, which closely corresponds to the theoretical value of 0.6 mm estimated for multimode DCF illumination.

The captured image of the annular beam projected onto the device is shown in 3.14. At a fiber-to-device distance of 0.4 mm, the annular beam effectively illuminates the active area, although slight spillage onto the interconnection metal design is observed. As the distance increases to

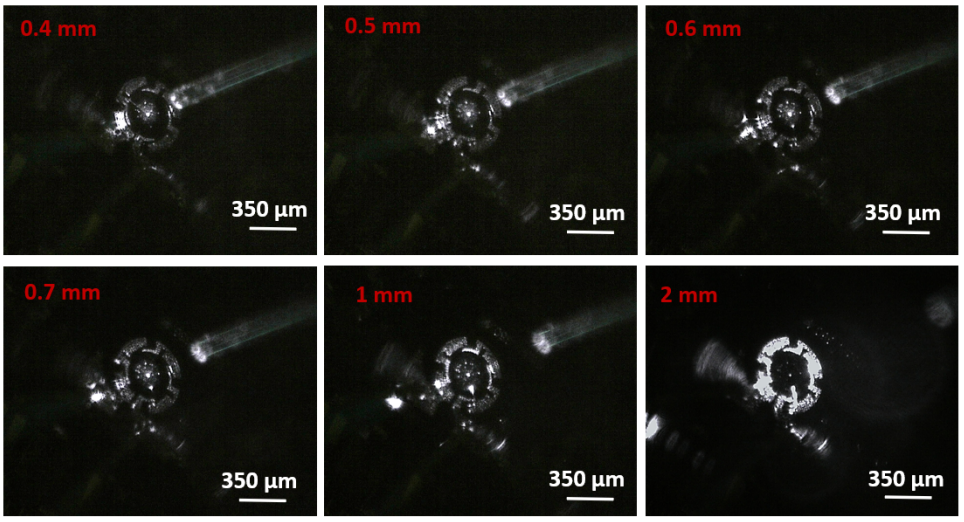


FIGURE 3.13: Illumination on the four segment GaAs PPC captured at a 45 degrees angle under quasi-Gaussian illumination for varying fiber-to-device distances.

0.5 mm, the beam expands further, and reflections begin to appear near the inner radii of the interconnect metal traces. At 0.6 mm, these reflections become evident, and illumination over the metallic regions becomes dominant. These observations provide insight into the variation of the I_{sc} with increasing fiber-to-device distance, as the changing beam distribution and metal reflections influence the optical coupling and photocurrent generation.

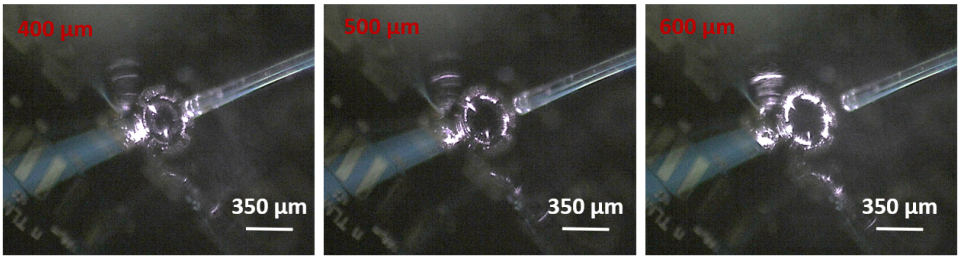


FIGURE 3.14: Annular beam illumination on the four segment GaAs PPC device captured at a 45 degrees angle for fiber to device distances of 0.4 mm, 0.5 mm, and 0.6 mm (images shown from left to right).

3.5 PV response of chip 2 under quasi-Gaussian and annular illumination

3.5.1 I_{sc} Dependence on Fiber-to-Device Distance

The I–V characteristics of Chip 2 were measured under quasi-Gaussian and annular illumination as a function of fiber-to-device distance. Figure 3.14 presents the extracted short-circuit current

I_{sc} for both illumination profiles at incident powers ranging from 10 mW to 60 mW.

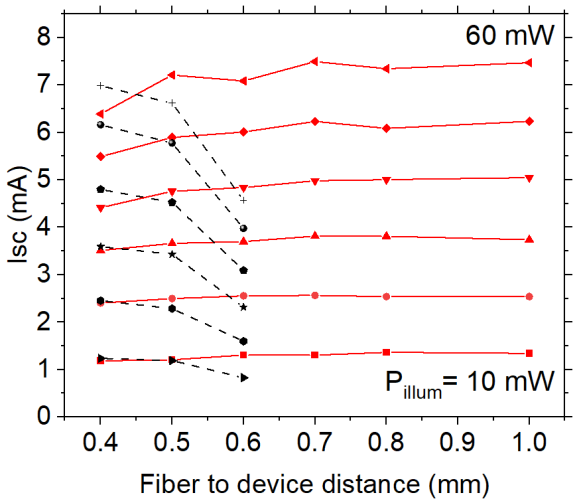


FIGURE 3.15: Variation of I_{sc} of Chip 2 as a function of fiber-to-device distance for incident optical powers ranging from 10 mW to 60 mW. The I_{sc} values under annular beam illumination are shown in black (dashed trace), while those under quasi-Gaussian illumination are shown in red (solid trace).

Under quasi-Gaussian illumination, I_{sc} remains relatively stable as the fiber-to-device distance increases from 0.4 mm to 0.8 mm, indicating robust optical coupling over this range. At an incident power of 10 mW, I_{sc} increases from 1.18 mA at 0.4 mm to 1.36 mA at 0.8 mm, corresponding to an enhancement of approximately 15%. This increase is consistent with improved spatial overlap between the expanding beam and the 350 µm active area. Beyond 0.8 mm, I_{sc} decreases by approximately 6% at 1.0 mm, coinciding with beam overspill beyond the device boundary and reduced active-area coverage observed in the beam images.

In contrast, annular illumination exhibits a stronger dependence on fiber-to-device distance. At 0.4 mm, the annular beam produces higher I_{sc} than the quasi-Gaussian case, with an enhancement of 2–12% across the investigated power range, consistent with the well-confined annular intensity ring observed in the corresponding beam profiles. As the distance increases to 0.5 mm, quasi-Gaussian illumination begins to yield 2–9% higher I_{sc}, marking the onset of radial expansion of the annular beam. At 0.6 mm, this expansion leads to pronounced overspill and reduced overlap with the active area, resulting in I_{sc} values that are 50–60% lower than those obtained under quasi-Gaussian illumination.

A direct comparison between annular illumination at 0.4 mm and quasi-Gaussian illumination at 0.8 mm shows comparable photocurrent levels at moderate incident power, with the quasi-Gaussian configuration exhibiting approximately 9% higher I_{sc} at 20 mW. This comparison highlights that while annular illumination can achieve efficient optical coupling at short

distances, quasi-Gaussian illumination provides more stable current collection as the fiber-to-device distance increases due to its broader and more tolerant beam coverage of the active area.

3.5.2 Open circuit and maximum operating condition of Chip 2

Figure 3.16 (a) shows the variation of V*oc* with incident optical power for quasi-Gaussian and annular illumination at different fiber-to-device distances. For both illumination profiles, V*oc* increases logarithmically with input optical power, consistent with standard photovoltaic behavior. At an incident power of 60 mW, annular illumination yields a maximum V_{oc} of 4.81 V at a fiber-to-device distance of 0.6 mm, which is approximately 1.7% higher than the value obtained under quasi-Gaussian illumination at a distance of 1 mm, the trends observed for Chip 2 closely follow those established using Chip 1.

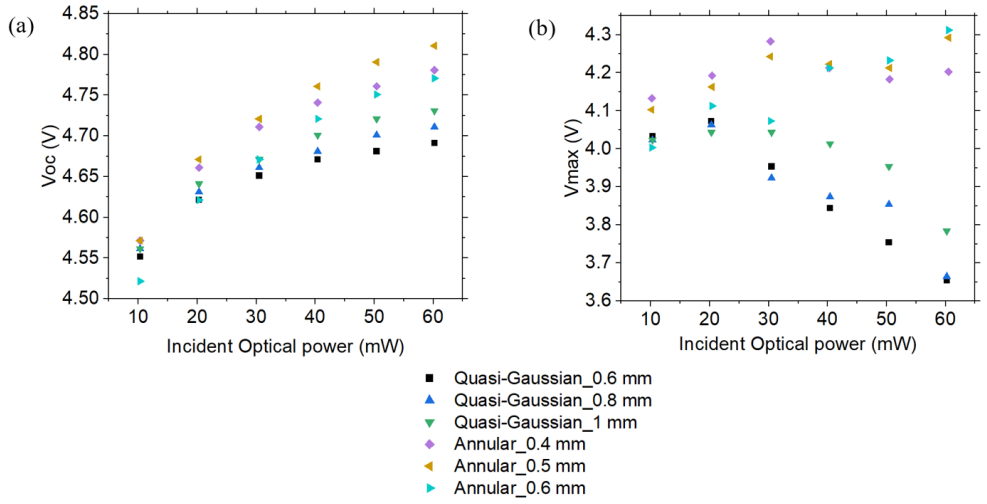


FIGURE 3.16: (a) V_{oc} and (b) V_{max} as functions of incident optical power for different fiber-to-device distances under quasi-Gaussian and annular illumination.

The device delivers a maximum voltage V_{max} of 4.13 V and 4.20 V at incident powers of 10 mW and 60 mW, respectively, under annular beam illumination with a fiber to device distance of 0.4 mm as shown in Figure 3.16 (b), whereas under quasi-Gaussian illumination at a 1 mm spacing, V_{max} decreases to 4.02 V at 10 mW and 3.78 V at 60 mW. The stronger reduction of V*max* at higher optical power under quasi-Gaussian illumination reflects increased resistive voltage losses during current flow through the device, consistent with the series-resistance effects identified for Chip 1. A fluctuation in the data observed near 40 mW under annular illumination data arises from variations in the source laser output and is excluded from comparative analysis.

In addition to the voltage characteristics, the maximum output power p_{max} delivered by the four-segment PPC under quasi-Gaussian and annular illumination was evaluated using the power–voltage characteristics shown in Fig. 3.16. At low incident optical power (10 mW), the extracted p_{max} values are comparable for both illumination profiles, yielding approximately 5.20 mW under quasi-Gaussian illumination (1 mm spacing) and 4.69 mW under annular illumination (0.4 mm spacing), indicating similar power delivery in the low-current regime. As the incident optical power increases, a clear divergence in performance is observed. At 60 mW input power, the device delivers a p_{max} of 27.02 mW under quasi-Gaussian illumination, while annular illumination yields a comparable value of 26.97 mW, demonstrating that the four-segment, 350 µm diameter PPC is capable of delivering nearly 27 mW of electrical power under surface-normal excitation.

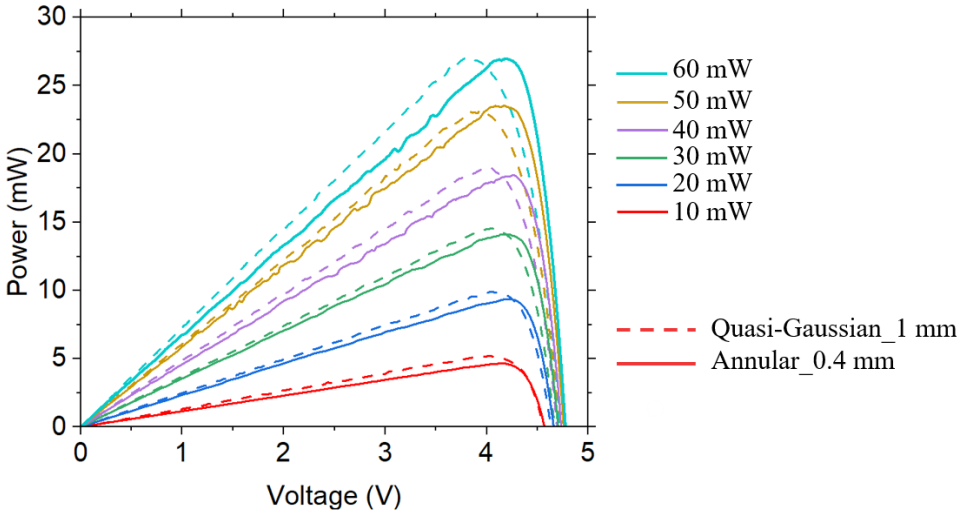


FIGURE 3.17: PV characteristics of the four-segment, 350 µm active diameter PPC, measured at the fiber-to-device separations corresponding to maximum power extraction for each illumination profile. Solid lines correspond to annular illumination at a distance of 0.4 mm, while dashed lines represent quasi-Gaussian illumination at a distance of 1 mm. Curve colour denotes the incident optical power, varied from 10 to 60 mW (bottom to top curve).

3.5.3 Distance and illumination dependent η and FF performance of Chip 2

Figure 3.18 compares η and FF of Chip 2 under quasi-Gaussian and annular illumination at the fiber-to-device distances corresponding to the highest performance for each illumination mode, specifically 1 mm for quasi-Gaussian illumination and 0.4 mm for annular illumination. Under quasi-Gaussian illumination, the device achieves an η of 50.5% at an incident optical power of 10 mW with a corresponding FF of 84.8%. As the incident power increases to 60 mW, η decreases to 45%, accompanied by a reduction in FF to 76.4%. These measurements are

obtained at a larger fiber-to-device separation than those explored for Chip 1 and therefore reflect the extended-distance study enabled by Chip 2 rather than an intrinsic improvement in device performance.

Under annular illumination, Chip 2 exhibits reproducible behavior, with η increasing gradually with incident power and reaching a maximum value of 47.4% with an FF of 81% at 50 mW. This trend closely follows that observed for Chip 1, confirming consistent power-conversion behavior under annular illumination across devices.

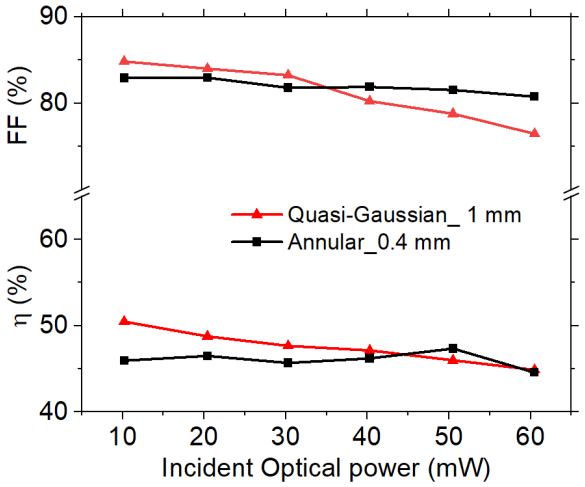


FIGURE 3.18: η and FF of chip 2 as a function of incident optical power under quasi-Gaussian and annular illumination for fiber to device distances of 1 mm and 0.4 mm, respectively. The results highlight that the device exhibits peak performance at these distances for each illumination condition.

Figure 3.19 illustrates the dependence of the η of Chip 2 on fiber-to-device distance under quasi-Gaussian illumination over the range 0.6–1.2 mm. While 0.6 mm corresponds to the theoretically estimated beam-matching condition, the experimental results show that the highest efficiencies are achieved at slightly larger separations. Increasing the distance from 0.6 mm to 0.8–1.0 mm leads to an improvement in η, whereas a further increase to 1.2 mm results in reduced performance. The maximum η of 50.6% is obtained at a fiber-to-device distance of 0.8 mm for an incident optical power of 10 mW, decreasing to 43.8% at 60 mW. The reduction in η at higher illumination levels is primarily associated with a decrease in the FF extracted from the measured I–V characteristics, which limits the achievable power output.

In comparison with Chip 1, where the maximum efficiency occurred at 20 mW for a fiber-to-device distance of 0.6 mm, Chip 2 exhibits optimal performance at lower incident power and at distances exceeding the nominal beam-matching condition. This shift reflects the evolution

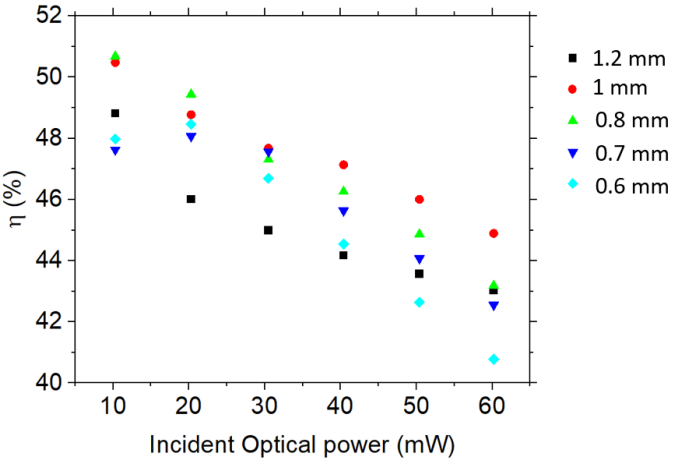


FIGURE 3.19: η plotted as a function of incident optical power for fiber to device distance of 0.6 mm to 1.2 mm under quasi-Gaussian illumination on Chip 2.

TABLE 3.1: Performance comparison of the four-segment, 350 µm active diameter PPC under quasi-Gaussian and annular illumination at their respective optimal fiber-device spacings.

Parameter	**Quasi-Gaussian (1 mm)**	**Annular (0.4 mm)**
Illumination profile	Center-peaked intensity distribution	Peripheral ring-shaped distribution
Fiber-device spacing	1.0 mm	0.4 mm
p_{max} = 10 mW	5.20 mW	4.69 mW
V_{max} = 10 mW	4.02 V	4.13 V
p_{max} = 60 mW	27.02 mW	26.97 mW
V_{max} = 60 mW	3.78 V	4.20 V
High-power voltage behavior	Response to rapid voltage reduction	Response to gradual voltage reduction
Illumination uniformity	Limited by intrinsic Gaussian beam profile	Improved by annular redistribution of optical power

of the multimode intensity distribution with propagation, leading to improved optical overlap at slightly larger fiber-to-device separations under quasi-Gaussian illumination.

3.6 Conclusion and Discussion

This chapter presented an experimental investigation of optical beam shaping for enhanced PV performance in laterally interconnected segmented PPC using a DCF illumination scheme. Through a comparative and parametric study involving two PPC chips, the influence of illumination profile, beam confinement within active region, and fiber to device distance on η and device reproducibility was systematically examined.

For Chip 1, annular illumination generated via angular coupling into the DCF improved voltage-related performance relative to quasi-Gaussian illumination. At an irradiance of 62.4 W/cm^2, annular excitation yielded an open-circuit voltage of approximately 4.74 V and an operating voltage exceeding 4 V, corresponding to improvements of about 1% and 9.6%, respectively. A peak η of 48% for chip 1 was achieved under annular illumination at 20.4 W/cm^2 for a fiber-to-device spacing of 0.4 mm, indicating effective redistribution of optical power across the segmented active area. At larger spacings, however, partial optical spillage reduced the collected photocurrent, highlighting the sensitivity of annular illumination to beam confinement within the PPC aperture.

Measurements on Chip 2 confirmed the robustness and reproducibility of these trends. Under quasi-Gaussian illumination, maximum η was observed at a fiber-to-device spacing of 1 mm, reaching about 50.4% at an irradiance 10.4 W/cm^2 and decreasing to 45% at 62.4 W/cm^2. In contrast, annular illumination achieved comparable power delivery while maintaining higher operating voltage at a reduced spacing of around 0.4 mm. These results demonstrate that beam shaping enables equivalent electrical performance at substantially reduced fiber-to-device separation, provided that optical confinement is carefully controlled. The key comparative results obtained at these optimized spacings are summarized in Table 3.1.

Annular illumination enables higher operating voltage in laterally segmented surface-normal PPCs. As the segment count is increased to support voltage scaling for delivery to remote circuits the associated growth in metal interconnects and isolation trenches enlarges the fraction of non-active regions within the device aperture. Under these conditions, Gaussian illumination experiences increased optical loss due to overlap with non-active regions, while annular illumination reduces this overlap and maintains effective power delivery. This behavior is relevant for segmented PPCs employed in power-over-fiber architectures requiring compact integration and elevated voltage operation, such as endoscopic microsystems. At higher incident powers, annular illumination exhibited a gradual reduction in conversion efficiency and delivered voltage, which can be attributed to non-uniform intensity distribution across the segmented PPC aperture. Achieving improved segment-to-segment illumination uniformity therefore remains an important design consideration. Future work will focus on optimizing annular beam generation through controlled excitation of higher-order modes in high-NA double-clad fibers, including refinement of launch conditions and tilt angles. Such improvements are expected to enhance optical confinement, improve illumination uniformity, and increase overall system efficiency,

further strengthening the viability of annular illumination as a scalable and robust approach for compact, high-performance surface-normal power delivery systems.

Chapter 4

Remote signalling using transfer printed electroabsorption modulator on a reflector

4.1 Introduction

In a power-over-fiber system for minimally invasive surgical endoscopes with outer diameters ranging from 1 mm to 3 mm, the ability to remotely deliver sufficient optical power while simultaneously supporting high-speed data transmission depends on both the efficiency of the photovoltaic power converter and the performance of the optical modulator responsible for encoding the return data signal. The previous chapter demonstrated that surface-normal illumination onto a multi-segment PV converter provides an effective and compact approach for harvesting optical power at the distal end of the endoscope. With the power-delivery method established and its electrical output characteristics defined, the next requirement is the selection of a modulator that can operate within the constrained voltage and power levels available from the photovoltaic device.

Short-reach optical links are commonly implemented using directly modulated semiconductor lasers, including edge-emitting lasers and VCSELs. This chapter focuses on SNEAMs based on the quantum-confined Stark effect (QCSE), which provide a compact device geometry together with high extinction-ratio amplitude modulation, low drive-voltage operation, and polarization-independent behavior [73]. These characteristics align directly with the spatial and electrical

specifications of the targeted power-over-fiber endoscopic platform, where all components must be accommodated within an outer diameter below 3 mm. In addition, the surface-normal active aperture of SNEAMs is compatible with fiber delivered optical carriers from SMF and DCF, enabling low-loss fiber–device coupling. Experimental demonstrations in the literature [74] show that SNEAM arrays comprising devices with approximately 20 µm apertures have been packaged and passively aligned within optical systems. The SNEAM device design and footprint evaluated in this chapter are used to determine the achievable device performance for subsequent co-integration with a surface-normal photovoltaic converter, providing the basis for its integration within a minimally invasive power-over-fiber imaging tool.

This chapter details the design of SNEAM device and the transfer printing technique for assembling the prefabricated SNEAM on a pattern target substrate. This assembly enables the device to function as a reflective SNEAM. The fabricated SNEAM features an active aperture of 30 µm and a coupon footprint of 68 µm × 77 µm with integrated electrical contacts on an indium phosphide (InP) platform. An asymmetric Fabry–Pérot cavity is implemented using the air–semiconductor interface as the top reflector and a bottom reflector composed of a silicon nitride (SiN) layer and a high-reflectivity metallization stack on a silicon substrate. The operating principle, governed by the QCSE, is examined through photoresponse measurements. The cavity is designed to exhibit resonance at 1560 nm detuned from the intrinsic PIN exciton absorption by depositing a 390 nm SiN layer above the bottom reflector.
The transfer printed SNEAM exhibits a DC extinction ratio of 6 dB between bias voltages of -1V and -7 V. We measure the bandwidth of the device to be 9 GHz at 1560 nm for bias voltage of -5 V. A eye diagram measurement were shown for a data modualtion of 1 Gbps on the device using Non-Return-to-Zero On-Off Keying (NRZ-OOK) with driving voltage of 6 V.

4.2 Principles of SNEAM Operation and State of the Art

The shift in the absorption spectrum under an applied electric field in a quantum well (QW) structure arises from the quantum-confined exciton, a bound electron hole pair confined within the low-bandgap well and restricted by the surrounding higher bandgap barriers [75]. Figure 4.1 (a) illustrates this QCSE using a single well example, whereas the actual device employs multiple wells and barrier. With no applied field, the electron and hole wavefunctions are centered within the well, defining the excitonic transition energy E_1. When a reverse bias is applied, the electric field tilts the potential and displaces the carrier wavefunctions toward opposite

sides of the well, lowering the excitonic transition energy to E_2 which appears as a redshift in the absorption spectrum. At sufficiently high fields, the field-induced separation becomes large enough that the exciton can no longer remain bound, leading to the disappearance of the excitonic. The corresponding change in the absorption spectrum is illustrated schematically in Figure 4.1 (b). In the unbiased case, a distinct excitonic peak appears near the band edge, characteristic of a well confined electron–hole pair. Increasing the reverse bias shifts this peak to longer wavelength and reduces its amplitude due to field-induced wavefunction displacement. For electro-absorption modulation, an operating wavelength λ_{op} is selected at the point where the absorption difference between spectra obtained under different reverse-bias conditions reaches its maximum, providing the highest extinction ratio. This bias-dependent change in absorption amplitude enables modulation of the transmitted optical signal by switching the applied voltage between its on and off states.

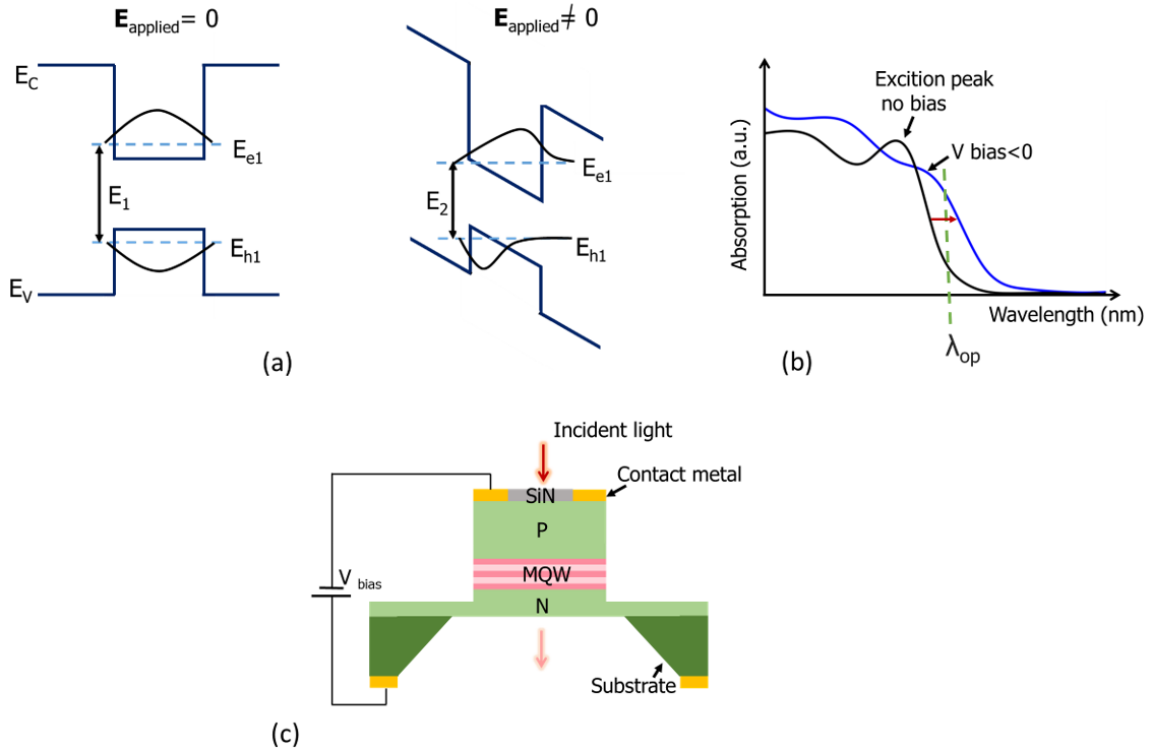


FIGURE 4.1: (a) Band diagrams illustrating the electron and hole wavefunction in a single QW, under no bias and reverse condition. (b) Schematic absorption spectra showing the QCSE-induced redshift and reduction of the excitonic peak under reverse bias, with λ_{op} indicating the wavelength of maximum modulation. (c) Schematic of surface normal EAM under transmission design.

Figure 4.1 (c) illustrates the early implementation of a SNEAM [76] [77], in which light propagates perpendicular to the MQW layers. In this transmission-based configuration, incident light enters through the top surface, passes through the SiN anti-reflection coating and the p-doped semiconductor layer, and then reaches the intrinsic region containing the MQWs that

govern the modulation process. As the incident light passes through the MQW region, the absorption changes with the applied reverse bias, and the transmitted light exits through the n-doped semiconductor and the backside-etched substrate for collection. This surface normal transmission design enabled the first direct measurements of QCSE by monitoring the transmitted intensity through the device. However, the geometry inherently limits the interaction length between the incident light and the MQW region, which in turn restricts the achievable extinction ratio.

Addressing this limitation required increasing the interaction length within the MQW region, and early devices therefore employed MQW sections nearly one 1 µm thick to produce a measurable change in excitonic absorption at a fixed wavelength. This increased thickness, however, distributed the applied voltage over a larger distance, reducing the electric field for a given bias and therefore requiring higher reverse-bias operation while also introducing additional insertion loss. Later studies demonstrated that a more effective way to enhance the interaction between the incident light and the MQW region is to form a Fabry–Pérot (FP) cavity by placing mirrors above and below the PIN stack that includes MQWs [78] [79]. A reflective interface beneath the MQW region increases the effective optical path without modifying the physical thickness of the intrinsic layer, allowing the optical field to traverse the wells multiple times. This resonance based configuration strengthens the influence of QCSE induced absorption changes, enabling higher extinction ratios at reduced drive voltage.

4.2.1 Asymmetric FP Reflection operation in SNEAM

In the SNEAM, the asymmetric FP design is realized by using a lower reflectivity top mirror relative to the bottom mirror, which enhances the resonant response and enables a high extinction ratio. [79] [80]. Figure 4.2 illustrates this asymmetric configuration. In the reflection-mode operation of SNEAM, the incident light encounters the top-interface reflection and also propagates through the MQW region to the bottom mirror, where it is reflected and passes back through the MQW with a phase opposite to that of the top reflection. The absorption change in the MQW region induced by the QCSE adjusts the attenuation of this round-trip light, thereby modifying the effective bottom reflection response so that the interfering reflected amplitudes can be brought to the condition required for cancellation.

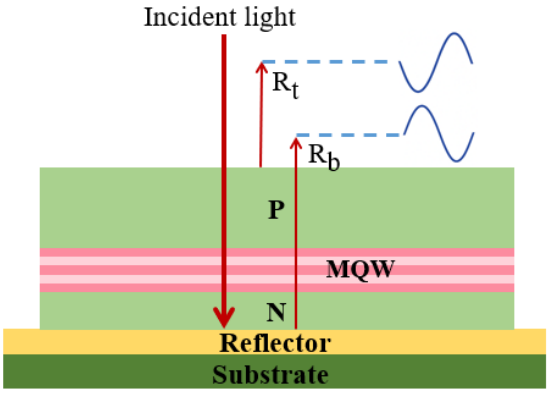


FIGURE 4.2: Schematic illustration of light reflection in the asymmetric Fabry–Perot operation of SNEAM. The top reflection R_t exhibits a 180-degree phase shift, and the bottom reflection R_b, after passing through the cavity, ideally returns with an opposite phase and an amplitude comparable to R_b, enabling destructive interference in the reflected signal.

At resonance, the total reflected amplitude at the top surface is expressed as in [79]

$$r_{\text{tot}} = -r_t + r_b e^{-\alpha L}, \tag{4.1}$$

where r_t and r_b are the amplitude reflection coefficients of the top and bottom reflector, respectively, and α and L are the absorption coefficient and cavity length of the MQW region. The QCSE increases α under reverse bias such that the attenuated bottom-mirror reflection satisfies the balance condition in Equation 4.2, where its amplitude and phase match those of the top reflection; under this condition, the total reflected amplitude reduces to zero, as shown in Equation 4.3.

$$r_b e^{-\alpha L} = r_t, \tag{4.2}$$

$$r_{\text{tot}} = -r_t + r_t = 0, \tag{4.3}$$

In terms of power reflectivities $R_t = |r_t|^2$ and $R_b = |r_b|^2$ this cancellation condition becomes

$$R_b e^{-2\alpha L} = R_t, \tag{4.4}$$

which can only be satisfied when $R_b > R_t$ so that the bottom reflection can be reduced to the required level by absorption in the cavity. This unique ability of the asymmetric FP configuration to reach the zero–reflectivity condition with modest absorption change allows SNEAM devices to achieve very high extinction ratios with short cavity lengths and low operating voltages, in contrast to symmetric FP structures, which cannot realize this cancellation at low bias.

The top reflectivity was optimized through epitaxial growth of distributed Bragg reflection layers [81] [82], deposition of dielectric layers [73] and using the air semiconductor interface [79] [83]. In order to achieve a SNEAM device with high performance, an optimization of the PIN structure and top reflectivity are crucial for positioning the FP resonance at a wavelength encountering high change in absorption for an applied reverse bias. Recent work used an asymmetric design approach as an effective way to reduce the drive voltage from 4 V to 1.5 V by reducing the MQW number and by further optimization of the top reflector which in resulted in an extinction of 10 dB [59]. In the literature, integration of asymmetric SNEAMs from source to any target wafer were demonstrated using either flip-chip bonding or wafer bonding. A 1-D array of C-band SNEAM devices was demonstrated using flip-chip bonding of an active region containing InAlGaAs QWs followed by substrate removal [73], [84]. In [85] a Ge-Si-based asymmetric FP EAM, grown on a silicon substrate and integrated onto a handling wafer, was realized via anodic bonding and selective silicon etching. While these approaches enable device integration, they involve complex substrate release and intricate fabrication steps to incorporate both top and bottom reflectors in the SNEAM structure. As a more flexible and scalable alternative, we employ microtransfer printing to assemble the SNEAM device with InAlGaAs QWs. This approach enables heterogeneous integration with remote powering device, allowing efficient pick-and-place transfer of disparate photonic components onto target wafers [86], [87].

4.3 Reflective SNEAM device design

The formation of the reflective electro-absorption modulator device involves two separate design and process steps. The first step is the design and fabrication of the SNEAM, and the second involves designing the cavity on the target wafer and transfer-printing the released SNEAM device onto the reflector target, enabling it to function as a reflective EAM device. On the source wafer, the PIN structure with MQW layers is grown epitaxially, followed by the fabrication of the SNEAM device structure using a specifically designed mask. The SNEAM device is designed to operate based on an asymmetric FP cavity resonance. The prefabricated SNEAM device is transfer-printed onto a dielectric layer positioned above the reflector on the target wafer. These steps are discussed in detail in the following sections.

4.3.1 SNEAM device design

A surface normal configuration of the EAM is realized using a circular mesa design with active diameters of 10 µm, 20 µm, and 30 µm. These diameters were chosen to enable light coupling through a single-mode fiber. On the source wafer, the EAM with a PIN structure consists of a 2 µm, thick p-layer, 10 AlInGaAs-based quantum wells, an intrinsic region with a total thickness of 395 nm, and a 200 nm thin n-layer. An InGaAs and InAlAs dual sacrificial layer with thicknesses of 100 nm and 400 nm, respectively, is incorporated to enable undercutting of the coupons for transfer printing. The thickness of the intrinsic layer and the number of quantum wells are critical parameters that determine the bias voltage required to observe a strong QCSE. The MQWs in the PIN structure were designed for achieving an exciton peak near 1500 nm. When the SNEAM is placed on a reflective substrate, the FP resonance enhances the interaction between the incident light and the MQW absorbing layer, enabling a larger QCSE-induced redshift at reduced operating voltage. Based on the intrinsic-region thickness used in this device, applied reverse-bias voltages of 5 V and 7 V correspond to electric fields of 127 kV/cm and 177 kV/cm, respectively. The MQW epitaxial structure used in this work is identical to that reported in [88], where a QCSE-induced excitonic redshift of several nanometers was demonstrated under surface-normal incidence for reverse-bias voltages up to 8 V. In that work, absorption modulation of the same MQW structure was characterized in an edge-coupled configuration, confirming that electric-field magnitudes in this range are sufficient to induce significant electroabsorption in InAlGaAs/InP MQWs.

The EAM device was grown on an InP substrate, incorporating a release layer composed of InGaAs and AlInGaAs beneath the PIN layers. Further details of the epitaxial stack are provided in [88]. The overall coupon dimension of the PIN circular mesa structure with active diameters of 10 µm, 20 µm and 30 µm are 63 µm × 77 µm, 68 µm × 77 µm and 80 µm × 87 µm designed in considering the fabrication tolerance associated with each process step. The device dimension should also be compatible with the polydimethylsiloxane (PDMS) stamp used for transfer-printing the coupon from the source wafer to the target wafer.

4.3.2 Asymmetric FP Cavity Design

The asymmetric FP cavity is formed within the PIN structure, comprising two reflectors separated by a MQW active region illustrated in Figure 4.3 (a). The cavity includes a front partial reflector R_t and a back-end high reflector. The incident light P_{in} first interfaces with the air

and the p-InP layer at the front of the device, where partial reflection occurs. The remaining light propagates through the MQW active region and is reflected by the Au back reflector, forming an optical resonance within the cavity. The resonant wavelength of the FP cavity is designed to coincide with the wavelength of maximum absorption difference in the MQW under applied reverse bias.

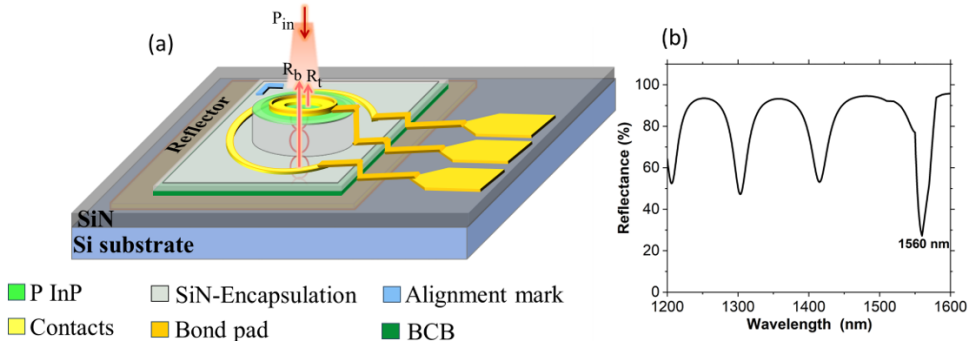


FIGURE 4.3: (a) Schematic of asymmetric FP resonance in the SNEAM device, (b) The simulated cavity response plotted for comparing reflection intensity with increase in reverse bias.

This design choice follows from the QCSE behaviour discussed in Section 4.2. Under reverse bias, the field-dependent absorption modifies the effective bottom-mirror reflection R_b, enabling the device to switch between high and low reflectivity states. To optimize the operating resonant wavelength, a dielectric SiN layer is deposited before the back-end reflector to adjust the cavity length. The thickness of the SiN layer (refractive index n = 1.99 [89]) is designed to be a half-wavelength thickness, supporting a resonant wavelength of 1560 nm, which corresponds to the maximum extinction ratio of the signal. A thin benzocyclobutene (BCB) layer is used primarily as an adhesive to bond the PIN structure to the SiN–Au reflector; however, because BCB also forms part of the optical cavity, its presence influences the effective cavity length and therefore affects the FP resonance. Thin-film simulations are used to evaluate how the SiN and BCB layer thicknesses affect the resonance behaviour of the cavity.

Figure 4.3 (b) shows the thin-film simulation implemented using Essential Macleod, and the intrinsic-layer parameters employed are listed in Appendix Table A.7.1 and A.7.2. The simulation results in Figure 4.4 are plotted for wavelengths below 1560 nm to reveal the FP cavity modes beyond the excitonic absorption region, allowing direct comparison with DC-characterization measurements. The resonant mode near 1560 nm is achieved by optimizing the SiN and BCB layer thicknesses to 390 nm and 90 nm, respectively. The effect of varying these thicknesses in the multilayer PIN–BCB–SiN–Au structure is illustrated in Fig. 4.4. The simulations are primarily used to identify and compare the depth of the reflectance minimum

near 1560 nm, which corresponds to the strength of the FP cavity resonance controlled through the SiN and BCB layer thicknesses.

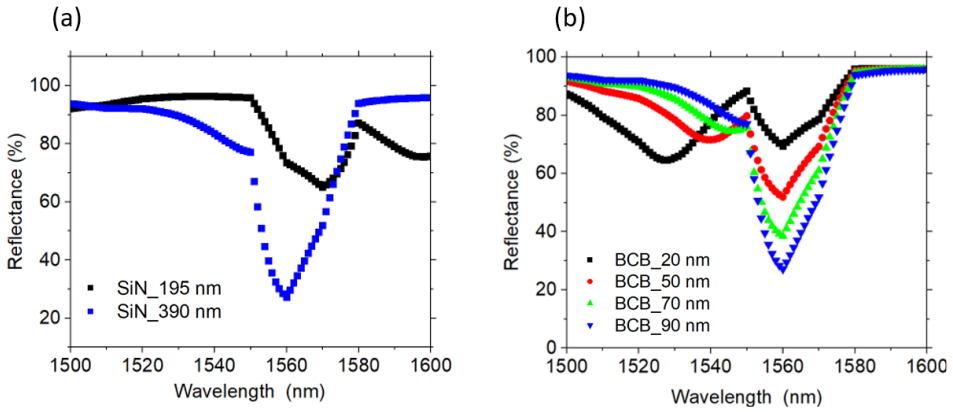


FIGURE 4.4: Thin-film simulation results of the multilayer PIN–BCB–SiN–Au structure obtained using Essential Macleod. (a) Reflectance spectra showing the variation in reflectance minimum for quarter-wavelength (195 nm) and half-wavelength (390 nm) SiN thicknesses at a fixed BCB thickness of 90 nm, highlighting the resonance near 1560 nm. (b) Spectral reflectance as a function of wavelength for different BCB thicknesses with the SiN thickness fixed at 390 nm.

To support resonance at the target wavelength, the SiN thickness was considered for quarter-wavelength (195 nm) and half-wavelength (390 nm) conditions while keeping the BCB thickness fixed at 90 nm. As shown in Figure 4.4 (a), a SiN thickness of 390 nm produces a deeper reflectance minimum than 195 nm, indicating stronger destructive interference between the reflected waves and more effective phase matching at 1560 nm. This comparison demonstrates that the resonance is more weakly supported for the quarter-wavelength SiN configuration.

The influence of the BCB layer thickness was examined by fixing the SiN thickness at 390 nm, with the results shown in Figure 4.4 (b). Introducing a 90 nm BCB layer reduces the reflectance at resonance from 69.4% to 27.2%, corresponding to an absolute reflectance reduction of approximately 42.2 percentage points compared to the case without a BCB layer between the PIN stack and the SiN–Au reflector. This reduction confirms the role of the BCB layer in strengthening the cavity resonance by modifying the effective optical path length.

In this design, both the SiN and BCB layers form part of the optical cavity and therefore contribute to the effective refractive index experienced by the optical mode. Because SiN has a higher refractive index than BCB and can be deposited without a hard-curing process, it is used as the underlying layer beneath the PIN structure to provide finer control over the resonance condition. The abrupt spectral features observed in the simulated reflectance curves arise from the limited wavelength resolution of the intrinsic material optical data used in the Macleod

simulations. Increasing the density of wavelength-dependent material data points would result in smoother spectral transitions while preserving the observed reflectance minima and their dependence on SiN and BCB thickness.

4.4 Fabrication of Asymmetric FP SNEAM Devices

The fabrication of the SNEAM is based on a process flow and corresponding mask that was designed in this work, involving a source wafer and a target wafer. Details of the epitaxial PIN material stack are provided in Appendix A.8.1. On the source wafer, PIN structures with device contacts are fabricated and finished with tether and releasing coupon steps. On the target wafer, the reflective mirror stack is patterned and prepared to receive the transferred devices. Following transfer printing, the fabrication process is completed with bond-pad metallization for electrical characterization. The corresponding mask layouts used for the source and target wafer fabrication are provided in Appendix Figure B.3.1 and B.4.1.

4.4.1 Source fabrication

The EAM devices with active diameters of 10 µm, 20 µm and 30 µm, were fabricated on the source wafer using a 7-layer mask process. The fabrication steps includes P-metal lithography and metallization, mesa formation and mesa encapsulation, N-metal lithography and metallization, coupon definition and coupon encapsulation, contact opening, and photoresist tether definition. The layout design of the coupon with tethers is presented in Appendix Figure B.1.1, and B.2.1. Following these steps, the undercut process is performed by selectively removing the release layer using a $FeCl_3$ solution, allowing the coupons to be released and prepared for pick-and-place integration. A schematic representation of the source wafer process flow is illustrated in Figure 4.5.

4.4.2 Target fabrication

The silicon target wafer fabrication begins with the design of a photolithography mask that incorporates the bottom reflector geometry, alignment marks required for the transfer-printing process, and bond-pad layouts. Using this mask, lithographic patterning is carried out to define

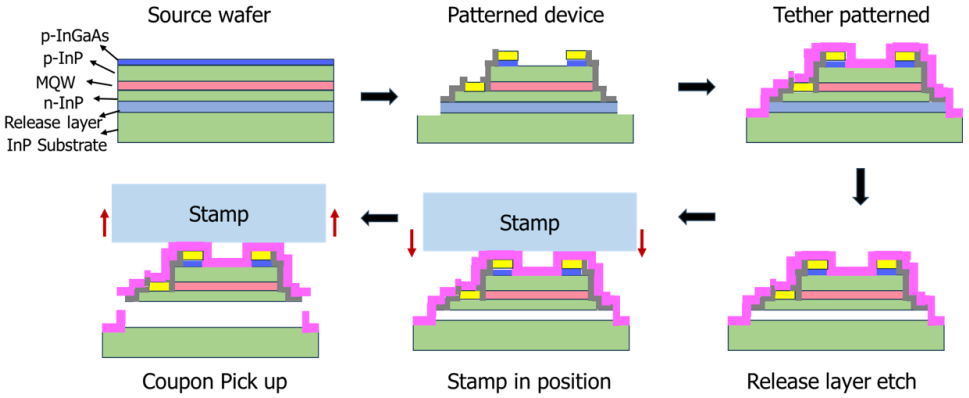


FIGURE 4.5: Overview of the fabrication process flow for the source wafer.

the Au bottom reflector and bond pads on the silicon substrate. These patterned features establish both the optical cavity foundation and the electrical access required for subsequent device integration. The bottom reflector geometry is defined on the silicon wafer using lithography, followed by the deposition and lift-off of a 200 nm thick Au layer, resulting in Au being present only in the designed reflector regions. Following the formation of the Au bottom reflector, a 390 nm thick SiN layer, corresponding to a $\lambda/2$ optical thickness, is deposited uniformly across the entire wafer using plasma-enhanced chemical vapor deposition. The SiN layer uniformly covers the patterned Au reflector and remains present beneath the bond-pad regions, with its thickness optimized to achieve a resonant cavity wavelength of 1561 nm. Prior to BCB deposition, the target wafer undergoes O_2 plasma treatment at 66% power (200 W) for 10 minutes to enhance adhesion. Subsequently, a 90 nm thin BCB layer is spin-coated onto the SiN layer of the target wafer and cured at 90°C for 3 minutes.

4.4.3 Micro transfer printing

The prepared target wafer and released SNEAM coupon on the source wafer are positioned in the transfer print instrument. The PDMS stamp with dimension of 80 µm × 80 µm used to pick the released coupon with encapsulation of 63 µm × 77 µm, 68 µm × 77 µm and 80 µm × 87 µm. The picked coupons were positioned at the target locations and printed after fine alignment using L-shaped alignment markers defined on both the coupons and the target wafer. After successful coupon transfer with misalignment of <1 µm, the target wafer is placed on a hot plate at 120°C for 3 minutes to enhance adhesion between the printed coupon and the BCB-coated target before removing the tether. The tether resist is then removed using a surface patterning tool, where O_2 cleaning is performed for 6 minutes.

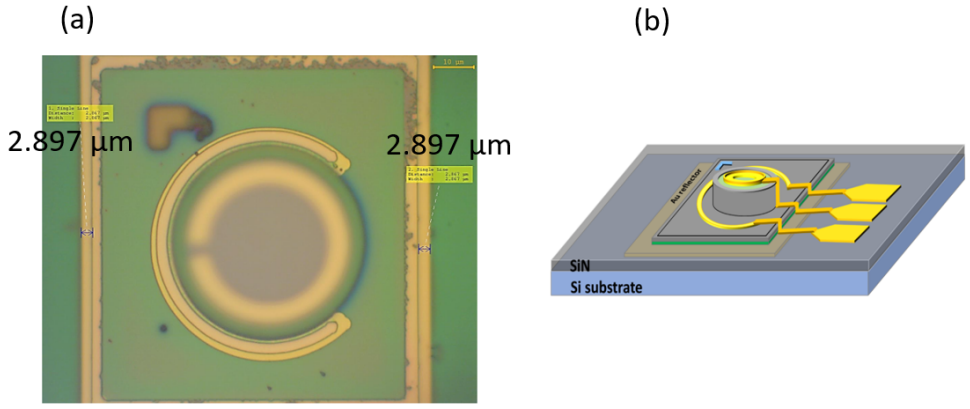


FIGURE 4.6: (a) Microscope image of the transferred coupon on the target wafer prior to GSG pad metallization, showing the alignment accuracy. (b) Schematic illustration of the printed device on the target wafer following completion of the GSG pad metallization.

To further improve the adhesion between coupon and the spin-coated BCB reflector target, the transfer-printed targets were placed in silylation oven. Figure 4.6 shows a schematic of the final post-processing step, in which ground-signal-ground (GSG) bond pads are defined for testing by lithography and angled metal evaporation using a Ti/Pt/Ag/Au metal stack with thicknesses of 60 nm/40 nm/800 nm/200 nm, respectively.

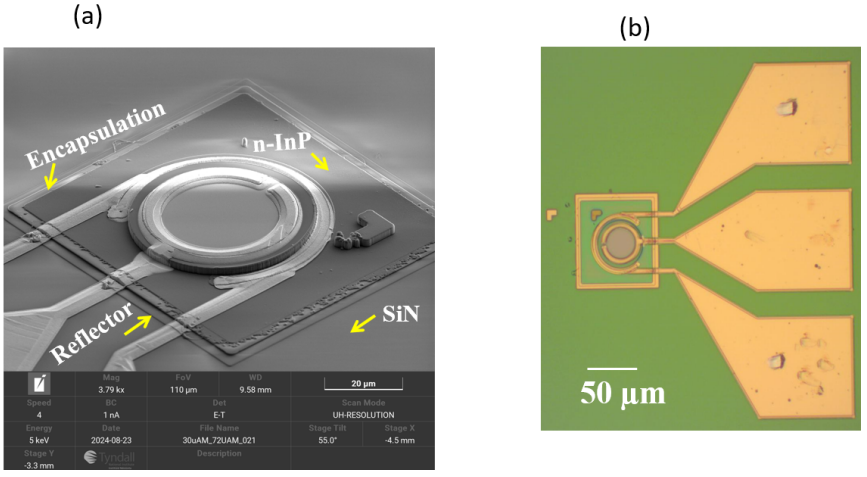


FIGURE 4.7: EAM device with an active diameter of 30 µm printed onto the target wafer: (a) Scanning electron microscope (SEM) image of the device following bondpad metallization on the transferred coupon. (b) Microscope image of the completed device showing the GSG pad configuration.

The SEM image in Figure 4.7 (a) was captured to demonstrate the successful transfer printing of the device onto a back reflector, positioned beneath the SiN and BCB layers. The GSG track is defined on the P and N metal contacts on the device, which has an active diameter of 30 µm. Figure 4.7 (b) presents a microscope image of the completed device, highlighting the GSG pad structure. Each pad has dimensions of 100 µm × 100 µm on the target wafer, with

pad pitch of 125 µm designed to match the GSG probe used for device testing. The pads were positioned 150 µm from the center of the mesa to prevent the 125 µm diameter fiber cladding from interfering with device probing. The layout of the device on the target wafer is shown in Appendix Figure B.5.1.

4.5 Result and discussion

4.5.1 Photoabsorption response

The photoresponse of the 30 µm active diameter device was characterized by illuminating it with a broadband wavelength source. Figure 4.8 (a) demonstrates the QCSE effect, illustrating the voltage-induced wavelength shift. The exciton peak is prominently observed near 1500 nm under a low bias at 0 V. As the reverse bias increases, the exciton peak exhibits a slight reduction in absorption amplitude. However, near 1560 nm, the absorption peak increases at -7 V and -8 V, which results from the cavity design. At this wavelength, a significant difference in absorption amplitude is observed between voltage levels of -8 V and -1 V, indicating high extinction ratio amplitude modulation. Further increasing the bias beyond -8 V depletes the exciton, leading to a decrease in amplitude. Figure 4.8 (b) presents the exciton wavelength shift as a function of reverse bias voltage, demonstrating a clear redshift with increasing bias. The magnitude of the shift reflects the nonlinear field dependence characteristic of the QCSE, where the applied electric field tilts the potential profile and spatially separates the electron and hole wavefunctions, thereby reducing the transition energy.

The cavity resonant wavelength is aligned with a spectral region in which MQW absorption exhibits strong dependence on the applied reverse bias due to the QCSE. As light undergoes multiple round trips within the cavity, the effective interaction length within the MQWs is increased, thereby amplifying the bias-induced change in absorption at the resonant wavelength. This behavior is absent in the QCSE effect observed in the same EAM structure without the cavity design [88]. The results demonstrate that this long-cavity device supports operation at multiple resonant wavelengths, including 1316 nm, where photoabsorption is high, making it suitable for receiver applications. The free spectral range was determined from the peak-to-peak separation of adjacent cavity resonances and evaluated in the frequency domain, resulting an approximately constant mode spacing of 18 THz. The dual operational capability under optimal biasing conditions allows the device to function as both a receiver channel and a signal

modulator for remote applications. However, this work focuses on testing signal modulation due to time constraints.

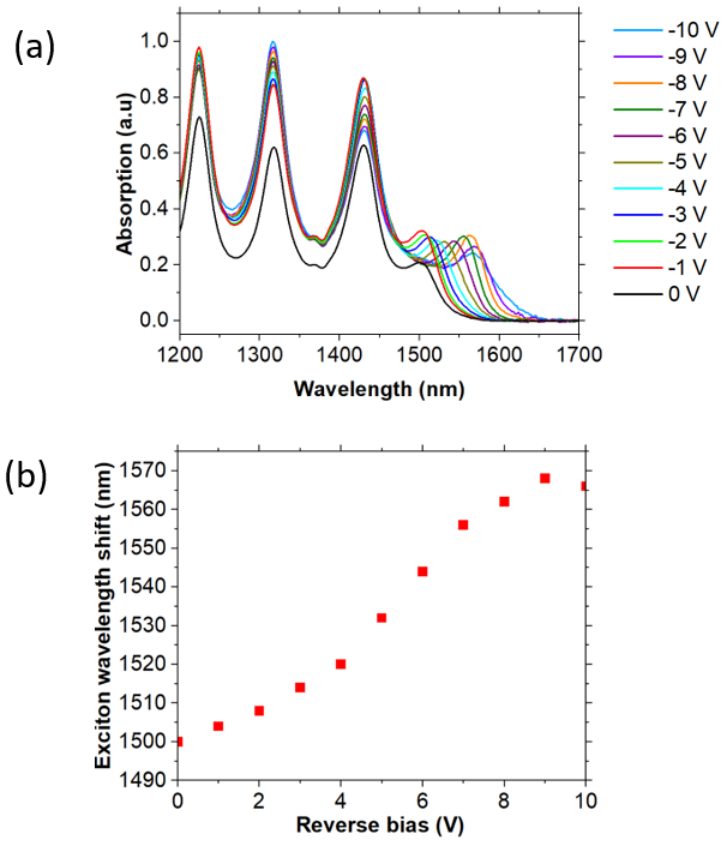


FIGURE 4.8: (a) The QCSE effect of SNEAM with presence of asymmetric FP condition. Voltage induced exciton shift tested for 30 µm diameter device and (b) Exciton wavelength shift versus reverse bias applied to the device.

4.5.2 Reflection spectrum

The reflected light from the device was measured using a flat-cleaved SM fiber with core diameter of 9 µm, positioned perpendicular to the device surface. The fiber was carefully aligned to avoid cavity formation between the fiber tip and the device surface, ensuring that the reflected signal corresponded only to the FP cavity of the device. All the measurements were performed on the device with 30 µm active diameter. The experimental setup consists of a broadband amplified spontaneous emission (ASE) output from an Erbium-Doped Fiber Amplifier (EDFA), which is incident on the SNEAM device through an optical circulator. The reflected light from the device was analyzed using an optical spectrum analyzer (OSA) via the circulator, as illustrated in Figure 4.9 (a). The corresponding bench-top arrangement used for these measurements is shown in Figure 4.9 (b). In this setup, the chip containing the device

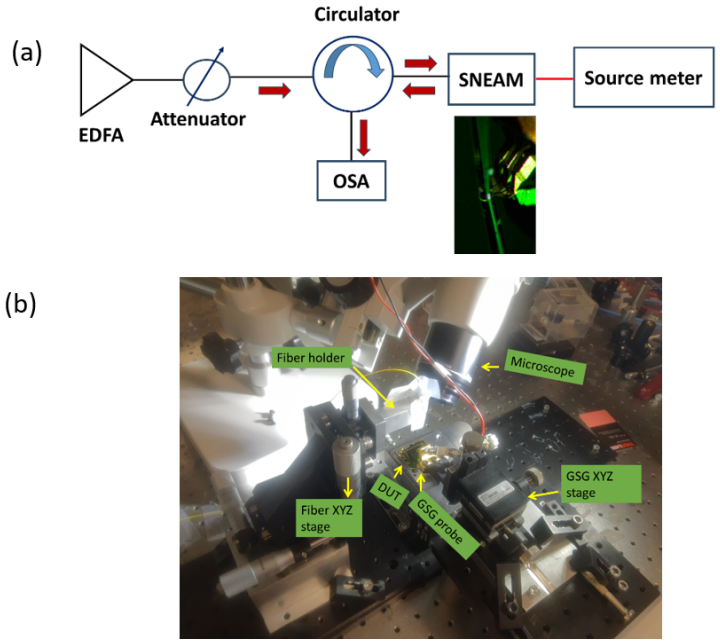


FIGURE 4.9: (a) Schematic of reflection experimental setup for the SNEAM device. The inset shows the fibre aligned device during testing. (b) Experimental setup showing a single-mode fiber aligned surface normal to the top surface of the device under test (DUT), which is probed using a GSG probe.

under test (DUT) and microscope is placed at 45 degrees to enable precise visual alignment. The optical fiber, used both to deliver light to the device and to collect the reflected signal, is secured in a fiber holder and positioned perpendicular to the device surface using a precision XYZ translation stage. The GSG electrical probe is mounted on a separate XYZ stage to establish stable electrical contact with the chip.

Figure 4.10 highlights the circular mesa structure surrounded by the P-metal contact, with a 30 µm, providing a detailed view of the top surface of the device. The reflected light measurement is highly sensitive to the fiber angle and position because the non-planarized top surface of the device makes the optical response strongly dependent on the fiber to top surface spacing and alignment. Despite the use of a lens-ended fiber, variations in the spacing between the fiber tip and the device surface can introduce unintended cavity effects that perturb the measured response. A consistent cavity response is obtained only when the fibre is positioned in contact with the device surface and precisely aligned using a precision XYZ translation stage. Under these conditions, the 10 µm and 20 µm aperture devices exhibit greater sensitivity to coupling variations than the 30 µm device, as the alignment of fiber core to smaller apertures results a low tolerance. As a result, even minor deviations in alignment produce noticeable changes in the coupled optical power and the observed cavity response.



FIGURE 4.10: SEM image of the 30 µm SNEAM device. The active area is surrounded by a circular P-metal ring, which defines the optical access aperture relevant to fibre alignment during measurement.

The reflection spectra were obtained by normalizing the measured reflected optical power to the EDFA output spectrum, as shown in Figure 4.11 (a). By comparing the voltage switching between a reverse bias of -1 V to -7 V, the reflection at 1561 nm decreases, achieving an extinction ratio of 8 dB for an input power of 0 dBm launched through the single-mode fiber. The reduction in FP resonance for biases beyond -7 V is attributed to the response of the MQW structure, where increased electric field induced absorption modifies the cavity response.

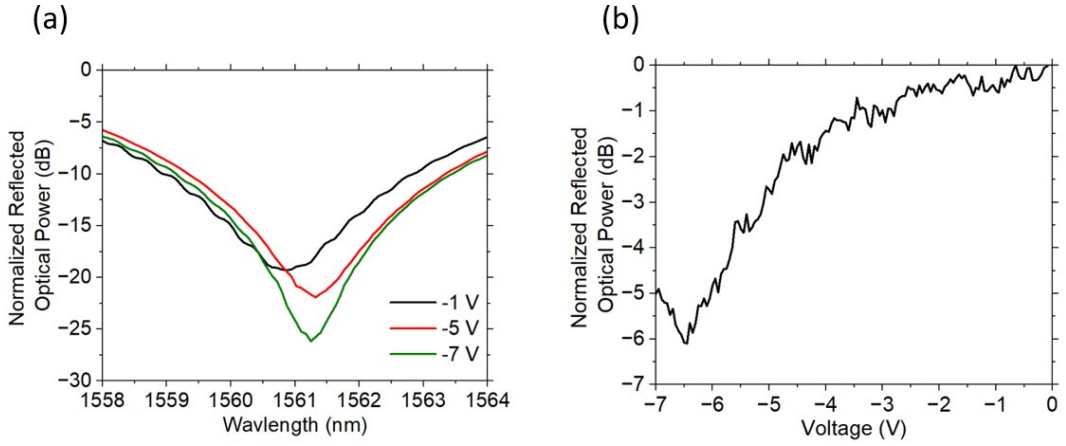


FIGURE 4.11: ((a) Normalized reflection spectra of the 30 µm active diameter device SNEAM device measured at reverse biases of -1 V, -5 V and -7 V, (b) Transfer characteristic showing the normalized reflected power as a function of applied reverse bias for the same device.

The transfer characteristics of the SNEAM were measured by analyzing the reflected optical power as a function of applied reverse bias. The measurement was performed by coupling incident light from a tunable laser source into the device at 1561.75 nm (0 dBm), near the FP resonance, and sweeping the bias voltage from -1 V to -7 V, while monitoring the reflected optical power using a power meter. The resulting transfer curve, shown in Figure 4.11 (b), was

normalized to its maximum reflected value and illustrates the voltage-dependent absorption behavior due to the QCSE. The device exhibits a 6 dB DC extinction ratio when switching between -2 V and -7 V. The transfer curve shows asymmetry beyond -6 V, which is consistent with bias-induced changes in the optical response, including modifications to both absorption and refractive index that alter the cavity coupling conditions. In particular, QCSE-induced refractive index changes shift the FP resonance relative to the fixed probe wavelength, causing the device to move off resonance at higher reverse bias and resulting in an increase in the measured reflected power. The insertion loss, which includes bidirectional coupling losses from the SNEAM and material absorption, was extracted from the higher-reflection state at -1 V, and was 19 dB near the FP resonance.

4.5.3 Capacitance-voltage measurements

Figure 4.12 (a) presents capacitance–voltage (C-V) measurements for SNEAM devices with active diameters of 10 µm, 20 µm, and 30 µm. The capacitance measurements were performed on the fully fabricated devices with GSG pads. To eliminate the influence of external probes and cables, short-open calibration was conducted prior to measurements. The measurements were performed by applying a small-signal AC voltage at 0.1 MHz to the PIN device while sweeping the DC bias. The smallest capacitance, measured for the 10 µm active diameter device, is 240 fF beyond -1 V, increasing to 580 fF for the 30 µm active diameter device. This relates to the relation of capacitance $C = \frac{k\epsilon_0 A}{d}$, where k is the relative permittivity of the semiconductor material, ϵ_0 is the permittivity of free space, A is the intrinsic area, and d is intrinsic thickness. For reverse biases more negative than –3 V, the capacitance becomes nearly constant, indicating that the depletion width has expanded to the full intrinsic thickness and additional bias no longer significantly modifies the space-charge distribution. The 30 µm device exhibits more than twice the capacitance of the 10 µm device, demonstrating the dependence of capacitance on the active area. The measured capacitance contains both the intrinsic depletion capacitance of the PIN junction and several parasitic contributions that arise from the device structure. These parasitic components originate from the P and N metal routing, the GSG pads, fringing electric fields at the mesa perimeter where lateral field spreading increases the effective junction area, and capacitive coupling to the underlying stack consisting of SiN/BCB/Au. When considered collectively, these parasitic contributions increases the total capacitance and partly suppress the ideal depletion behaviour expected from the junction. The use of a low permittivity planarization layer would reduce the strength of these parasitic capacitance by

limiting field penetration into surrounding metal and dielectric layers, thereby lowering the overall device capacitance [90].

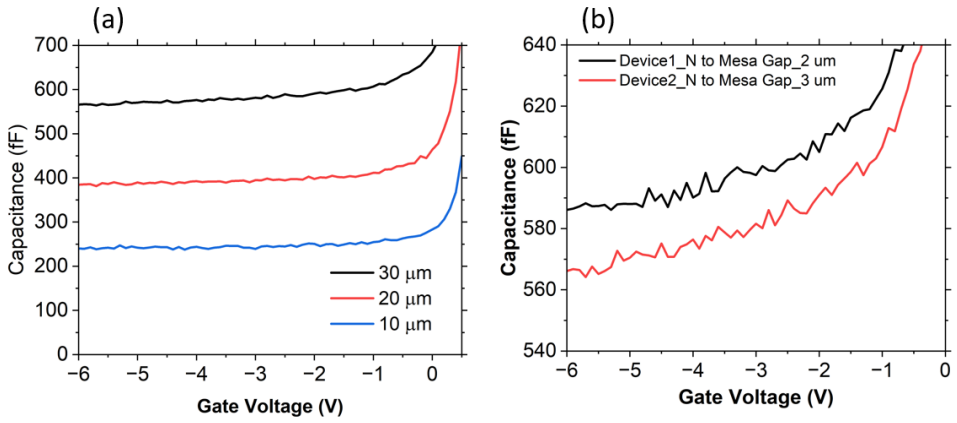


FIGURE 4.12: (a) C-V measurement for a variation of active diameter and (b) Effect of mesa-to-n-contact spacing on the capacitance of a 30 µm active diameter device, comparing spacings of 2 µm and 3 µm.

The effect of n-contact spacing was investigated using 30 µm active diameter devices in which the n-metal contact was positioned at distances of 2 µm and 3 µm from the intrinsic region. These separations were defined by the coupon dimensions established during the source wafer fabrication process. As shown in Figure 4.12 (b) shows the capacitance measured at -6 V decreases from 586 fF for the 2 µm spacing to 566 fF for the 3 µm spacing. This reduction of 4% is attributed to weaker fringing fields and reduced metal semiconductor coupling when the N contact is located farther from the junction. All subsequent electrical and optical characterization employed devices with a 3 µm N contact spacing, as this design was found to be optimal for performance. In efforts to miniaturize the SNEAM device for integration with a chip-on-tip medical diagnostic tool, the trade-offs in chip dimension reduction are mainly constrained by fabrication tolerances and the overall space limitations within the 1 mm outer diameter of diagnostic tool. Capacitance reduction can still be optimized by modifying the intrinsic region properties, such as adjusting the thickness and doping concentration. However, the intrinsic region thickness cannot be arbitrarily increased, as it directly impacts the required reverse bias voltage, which must remain within practical operating limits.

4.5.4 SNEAM electro-optic response

In the previous sections, the results from DC characterizations, including the measurement of FP response and the determination of the optimal bias point from the transfer curve, were discussed. In this section, the bandwidth performance and signal modulation characteristics of the

SNEAM device are analyzed. The electro-optic and data transmission characterization setup used in this work, as well as the associated measurements, were implemented and performed by Asif Khan from the system lab at the Tyndall National Institute. My contribution involved analyzing the resulting measurement data to evaluate the high-frequency performance of the SNEAM device. The experimental setup for electro-optic measurement is illustrated in Figure 4.14 (a), A tunable laser source at 1561.75 nm is used to couple incident light into the SNEAM device through an optical circulator. A bias tee, connected to the SNEAM through a GSG probe, supplies both the high-frequency RF signal and the DC reverse bias simultaneously.

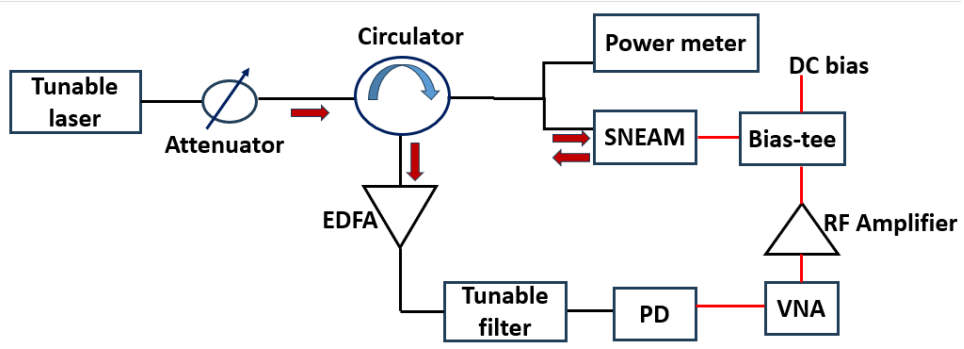


FIGURE 4.13: Schematic of experimental setup for electro-optic measurement.

A vector network analyzer (VNA) is used to generate and analyze the RF signal and is connected to the SNEAM device through the GSG probe. The modulated optical signal is reflected from the device and separated using a circulator, directing it toward a high-speed photodetector for detection. The detected RF signal is fed into the VNA, which measures the amplitude and phase of the reflected signal, producing the S_{21} response over a range of frequencies. To ensure that the measured data accurately represents the device modulation characteristics, the S_{21} response was normalized to the system response. Additionally, the data were processed by applying smoothing and averaging to minimize noise fluctuations.

Figure 4.14 (a) shows the electro-optic bandwidth S_{21} response of SNEAM devices with active diameters of 20 µm and 30 µm both biased at -5 V. The 3 dB roll-off point in the bandwidth curve defines the modulation bandwidth, beyond which the device response begins to decline. The 20 µm device exhibits a 3 dB bandwidth of 16 GHz, whereas the 30 µm device shows a lower bandwidth of 9.4 GHz. This reduction in bandwidth with increasing active diameter is attributed to the higher capacitance associated with the larger device area. These results demonstrate that the SNEAM architecture provides sufficient modulation bandwidth for remote

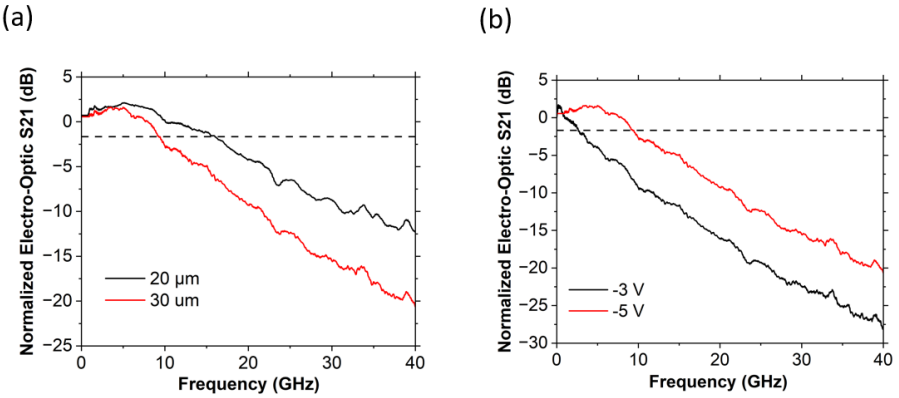


FIGURE 4.14: Normalized electro-optic bandwidth S_{21} of SNEAM devices measured for (a) 20 µm and 30 µm active diameters at -5 V bias, and (b) a 30 µm active diameter at -3 V and -5 V bias.

signalling over distances from 100 m to several kilometers in standard single-mode fiber at 1550 nm, where fiber dispersion and attenuation are low.

$$C = \frac{k\epsilon_o A}{d} \tag{4.5}$$

The capacitance contribution to this active-area-dependent bandwidth reduction was evaluated using the geometrical capacitance relation given in Equation 4.5. In this relation, k is the dielectric constant (approximately ~ 12.9 for AlInGaAs), ϵ_o is the vacuum permittivity and A is the active area of SNEAM and d is the depletion width, defined by the 395 nm intrinsic-region thickness. The calculated geometrical capacitance values are approximately 91 fF and 204 fF for the 20 µm and 30 µm active diameter devices, respectively. This calculated increase with active diameter is consistent with the C-V measurements presented in Subsection 4.5.3, where the fully fabricated devices exhibited the same capacitance trend. The absolute measured capacitance values are higher than the geometrical estimates because the C-V measurement includes parasitic contributions from the metal routing, GSG pads, fringing fields, and coupling to the SiN/BCB/Au stack. This agreement in trend supports the interpretation that the lower measured bandwidth of the 30 µm device is associated with its larger capacitance.

The effect of reverse bias variation on the electro-optic characteristics of the 30 µm device is shown in Figure 4.14 (b). At optimum bias of -5 V, the device exhibit a 3 dB bandwidth of 9.4 GHz. In comparison, operation at -3 V results in a weaker electric field across the MQW region, reducing the strength of QCSE-induced absorption modulation within the FP cavity and causing a more rapid roll-off of the S_{21} response. Consequently, the 3 dB bandwidth decreases

to 2.6 GHz. For remote applications, such as signal modulation from a camera operating at 100 frames per second in a diagnostic tool, low-speed modulation may be sufficient. Operating the device at -3 V would reduce power consumption at the remote end, making it suitable for energy-efficient applications. However, biasing the device at -5 V ensures optimal operation, as it falls within the linear region of the transfer curve.

$$f_{RC} = \frac{1}{2\pi RC} \tag{4.6}$$

$$f = (\frac{1}{f_{RC}^2} + \frac{1}{f_{tr}^2})^{-\frac{1}{2}} \tag{4.7}$$

In analyzing the bandwidth limitations of the SNEAM devices, both the carrier transit time and the RC time constant must be considered. For the 30 µm device, the previously estimated geometrical capacitance was used together with the 40 Ω series resistance extracted from the I–V curve to determine the theoretical RC-limited bandwidth from Equation 4.5. This gives an RC-limited bandwidth of approximately 19 GHz. The carrier transit-time limit was estimated using an electron saturation velocity in AlInGaAs of about $\sim 1 \times 10^{7}$ cm/s and a depletion width of 395 nm. This gives a carrier transit time of 3.95 ps, corresponding to a transit-time-limited bandwidth of 126 GHz using $f_{\mathrm{tr}} \approx 1/(2t_{\mathrm{tr}})$. The overall theoretical bandwidth obtained from Equation 4.7 is therefore about 19 GHz, indicating that the RC response dominates and that the modulation bandwidth is primarily constrained by the device capacitance. Reducing the active area would decrease the capacitance and increase the RC-limited bandwidth, while optimization of the top-side optical coupling could enable the use of smaller active-area devices while maintaining coupling efficiency.

4.5.5 Eye diagram analysis of the modulated signal

Figure 4.15 (a) illustrates the data-transmission experiment conducted using the 30 µm SNEAM device within a bench-top characterization setup. The eye diagram measurement provides a direct assessment of the modulated optical signal from the device with pattern consisting of high and low states and a wide-open eye indicates low noise and high signal quality. A continuous-wave (CW) laser at 1561 nm is fiber-coupled into the SNEAM, while a high-speed RF signal from a bit error rate tester (BERT) is applied through a GSG probe connected to a bias tee. The modulated optical signal is reflected from the SNEAM, then separated using

a circulator, and detected by a high-speed photodetector. The recovered electrical signal is amplified using an RF amplifier and passed through a filter to reduce high-frequency noise, after which the electrical signal is fed into the BERT, for eye diagram analysis and evaluation of signal integrity.

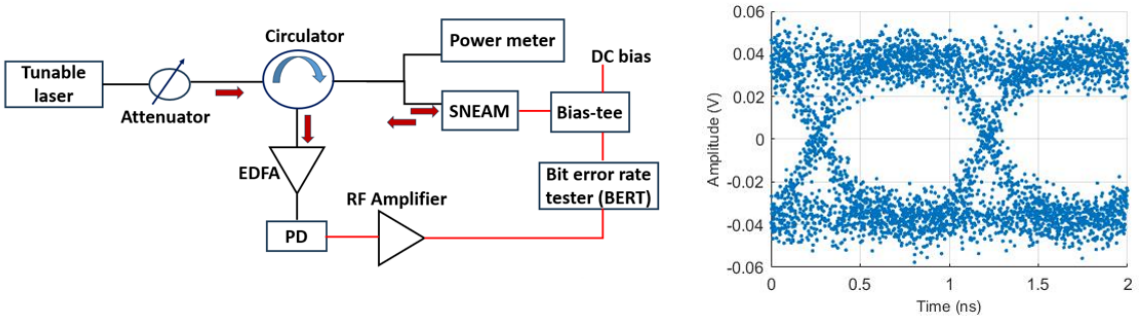


FIGURE 4.15: (a) Schematic of Eye diagram measurement and (b) The SNEAM device modulated with NRZ-OOK signal at 1 Gbps.

A representative eye diagram corresponding to the SNEAM driven at a data rate of 1 Gbps using a non return to zero (NRZ-OOK) ON-OFF signal is presented in Figure 4.15 (b). The eye diagram exhibits a clearly defined eye opening, indicating that the device is able to modulate the incident optical carrier with sufficient amplitude and that the signal settles reliably within each bit period. The vertical eye opening reflects a strong optical extinction ratio, demonstrating effective differentiation between the logical ON and OFF states. The limited spreading of traces between consecutive bits indicates that the influence of one bit on the next is small, showing that the device does not distort the waveform as it switches between states. The steepness of the rising and falling edges demonstrates that the device can change its optical output quickly enough to follow a 1 Gbps. The horizontal eye opening signifies low timing jitter in the recovered signal, which is essential for maintaining deterministic sampling windows in high speed communication systems. These characteristics demonstrate that the SNEAM achieves stable, low noise, and high quality modulation at one gigabit per second, confirming its suitability for gigabit class optical data transmission.

4.6 Conclusion and discussion

We have demonstrated the design, fabrication, and characterization of a SNEAM III–V structure transfer-printed onto a patterned silicon substrate to realize an asymmetric Fabry–Perot response. A SM fiber positioned on the device enables the cavity, defined by the air–semiconductor

interface, the MQW region, the underlying SiN layer used to position the resonant wavelength relative to the QCSE response, and the Au bottom mirror, to exhibit a Fabry–Perot resonance centered at 1560 nm. The DC and high frequency characterization was performed using a 30 µm active device diameter, as it provided more stable fiber alignment and more reliable measurement conditions compared with the 20 µm and 10 µm devices. A static extinction ratio of 6 dB was achieved for reverse-bias voltages ranging from -1 V to -7 V at 1560 nm. Data transmission performance was evaluated using an eye diagram at 1 Gbps, with the device biased at -5 V.

As this transfer-printed, SNEAM configuration has not previously been demonstrated, the work highlights specific challenges associated with the top reflector. In particular, as the SNEAM aperture becomes smaller, even minor variations in the air gap between the fiber end face and the non-planarized top surface can modify the path length and impact the FP response wavelength. Although the 10 µm aperture device exhibits the lowest capacitance and is therefore attractive for high-speed operation, precise optical coupling becomes increasingly challenging under these conditions, contributing to higher insertion loss.

The results establish a clear proof-of-concept for an asymmetric FP cavity implemented through transfer printing using an air–semiconductor interface as the top reflector. Further improvement in system performance can be achieved through simultaneous optimization of the cavity and active region design to address both insertion loss and operating voltage. Increasing the effective top reflectivity by incorporating low-index dielectric layers, such as SiO_2 or SiN, on the top surface would reduce bidirectional fiber–device coupling losses, improve tolerance to fiber positioning, and enable operation closer to the critical-coupling condition, thereby lowering insertion loss and enhancing extinction ratio. This improvement in top reflector design would also reduce packaging related alignment sensitivity, because a more controlled cavity response would decrease the dependence of the reflected signal on small variations in the fiber or lens position during SMF or gradient-index lens based coupling. In parallel, reducing the intrinsic region and MQW thickness increases the electric field across the MQWs for a given applied bias, leading to a stronger QCSE and enabling effective modulation at reduced operating voltages (<5 V), as demonstrated in previous studies [59]. Since modifications to the intrinsic thickness also alters the optical cavity length, the FP resonance, spacer layer thickness, and top reflectivity must be co-optimized to position the resonance at a wavelength that maximizes the voltage induced reflectivity change while limiting residual absorption. The compact footprint and surface-normal configuration of the SNEAM device (80 µm × 87 µm) make it well

suited for co-integration with a photovoltaic cell on the same platform, enabling a self-powered microsystem architecture for chip-on-tip medical diagnostic tools.

Chapter 5

Conclusions and future work

The work presented in this thesis investigated the PPC and the SNEAM as two key components required for power and data over fiber implementation in endoscopic systems. This thesis addressed the development and experimental evaluation of an optical powering and signalling approach capable of supporting remote optical power delivery and data transmission within the stringent electrical, optical, and dimensional constraints of minimally invasive endoscopic systems, targeting an overall device footprint of approximately 1 mm $\times$ 1 mm while ensuring extreme miniaturization, reliable in-body operation, and immunity to electromagnetic interference.

The optical power conversion was demonstrated using PPCs investigated under both edge-coupled and surface-normal illumination configurations. Edge-coupled PPCs achieved a V_{oc} of 0.83 V in single-junction devices with an overall fiber-to-device efficiency of 34%, and optical power delivery and upstream data transmission at rates up to 500 Mb/s confirmed combined power and signalling operation within a single optical link. Voltage scaling was demonstrated through stacked junctions, achieving an V_{oc} of 3.6 V at an optical input power of 10 mW with η of 36%. Gaussian beam coupling produced non-uniform optical intensity across the stacked junctions, resulting in photocurrent mismatch that constrained carrier extraction and η. Surface-normal PPC operation using four laterally segmented GaAs-based devices illuminated via a double-clad fiber achieved peak efficiencies approaching 50%, with quasi-Gaussian illumination achieving a V_{max} of 4.02 V at 10.4 W/cm^2 using a fiber-to-device spacing of 1 mm, and annular illumination achieving efficiencies of 48.6% at 20.8 W/cm^2 and 47.5% at 62.4 W/cm^2 at a reduced spacing of 0.4 mm, while sustaining a V_{oc} of 4.77 V and a V_{max} of 4 V at the highest irradiance. Optimization of fiber-to-device spacing and illumination profile

was shown to be critical for uniform segment-to-segment power delivery, with annular beam delivery providing improved optical confinement along the device perimeter.

A SNEAM suitable for remote optical signalling in power-over-fiber systems was demonstrated using a transfer-printed III–V device integrated with an asymmetric FP cavity. The device exhibited a static extinction ratio of 8 dB under reverse bias between -1 V and -7 V at 1560 nm and supported data transmission at 1 Gb/s using single-mode fiber coupling. The compact footprint and surface-normal geometry of the realized design support compatibility with co-integration alongside PPC within a shared optical interface. Within the scope of this thesis, the PPC and SNEAM were developed and experimentally validated as individual components; however, a fully integrated PPC–SNEAM system enabling simultaneous optical power delivery and data transmission was not demonstrated. Key challenges identified include illumination configuration and uniformity in stacked and segmented PPCs, optical coupling sensitivity, cavity-length control in surface-normal modulators, and reduction of operating voltage for active components. The results establish a validated set of functional building blocks and define practical design constraints to guide future integration efforts. The following section summarizes the main results from Chapters 2, 3, and 4 and outlines directions for future work in Section 5.2 aimed at addressing these challenges and suggestions toward fully integrated optically powered endoscopic systems.

5.1 Overview of the results

Chapter 2 focused on demonstrating laser-to-laser photonic power conversion using an edge-coupled configuration. A packaged 1470 nm pump laser coupled to a 1550 nm single junction receiver achieved an internal conversion efficiency of 55% and an overall fiber to device efficiency of 34%, delivering an open circuit voltage V_{oc} of 0.83 V. The same configuration supported upstream data transmission at 500 Mb/s without external electrical biasing, while the single junction PPC delivered a vmax of approximately 0.6 V. Measurements using a 1060 nm receiver pumped at 980 nm achieved a V_{oc} of 1.07 V with a fiber to device efficiency of 23%. Voltage scaling was demonstrated using a triple stacked p–n junction receiver operating at 905 nm and pumped at 850 nm, achieving a V_{oc} of 3.6 V with a fiber to device efficiency of 35%. Performance limitations observed across the 1060 nm and 905 nm receiver configurations included sensitivity to fiber to chip alignment, residual facet reflectivity, and non uniform illumination, each of which contributed to reduced carrier extraction and conversion efficiency.

Additional uncertainty arose from limited knowledge of the receiver epitaxial design, which constrained detailed analysis of carrier collection dynamics. The results indicate that improved mode matching between SMF and the waveguide facet, the use of dedicated tapered coupling structures, enhanced illumination uniformity through beam shaping, and band structure engineering to facilitate carrier escape would significantly enhance performance. When considered collectively, these findings demonstrate that edge-coupled PPC retain strong potential for optimized on-chip photonic power conversion and co-integration with additional electronic and photonic components, supporting broader application in highly miniaturized systems, including optical powering of endoscopic micro-camera platforms.

Chapter 3 investigated surface-normal PPC using laterally interconnected GaAs-based PPC illuminated via a DCF to generate quasi-Gaussian and annular beam profiles. The results established the critical role of fiber-to-device spacing and illumination geometry in determining power delivery uniformity and electrical performance in segmented PPCs. For devices with an active diameter of 350 µm, quasi-Gaussian illumination achieved a peak efficiency of 50% at an irradiance of 10.4 W/cm^2 with a fiber-to-device spacing of approximately 1 mm. Annular illumination, generated and validated using identical devices, achieved a peak efficiency of 48.6% at an irradiance of 20.8 W/cm^2 at a reduced spacing of 0.4 mm, while sustaining higher operating voltages at increased optical power. At an irradiance of 62.4 W/cm^2, annular illumination delivered an open-circuit voltage V_{oc} of 4.78 V, a maximum operating voltage V_{max} of 4.3 V, and an electrical output power of approximately 27 mW The annular illumination profile concentrated optical power near the perimeter of the segmented PPC, improving segment-to-segment irradiance uniformity and reducing series resistance effects relative to central illumination, which is beneficial for laterally connected architectures as the number of segments increases to achieve higher output voltage. Measurements performed on both Chip 1 and Chip 2 identical devices exhibited consistent spacing-dependent trends under both illumination schemes, demonstrating repeatability. Increasing the effective NA of the delivery fiber improved tolerance to fiber positioning and spacing variations while maintaining well-defined annular illumination. Furthermore, the fiber-based nature of the DCF illumination scheme provides opportunities for integration with optical modulation or multiplexing techniques, enabling simultaneous power and signal delivery in future POF architectures.

Chapter 4 presented the SNEAM developed for remote optical signalling. The SNEAM on InP platform transfer-printed onto a patterned reflector, was designed to operate in an asymmetric FP configuration with a resonance centred near 1560 nm. Its design in the asymmetric cavity

arrangement, together with the fabrication steps required for assembling the device on the target substrate, was described in detail. Measured performance included a static extinction ratio of 8 dB for reverse biases between –1 V and –7 V, a 3 dB bandwidth of 9 GHz at 1560 nm for a –5 V bias, and data transmission demonstrated at 1 Gbps using a 6 V drive voltage. Device-scale constraints were also reported, including sensitivity of the FP path length to variations in the air gap between the fiber end-face and the non-planarized surface, as well as coupling limitations observed when the modulator aperture was reduced to 10 µm. The chapter concluded by outlining strategies for enhancing device performance, including increasing the top-reflector strength through additional dielectric layers and reducing the intrinsic region thickness to achieve lower operating voltage.

5.2 Future Work

The work presented here considers the integrated design of the PPC–SNEAM system using both single-fiber solution. Co-integrating these two components on a common platform is a key requirement for achieving simultaneous optical power delivery and signal transmission in minimally invasive surgical tools. Future work will therefore focus on design refinement and packaging strategies that enable compact co-integration within the spatial constraints of a 1 mm endoscopic form factor.

The suggested integration concept and single-fiber implementation using a DCF are illustrated in Figure 5.1. This layout integrates a 30 µm active diameter SNEAM at the center of a 350 µm active diameter segmented PPC, with transfer printing identified as a suitable technique for central placement without degrading device performance. Results from Chapter 3 demonstrated that annular illumination concentrated near the PPC edges provides performance comparable to Gaussian illumination while offering improved uniform coverage across the four segmented regions, particularly at small fiber-to-device separations.

The wavelength-allocation and illumination strategies summarized in Table 5.2 are directly referenced to the integrated PPC–SNEAM layout shown in Fig. 5.1 and describe viable operating choices for the proposed DCF-based single-fiber implementation. These configurations highlight the trade-offs between PPC efficiency, SNEAM performance, and illumination geometry within the central-SNEAM and annular-PPC architecture. One configuration employs a

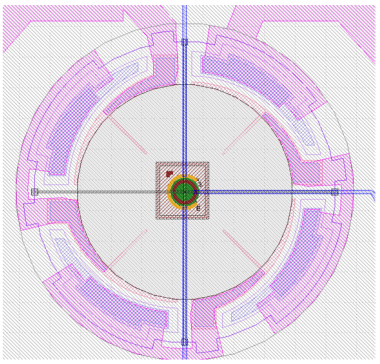


FIGURE 5.1: Layout showing the centrally positioned SNEAM with 30 µm on four segmented PPC with 350 µm.

shorter-wavelength PPC combined with a longer-wavelength SNEAM, enabling annular illumination of the PPC and central illumination of the SNEAM to mitigate SNEAM saturation. However, operation of the PPC at longer wavelengths requires increased junction segmentation to achieve the required electrical output voltage, while the higher electroabsorption at shorter wavelengths benefits SNEAM modulation efficiency. In this configuration, both annular and Gaussian illumination profiles are feasible, although Gaussian illumination introduces optical loss due to the limited SNEAM aperture. For short-reach, low-voltage, and low-power operation, this trade-off may be acceptable. An alternative configuration, where both PPC and SNEAM operate at shorter wavelengths, is advantageous for both devices in terms of absorption efficiency and aligns well with the suggested central-SNEAM and annular illumination on PPC as in the layout, allowing either annular or Gaussian illumination without inducing SNEAM saturation.

In contrast, MCF support longer-wavelength PPC and SNEAM combinations but require careful matching of the PPC active diameter to the adjacent core-to-core spacing in the MCF geometer. Customizing the MCF geometry, including tailored core-to-multimode transitions, offers a pathway to relax this constraint and avoid unnecessary expansion of the device perimeter. As commonly reported in the literature, reducing the photovoltaic device area increases the perimeter-to-area ratio, leading to enhanced sidewall surface recombination losses, which must be mitigated through device and surface-passivation optimization.

TABLE 5.1: Comparison of wavelength and illumination configurations for integrated PPC–SNEAM POF link.

SNEAM wavelength (nm)	**PPC wavelength** (nm)	**Illumination scheme**	**Fiber**	**Advantage**	**Disadvantage**
1300 / 1500	850	Annular (PPC), Gaussian (SNEAM)	DCF (Inner cladding-PPC, Core-SNEAM)	High PPC efficiency at 850 nm using GaAs material system	Additional SNEAM design required to mitigate saturation at optical powers $\gtrsim$1 mW [91–94]
850	1300	Gaussian- PPC, SNEAM	DCF / MMF	High extinction ratio ($\sim$50 dB) with reflective EAM based on GaAs–$Al_{0.2}Ga_{0.8}As$ [79]	Increased series interconnect complexity to achieve $\sim$4 V; penalty associated with multimode operation on SNEAM
780	850	Gaussian or Annular (PPC)	DCF / MMF	Approximately 4 V delivered from multi-junction GaAs PPC and extinction ratio exceeding 10 dB using $Al_{0.3}Ga_{0.7}As$–GaAs [95]	Non-telecom wavelength with limited availability of compact, fiber-integrated components compared with C-band systems
1300	1550	Gaussian (PPC, SNEAM)	DCF	Compatibility with standard telecom communication bands (1260–1650 nm)	Low PPC junction voltage (0.4–0.5 V) requiring approximately eight series-connected junctions to achieve 4 V

Performance values are indicative and depend on device design and illumination conditions.

Building on these findings, future integrated designs will employ 850 nm annular illumination delivered through the multimode inner cladding of the DCF to power the PPC, while the single-mode core enables bidirectional signal transmission at 1550 nm for reflective SNEAM operation. The choice of 850 nm is motivated by the need for efficient remote powering of endoscopic microsystems, where the PPC and associated electronic interface circuitry are co-designed to meet the power and voltage requirements of the micro-camera, which defines the primary load specification. At this wavelength, the PPC can provide sufficient electrical output to support both modulation functions and auxiliary electronic subsystems. The electrical output of the PPC is interfaced with a power management circuit that conditions and distributes the harvested energy to multiple local power delivery points within the endoscopic platform.

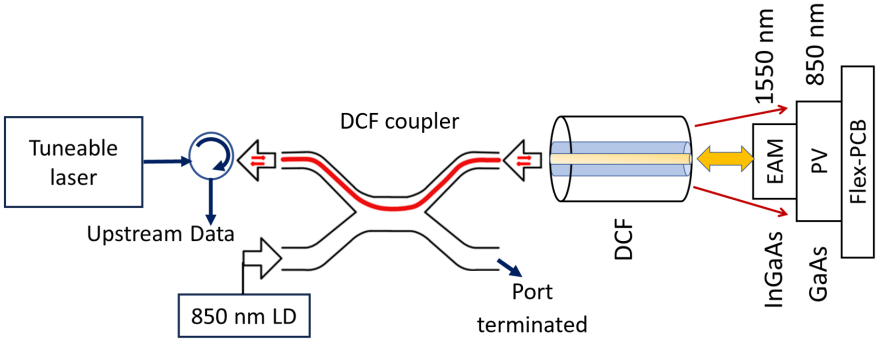


FIGURE 5.2: Schematic of single fiber solution using a DCF and a DC1300LQ2FA 2 × 1 DCF coupler to simultaneously launch 850 nm annular illumination into the inner cladding and support bidirectional 1550 nm signal transmission through the single mode core of DCF-13.

Electrical access to the centrally integrated SNEAM is achieved by routing metal interconnects through the trenches separating the PPC segments and insulating them with SiN, ensuring that the PPC active area remains undisturbed. The annular illumination approach is particularly attractive because, under ideal conditions, the central region where the SNEAM is located experiences minimal optical intensity. However, future work must focus on optimizing the annular beam diameter to achieve speckle-less and more uniform illumination across all PPC segments using a higher-NA core, with the annular ring width constrained to within 100 µm from the PPC edge. This is required to ensure that illumination remains confined to the PPC active regions and does not extend into the central area. This consideration is especially important because the SNEAM material exhibits absorption at the PPC power-delivery wavelength, and the thin MQW absorber can be sensitive to residual optical exposure. The spatial distribution of the annular illumination and the resulting central-region intensity are experimentally evaluated in Figure 5.3.

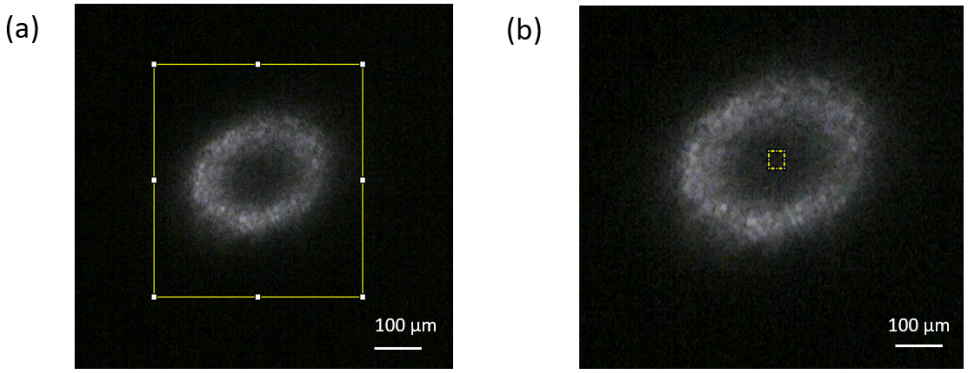


FIGURE 5.3: Power ratios calculated from raw annular beam images using background corrected integrated intensities extracted in ImageJ for a 350 µm diameter annular beam on a diffuse target. The highlighted rectangle indicates (a) the annular beam and background region and (b) 30 µm wide region used to estimate the fraction of optical power present at the beam center.

Experimental measurements of the annular beam profile show that a small fraction of the total optical power can be present at the beam center. Image analysis revealed that approximately 0.35% of the annular beam power overlaps with a 30 µm-wide central region, as shown in Figure 5.3. For an annular illumination power of 100 mW, this corresponds to approximately 0.35 mW incident at the center. These results highlight the importance of continued beam-shaping and illumination-profile optimization to ensure robust operation of the integrated PPC SNEAM on same platform.

The wavelength choices explored in this thesis were guided by both device-level performance and system-level considerations. The 850 nm wavelength was selected to maximize PPC conversion efficiency, while telecom wavelengths (1550 nm) were chosen for the SNEAM to enable compatibility with established short- and long-haul optical communication infrastructure. As an alternative direction, future work will also consider 780 nm operation for the EAM, enabled through appropriate MQW and material design. This approach would allow greater functional separation between optical power transfer and modulation while preserving efficient PPC operation and flexible signal transmission.

A further extension of the proposed integration strategy involves aligning the PPC and SNEAM on the same platform with the electrical requirements of a customized image sensor currently under development by the Microelectronics Circuits Centre Ireland (MCCI) group at Tyndall for distal-end operation. This requires establishing key interface parameters such as supply voltage levels, current consumption, and overall power budget for the sensor. With these

requirements defined, the PPC design can be adapted to provide the necessary electrical output, while the SNEAM geometry and placement can be refined to ensure dimensional and functional compatibility within a shared integration platform. This progression enables the integrated PPC and SNEAM concept to move beyond commercially available image sensors toward application specific imaging systems.

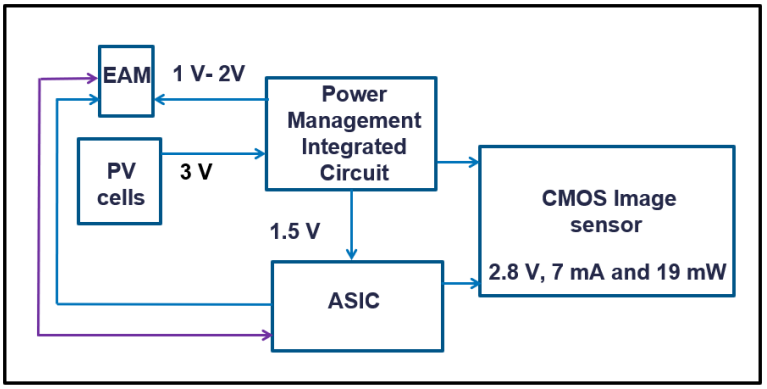


FIGURE 5.4: Block diagram illustrating the voltage distribution through the power management integrated circuit (PMIC) to the various system components, highlighting the supply requirements of the customized CMOS image sensor.

In considering the customized image sensor specification, in addition to the DCF-based single-fiber solution, further opportunities arise when considering reduced image-sensor voltage requirements and tighter footprint constraints. While reducing the annular beam diameter supports smaller PPC designs, it also increases the challenge of maintaining spatial separation between annular and central illumination. This motivates exploration of MCF as a complementary single-fiber solution. By enabling spatial separation of power and signal channels at the fiber level, MCF provides additional degrees of freedom for illumination control and reduces reliance on precise annular beam shaping at the device interface, with the potential to further reduce integrated chip footprint.

A second proposed chip layout adapted to the selected MCF core geometry (SM-4C1500) positions three PPC elements and one SNEAM to match the MCF core configuration, as shown in Figure 5.5 (a). An overview of the complete chip layout is shown in Figure 5.5 (b), where packaging considerations, including the incorporation of a 0.25 mm-diameter fiber ferrule, are taken into account. While the initial layout envelope corresponds to a chip dimension of 1.65 mm $\times$ 1.8 mm, further layout optimization allows the active integration region to be reduced to approximately 650 µm $\times$ 750 µm, while remaining compatible with fiber alignment and packaging constraints. To investigate the feasibility of this MCF based layout, the PV design was modified from a four-segment PPC architecture to a single-junction GaAs PPC

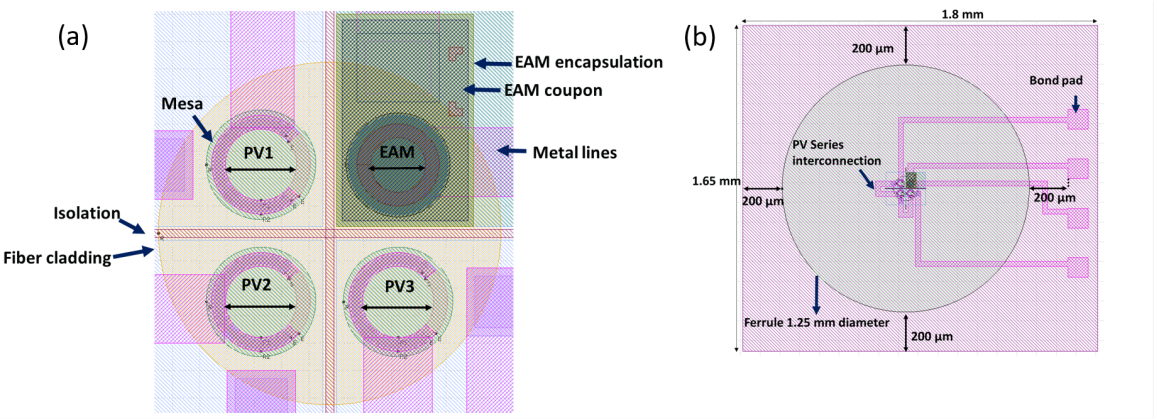


FIGURE 5.5: Suggested integrated layout of three single-junction PPCs (26 µm active diameter) connected in series and a central EAM (20 µm active area). (a) Detailed device-level layout adapted for MCF illumination. (b) Chip-level overview showing the overall chip dimensions 1.65 mm × 1.8 mm, including fiber ferrule and wire bonding for packaging.

with an active diameter of 26 µm, while a 20 µm-diameter SNEAM was positioned at a 50 µm separation from the PPC center to match the MCF core-to-core spacing.

A MCF based optical link is proposed in the Figure 5.6, to enable simultaneous optical power delivery and signal transmission within a four-core. In this scheme, three MCF cores will function on optical power delivery at 850 nm, while the remaining core supports bidirectional SNEAM signalling in the O-band and C-band, utilizing the transceiver capability of the SNEAM [96]. This approach allows independent optimization of the power and data channels while maintaining a compact single-fiber design.

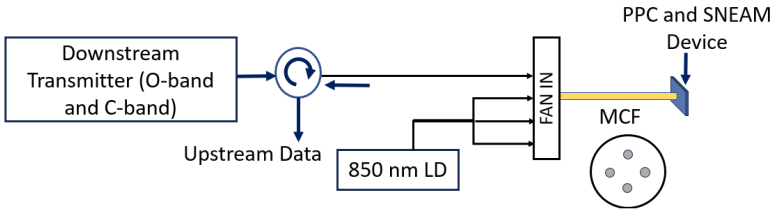


FIGURE 5.6: Schematic of experimental design on MCF as single fiber solution on illumination of PPC and bidirectional single transmission.

Overall, this chapter presents future design directions motivated by the demanding requirements of device miniaturization, power delivery, and integration in minimally invasive surgical tools. Within this context, power-over-fiber is an emerging approach for enabling remote powering and optical signalling at the distal end, and the continued development of the PPC and SNEAM will focus on improving device-level performance and integration to support such implementations. In this way, the results presented in this thesis contribute to the advancement of

POF-enabled photonic devices and provide a basis for further exploration of compact, optically powered solutions for biomedical applications.

Appendix A

Appendix

A.1 Python Code for Gaussian Power Distribution Analysis

```
import numpy as np
import matplotlib.pyplot as plt
from math import erf, sqrt, pi

# ============================================================
# Absolute geometry (micrometers)
# Segments have relative heights: [2,1,1,1,2] * (L/7)
# Middle three (segments 2,3,4) total height = 3*(L/7) = 10  m
# => L = 10 * 7/3  m
# ============================================================
MIDDLE3_HEIGHT_UM = 10.0
L_UM = MIDDLE3_HEIGHT_UM * 7.0 / 3.0  # 23.333...  m

# Pick spot sizes in absolute units ( m )
spot_sizes_um = [4.0, 6.0, 8.0, 10.0]

# Beam center ( m )
x0_um, y0_um = 0.0, 0.0



# ----------------------------
# Math helpers
# ----------------------------
```

```
def int_gauss_1d(a, b, u0, w):
    """  _a  ^b exp(-2 (u-u0)^2 / w^2) du"""
    return (w/2) * sqrt(pi/2) * (
        erf(sqrt(2)*(b-u0)/w) - erf(sqrt(2)*(a-u0)/w)
    )

def y_edges_2_1_1_1_2(L):
    """
    5 horizontal segments spanning y     [-L/2, +L/2]
    with relative heights [2,1,1,1,2].
    """
    h = L / 7.0
    heights = np.array([2, 1, 1, 1, 2], dtype=float) * h
    edges = [-L/2]
    for dh in heights:
        edges.append(edges[-1] + dh)
    return np.array(edges)

def segment_powers_fraction_of_total_beam(L, w, x0=0.0, y0=0.0):
    """
    Returns power in each segment as a fraction of TOTAL beam power.
    Gaussian normalized so total power = 1.
    """
    y_edges = y_edges_2_1_1_1_2(L)
    I0 = 2.0 / (pi * w * w)

    Fx = int_gauss_1d(-L/2, L/2, x0, w)
    Fy = np.array([
        int_gauss_1d(y_edges[i], y_edges[i+1], y0, w)
        for i in range(5)
    ])

    return I0 * Fx * Fy, y_edges

def power_transfer_efficiency_percent(L, w, x0=0.0, y0=0.0):
    """
    Middle three segments are series-connected.
      (%) = 100    3    min(P2, P3, P4)
```

```
    """
    P, _ = segment_powers_fraction_of_total_beam(L, w, x0, y0)
    usable = 3.0 * np.min(P[1:4])
    return 100.0 * usable


# ============================================================
# Figure 1: Gaussian profiles and segment power histograms
# ============================================================
def plot_gaussians_and_histograms(L, spot_sizes, x0=0.0, y0=0.0, n=450):
    seg_labels = ["Seg 1", "Seg 2", "Seg 3", "Seg 4", "Seg 5"]
    y_edges = y_edges_2_1_1_1_2(L)

    fig = plt.figure(figsize=(4.0*len(spot_sizes), 7.2))
    gs = fig.add_gridspec(2, len(spot_sizes), height_ratios=[1.2, 1.0])

    x = np.arange(5)
    last_im = None

    for j, w in enumerate(spot_sizes):
        ax_img = fig.add_subplot(gs[0, j])
        xs = np.linspace(-L/2, L/2, n)
        ys = np.linspace(-L/2, L/2, n)
        X, Y = np.meshgrid(xs, ys)

        I = np.exp(-2*((X-x0)**2 + (Y-y0)**2)/w**2)
        last_im = ax_img.imshow(
            I, extent=[-L/2, L/2, -L/2, L/2], origin="lower"
        )

        for y in y_edges[1:-1]:
            ax_img.plot([-L/2, L/2], [y, y], "k", lw=1.2)

        eta = power_transfer_efficiency_percent(L, w, x0, y0)
        ax_img.set_title(f"w = {w:.2f}  m \n  = {eta:.1f}%")
        ax_img.axis("off")

```

```
99          ax_bar = fig.add_subplot(gs[1, j])
100         P, _ = segment_powers_fraction_of_total_beam(L, w, x0, y0)
101         ax_bar.bar(x, 100*P)
102         ax_bar.set_xticks(x)
103         ax_bar.set_xticklabels(seg_labels)
104         ax_bar.set_ylim(0, 100)
105         ax_bar.grid(alpha=0.3)
106
107     cax = fig.add_axes([0.92, 0.57, 0.015, 0.28])
108     fig.colorbar(last_im, cax=cax, label="Relative intensity")
109     plt.show()
110
111
112 # ============================================================
113 # Figure 2: Efficiency vs spot size
114 # ============================================================
115 def plot_efficiency_curve(L, w_min=0.5, w_max=15.0, N=400):
116     ws = np.linspace(w_min, w_max, N)
117     eta = [power_transfer_efficiency_percent(L, w) for w in ws]
118
119     plt.figure(figsize=(7.2, 4.4))
120     plt.plot(ws, eta)
121     plt.xlabel("Spot size w ( m )")
122     plt.ylabel("Power transfer efficiency    (%)")
123     plt.grid(alpha=0.3)
124     plt.show()
125
126
127 # ============================================================
128 # Run
129 # ============================================================
130 plot_gaussians_and_histograms(L_UM, spot_sizes_um, x0_um, y0_um)
131 plot_efficiency_curve(L_UM, 1.5, 20.0)
```

Listing A.1: Gaussian beam power distribution and transfer efficiency calculation

A.2 SPICE analysis of series junction current limitation

Figure A.2.1 presents SPICE-based simulations used to analyse current limitation in series-connected photovoltaic junctions using equivalent circuit models. Each junction is represented by a silicon diode connected in parallel with an ideal current source, which sets the current supplied to the junction. In the single-junction configuration Figure A.2.1 (a), a current source of 100 mA drives the diode, resulting in an external current I_{ext} of 100 mA and an output power of approximately 60 mW. When three identical junction models are connected in series and driven by equal current sources Figure A.2.1 (b), the terminal voltage increases due to voltage addition across the junctions, while the external current is reduced to 33.3 mA and the delivered power remains unchanged. In contrast, when unequal current sources are applied to the series-connected junctions Figure A.2.1 (c), the external current is limited by the lowest current source, resulting in a reduced output power of approximately 40 mW. These simulations demonstrate that in series-connected junction circuits, current mismatch constrains the extractable electrical power despite increased terminal voltage.

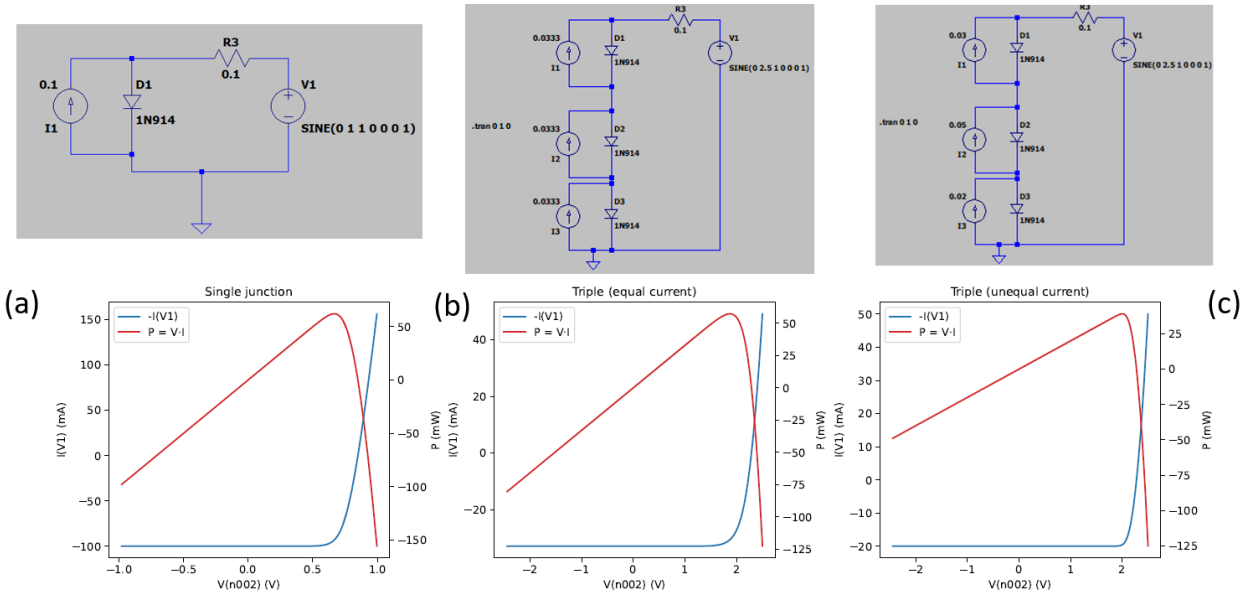


FIGURE A.2.1: SPICE-based circuit models and simulated I-V and P-V characteristics illustrating current limitation in series connected diode circuits. (a) single junction circuit driven by a current source with I_{ext}=100 mA, delivering of 60 mW; (b) three series connected diode circuits driven by equal current sources, resulting in voltage addition with I_{ext}=33.3 mA and unchanged output power of 60 mW; (c) three series connected diode circuits driven by unequal current sources, where I_{ext}=20 mA, leading to reduced output power of 40 mW.

A.3 Epitaxial details and layout of the four-segment PPC

The epitaxial layers used in the fabrication of the four-segment PPC are listed in Table A.3.1. The four laterally segmented PPCs, connected in series, were fabricated using the layout shown in Figure A.3.1. The process involved multiple lithography levels, deposition, and etching steps to define the device features, including p metal contacts, anti-reflection coating openings, mesa structures, n-contacts, interconnection metal lines, and isolation trenches.

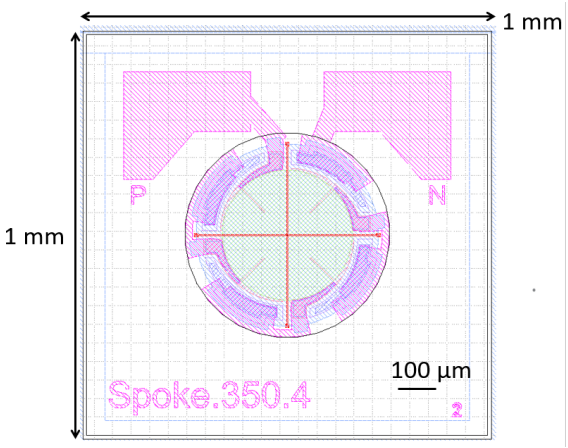


FIGURE A.3.1: Layout design of 350 µm active diameter PPC in 1 mm × 1 mm chip.

TABLE A.3.1: Epitaxial layer stack for the four-segment GaAs PPC.

Layer #	Layer name / material	Thickness	Doping
1	p++ GaAs cap	200 nm	$\sim 1 \times 10^{19}\,\mathrm{cm}^{-3}$
2	p+ $Al_{0.8}Ga_{0.2}As$ FSF	40 nm	$\sim 1 \times 10^{18}\,\mathrm{cm}^{-3}$
3	p+ GaAs emitter	400 nm	$2 \times 10^{18}\,\mathrm{cm}^{-3}$
4	n− GaAs base	3 µm	$3 \times 10^{17}\,\mathrm{cm}^{-3}$
5	n+ $Al_{0.3}Ga_{0.7}As$ BSF	40 nm	$\sim 1 \times 10^{18}\,\mathrm{cm}^{-3}$
6	n+ GaAs LCL	1 µm	$1 \times 10^{18}\,\mathrm{cm}^{-3}$
7	s.i. GaAs substrate	350 µm	semi-insulating

A.4 Camera specification

https://www.dino-lite.com/products$_d$etail.php?$index_m1_id = 3index_m2_id = 5index_id = 149$

A.5 Single junction micro PPC in surface normal illumination

Preliminary experiments were conducted using single-junction GaAs PPC illuminated under surface-normal incidence through standard single-mode fibers (SMF) to establish the achievable current, voltage, and power levels of an individual micro-scale photovoltaic device. This approach was adopted because the available MCF did not include a fan-out, and the short illumination link length allows SMF-based testing to provide a reliable baseline for optical coupling efficiency and alignment sensitivity. The fabricated micro-PPCs, with an active diameter of 26 µm, were characterized without an ARC, resulting in additional optical reflection losses. The measured power conversion efficiency of approximately 24% is consistent with reported trends in GaAs-based micro-PPC, where efficiency improves with increasing active aperture size due to a reduced perimeter-to-area ratio, while scaling to very small lateral dimensions causes recombination and leakage at etched mesa sidewalls to dominate, leading to enhanced non-radiative losses and degraded carrier extraction in small aperture devices [97].

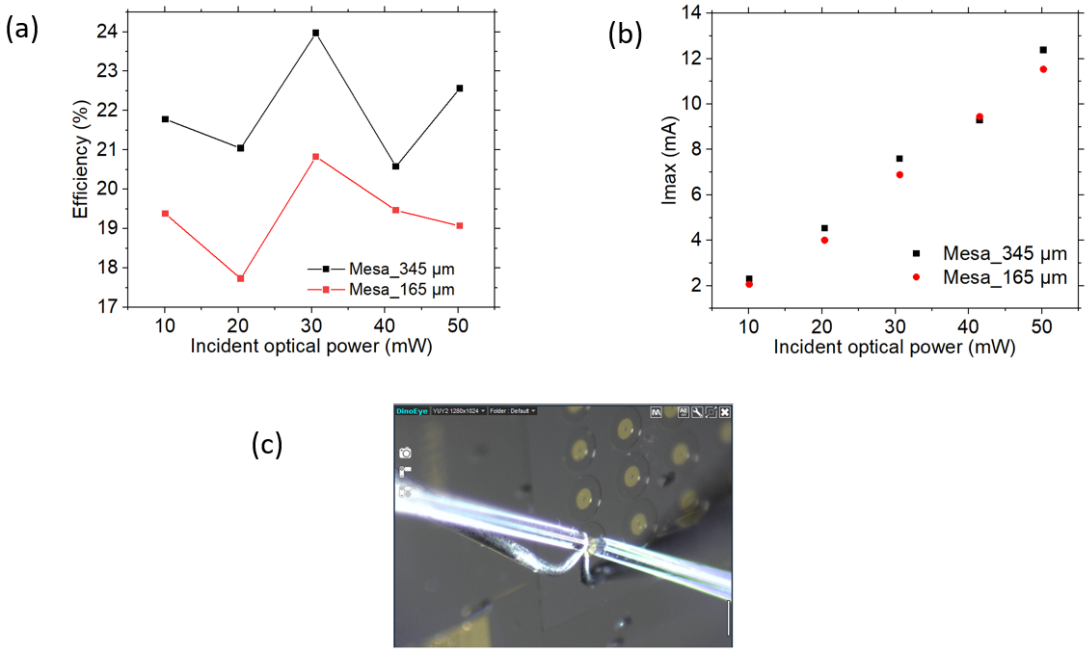


FIGURE A.5.1: Single junction GaAs PPC performance with a 26 µm active diameter and different mesa sizes. (a) Conversion efficiency and (b) maximum output current as functions of incident optical power, measured with a fiber to device separation of 40 µm during probing. (c) Picture of SMF aligned surface normal to device with 365 µm Mesa diameter.

A GaAs based single junction device was fabricated using a two step process. The first step involved defining and depositing the p-type metal, while the second step consisted of mesa definition and etching. Since the material was grown on a semi-insulating substrate, depositing the n-type metal on the backside of the substrate was not feasible within a two level process.

To enable initial testing on the micro PPC, a shadow mask, such as a Si piece, was placed on selected device regions to protect them, while the remaining areas were exposed for subsequent n-metal deposition. The fabricated device demonstrated an open-circuit voltage of 0.9 V and a maximum output current of 7.6 mA, as shown in Figure A.5.1. These results provide a quantitative baseline for estimating the electrical output of a multi-junction PPC architecture in which individual junctions are illuminated through separate cores of an MCF and electrically connected in series to achieve higher output voltages. For micro-scale devices, the experimental results further indicate that increasing the mesa diameter from 165 µm to 365 µm resulted in an approximately 10% increase in maximum output current at an incident optical power of 30 mW. This improvement is attributed to the reduced perimeter-to-area ratio associated with larger mesas, which lowers the relative impact of recombination and leakage at etched mesa sidewalls that otherwise dominate carrier losses in small-aperture devices. These findings highlight the fundamental trade-off between footprint reduction and extraction efficiency in micro-scale PPCs and motivate further optimization of mesa geometry, sidewall passivation, optical confinement, and ARC integration.

A.6 Image Analysis and Intensity Quantification Algorithms

This appendix summarizes the numerical routines used to extract beam centers and to quantify optical intensity outside a fixed physical radius. The implementations are provided to ensure transparency and reproducibility. An initial version of the numerical model was developed by Brendan Roycroft in MATLAB. The model was subsequently reimplemented and modified in Python by the author for use in this work.

A.6.1 Two-Dimensional Gaussian Beam Fits

For approximately Gaussian beam profiles, the beam center is obtained by fitting a two-dimensional Gaussian intensity distribution to the measured image data.

The model function is defined as

$$I(x,y) = A\exp\left[-\frac{(x-x_0)^2}{2\sigma_x^2} - \frac{(y-y_0)^2}{2\sigma_y^2}\right] + I_0, \tag{A.1}$$

where (x_0, y_0) denote the beam center, σ_x and σ_y are the spatial widths, and I_0 is a constant offset.

The corresponding numerical implementation is given below.

```
def twoD_gaussian(coords, A, x0, y0, sx, sy, offset):
    x, y = coords
    return (
        A * np.exp(
            -((x - x0)**2 / (2*sx**2)
              + (y - y0)**2 / (2*sy**2))
        ) + offset
    ).ravel()
```

The Gaussian parameters are obtained by nonlinear least-squares minimization. Only the fitted center coordinates are used for subsequent analysis.

```
def fit_gaussian_2d(img):
    h, w = img.shape
    x = np.arange(w)
    y = np.arange(h)
    X, Y = np.meshgrid(x, y)

    A0 = np.max(img) - np.min(img)
    x0_0, y0_0 = np.unravel_index(np.argmax(img), img.shape)[::-1]
    sx0, sy0 = w / 5, h / 5
    offset0 = np.median(img)

    p0 = (A0, x0_0, y0_0, sx0, sy0, offset0)

    try:
        popt, _ = curve_fit(
            twoD_gaussian,
            (X, Y),
            img.ravel(),
```

```
            p0=p0,
            maxfev=3000
        )
        _, x0, y0, sx, sy, _ = popt
        return x0, y0, sx, sy
    except Exception:
        return x0_0, y0_0, sx0, sy0
```

—

A.6.2 Radial Ridge Extraction and Circle Fitting

For annular beam profiles, the center is determined by extracting ridge points from radial intensity profiles and fitting them to a circle.

```
def find_ring_points(img, cx, cy, n_angles=360, smooth_sigma=2.0):
    h, w = img.shape
    r_max = int(0.5 * min(h, w)) - 2
    r_min = int(0.05 * min(h, w))

    k = gaussian_kernel_1d(smooth_sigma)
    pts = []

    for ktheta in range(n_angles):
        theta = 2 * np.pi * ktheta / n_angles
        rs = np.arange(r_min, r_max + 1, dtype=np.float32)
        xs = (cx + rs * np.cos(theta)).astype(np.float32)
        ys = (cy + rs * np.sin(theta)).astype(np.float32)

        prof = cv2.remap(
            img.astype(np.float32),
            xs.reshape(1, -1),
            ys.reshape(1, -1),
            interpolation=cv2.INTER_LINEAR,
```

```
            borderMode=cv2.BORDER_CONSTANT,
            borderValue=0
        ).ravel()

        if len(k) > 1:
            prof = np.convolve(prof, k, mode="same")

        r_peak = rs[np.argmax(prof)]
        x = cx + r_peak * np.cos(theta)
        y = cy + r_peak * np.sin(theta)

        if 1 <= x < w - 1 and 1 <= y < h - 1:
            pts.append([x, y])

    return np.array(pts)
```

The extracted ridge points are fit to a circle using an algebraic least-squares method with iterative trimming to suppress outliers.

```
def robust_circle_fit(points, trims=2, trim_frac=0.15):
    P = points.copy()
    for _ in range(trims):
        x, y = P[:, 0], P[:, 1]
        D = np.column_stack([x, y, np.ones_like(x)])
        z = x**2 + y**2

        A, B, C = np.linalg.lstsq(D, -z, rcond=None)[0]
        cx, cy = -A / 2, -B / 2
        R = np.sqrt((A*A + B*B)/4 - C)

        r = np.sqrt((x - cx)**2 + (y - cy)**2)
        resid = np.abs(r - R)

        keep = resid <= np.quantile(resid, 1 - trim_frac)
```

```
        if np.count_nonzero(keep) < 10:
            break

        P = P[keep]

    return cx, cy, R
```

—

A.6.3 Intensity Outside a Fixed Physical Radius

The fraction of optical intensity lying outside a physical diameter of 350 µm is computed after background subtraction using pixels beyond a larger radius.

```
def intensity_fraction_outside(
    img, center, diam_um, scale_um_per_px,
    bg_radius_um=400.0
):
    h, w = img.shape
    x0, y0 = center

    radius_px = (diam_um / 2) / scale_um_per_px
    bg_radius_px = bg_radius_um / scale_um_per_px

    Y, X = np.ogrid[:h, :w]
    r = np.sqrt((X - x0)**2 + (Y - y0)**2)

    bg_mask = r >= bg_radius_px
    if np.any(bg_mask):
        bg_val = np.median(img[bg_mask])
    else:
        bg_val = np.median(img)

    img_corr = np.clip(img - bg_val, 0, None)
```

```
    inside = r <= radius_px
    inside_sum = np.sum(img_corr[inside])
    total_sum  = np.sum(img_corr)

    frac_outside = 1 - inside_sum / total_sum if total_sum > 0 else np.nan
    return 100 * frac_outside
```

—

A.6.4 Bootstrap Estimation of Uncertainty

Uncertainties are estimated using a bootstrap procedure that accounts for uncertainty in the fitted center position, background estimation, and image noise.

```
def outside_intensity_with_uncertainty(
    img, center, diam_um, scale_um_per_px,
    bg_radius_um=400.0,
    n_bootstrap=200,
    center_jitter_px=2.0
):
    h, w = img.shape
    x0, y0 = center

    radius_px = (diam_um / 2) / scale_um_per_px
    bg_radius_px = bg_radius_um / scale_um_per_px

    Y, X = np.ogrid[:h, :w]
    r0 = np.sqrt((X - x0)**2 + (Y - y0)**2)

    outer_mask = r0 >= bg_radius_px
    if not np.any(outer_mask):
        outer_mask = r0 >= np.max(r0) - 1
```

```
outer_vals = img[outer_mask]
bg_sigma = 1.4826 * np.median(
    np.abs(outer_vals - np.median(outer_vals))
)

rng = np.random.default_rng()
frac_samples = []

for _ in range(n_bootstrap):
    dx, dy = rng.normal(0, center_jitter_px, 2)
    cx, cy = x0 + dx, y0 + dy

    bg = np.median(
        rng.choice(
            outer_vals,
            size=min(3000, outer_vals.size),
            replace=True
        )
    )

    noisy = img + rng.normal(0, bg_sigma, size=img.shape)
    img_corr = np.clip(noisy - bg, 0, None)

    r = np.sqrt((X - cx)**2 + (Y - cy)**2)
    inside = r <= radius_px

    inside_sum = np.sum(img_corr[inside])
    total_sum  = np.sum(img_corr)

    frac_samples.append(100 * (1 - inside_sum / total_sum))

frac_samples = np.array(frac_samples)
return np.median(frac_samples), np.std(frac_samples, ddof=1)
```

—

Remarks

All physical length scales are converted to pixel units using independently calibrated pixel-to-micrometer conversion factors. The algorithms are designed to remain robust against finite image size, residual distortions from image rectification, and spatially varying background levels.

A.7 Cavity simulation parameter

The EAM epitaxial intrinsic layer was designed by Owen Moynihan from the III–V Device Group using *Harold* software. The resulting intrinsic layer parameters were used in this work and imported into the *Essential Macleod* thin-film material database to simulate the cavity response under zero-bias conditions and reverse bias of 4 V. In these simulations, the optical properties of the MQW layer are described using the complex refractive index $\tilde{n} = n + ik$, where both the refractive index n and the extinction coefficient k are dimensionless quantities. For reference, the corresponding absorption coefficient α, expressed in units of cm^{-1}, is related to k by $\alpha = 4\pi k/\lambda$.

TABLE A.7.1: Intrinsic layer parameters used for the EAM epitaxial layer design and cavity simulation under zero bias.

Wavelength (nm)	**Refractive index**	**extinction coefficient**
1510	3.6260	0.0960
1520	3.6450	0.0530
1530	3.6270	0.0270
1540	3.6130	0.0180
1550	3.5930	0.0130
1560	3.5900	0.0100
1570	3.5800	0.0080
1580	3.5750	0.0070
1590	3.5690	0.0060
1600	3.5600	0.0050

TABLE A.7.2: Intrinsic layer parameters used for the EAM epitaxial layer design and cavity simulation under reverse bias of 4 V.

Wavelength (nm)	**Refractive index**	**extinction coefficient**
1510	3.55	0.024
1520	3.543	0.0159
1530	3.535	0.0118
1540	3.529	0.0099
1550	3.524	0.0087
1560	3.518	0.077
1570	3.513	0.07
1580	3.503	0.0072
1590	3.5	0.008
1600	3.504	0.01

A.8 Epitaxial layer details of EAM

TABLE A.8.1: Epitaxial EAM stack designed for μTP [88].

Layer	**Material**	**Thickness** (nm)	**Doping** (cm^{-3})
P-contact	InGaAs	50	1×10^{19}
P-cladding	InP	1600	1×10^{18}
Confinement	$Al_{0.4}In_{0.07}Ga_{0.53}As$	10	n.i.d
Confinement	$Al_{0.36}In_{0.11}Ga_{0.53}As$	10	n.i.d
Barrier	$Al_{0.27}In_{0.23}Ga_{0.50}As$	10	n.i.d
Well ($\times$10)	$Al_{0.085}In_{0.305}Ga_{0.61}As$	9.5	n.i.d
Barrier ($\times$10)	$Al_{0.27}In_{0.23}Ga_{0.50}As$	10	n.i.d
Confinement	$Al_{0.36}In_{0.11}Ga_{0.53}As$	170	n.i.d
N-cladding	InP	200	1×10^{18}
Release	InGaAs	100	5×10^{17}
Release	AlInAs	400	5×10^{17}
Substrate	InP	—	1×10^{18}

Appendix B

Appendix

B.1 Per-layer mask design of source

The source wafer fabrication is defined using a seven-layer mask layout, as shown in Figure B.1.1, with each panel corresponding to a lithography mask designed in graphic design system (GDS) format using KLayout softwer to define a specific device layer or process step. In the layout, the coloured regions indicate areas exposed during ultraviolet lithography and subsequently processed by material deposition or etching. Features defined in earlier lithography steps are retained in each layout view to indicate the relative positioning of previously patterned structures with respect to the current mask layer and to identify regions that remain protected by photoresist during the present processing step. Black arrow markers denote the lateral dimensions of the mesa and coupon features defined by the corresponding mask layers.

The layout shown corresponds to a device aperture with a active diameter of 30 µm, and similar layer structures were also designed for active diameters of 20 µm and 10 µm. The individual mask layers define the p-contact and alignment marks, circular mesa, n-contact metallization, coupon outline, encapsulation opening, SiN etch window, and tether geometry required for device release and transfer printing. In the first mask layer, a p-metal alignment mark is defined adjacent to the p-contact region. As shown in Fig. B.1.1 (a), this alignment mark has dimensions of 10 µm × 10 µm and is positioned near the coupon edge with a spacing of 11 µm. This alignment mark serves as a reference feature exclusively for accurate alignment during the transfer-printing process.

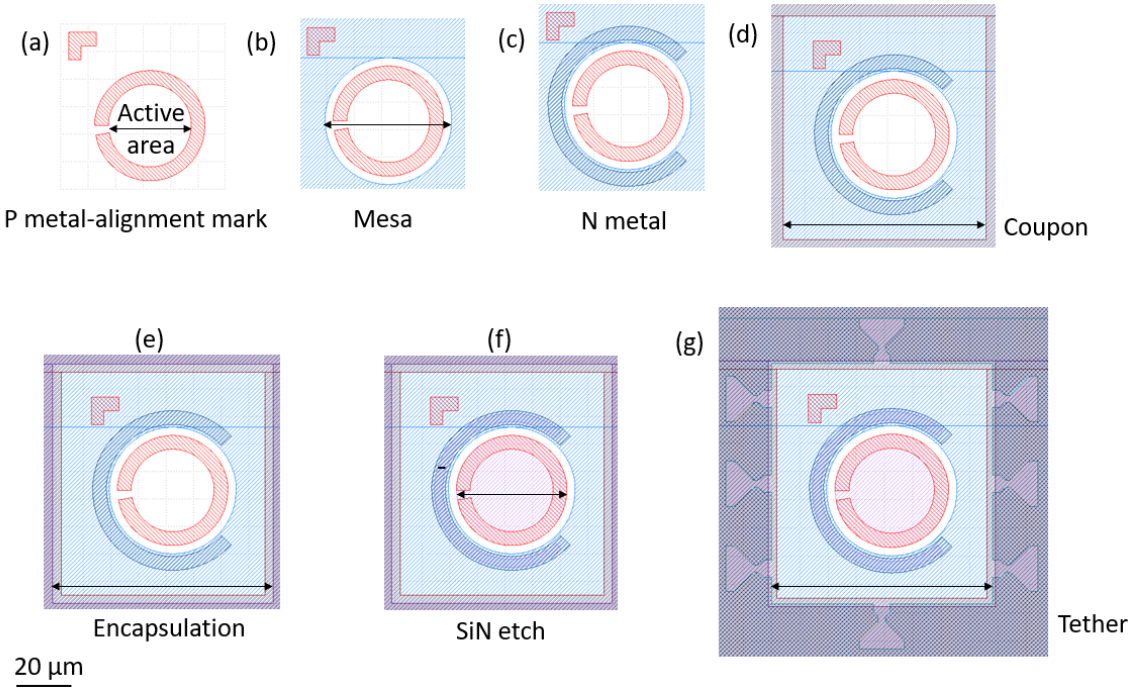


FIGURE B.1.1: Seven-layer lithography mask layout used for source wafer fabrication of the SNEAM device, with panels (a)–(g) showing the sequential mask layers. Coloured regions indicate areas exposed during the corresponding lithography step, while features from previous steps are retained for reference to illustrate layer alignment. Black arrow markers denote the lateral dimensions of the mesa and coupon features. The layouts correspond to a device aperture of 30 µm.

B.2 SNEAM source with tether design

Three tether configurations were incorporated into the coupon layout, as shown in the GDS format in Fig. B.2.1. Coupon designs with two, four, and eight tethers were implemented. In these layouts, regions protected by photoresist during the lithography step are shown as white, while the shaded regions correspond to areas exposed to ultraviolet light and subsequently developed and etched. The indicated dimensions define the tether width and length.

Each tether includes a narrow neck region with a width of 2.5 µm, which defines the intended breaking point during coupon pickup. The wider foot of the tether, as shown in Figure B.2.1, supports the coupon prior to release and prevents collapse following detachment. Among the configurations included in the design, the eight-tether configuration exhibited the most consistent release and pickup performance compared to the four and two tether designs.

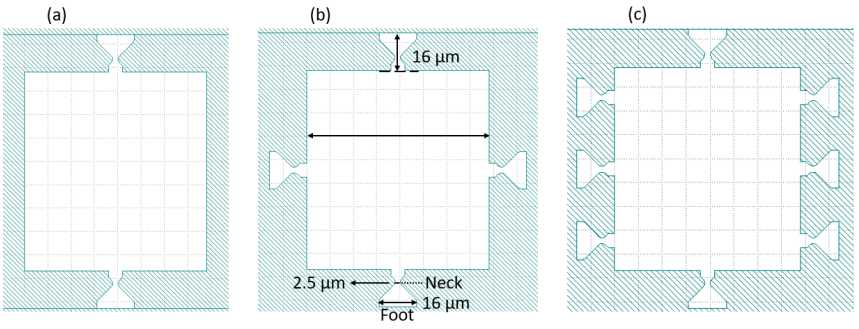


FIGURE B.2.1: GDS mask layouts showing coupon designs with different tether configurations used for source wafer fabrication. From (a)–(c) illustrate coupons incorporating two, four, and eight tethers, respectively. Shaded regions indicate areas exposed during lithography, while unshaded regions represent protected regions.

B.3 Complete source GDS mask overview

The full GDS mask layout shown in Figure B.4.1 incorporates multiple device geometries with active diameters of 10 µm, 20 µm, and 30 µm, combined with n-metal–to–mesa gaps of 2 µm, 3 µm, and 5 µm.

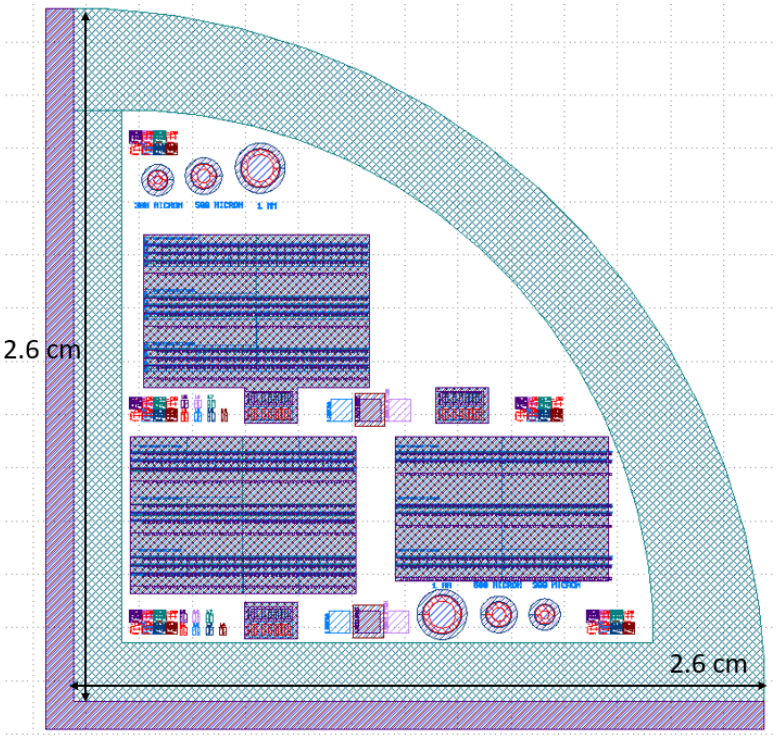


FIGURE B.3.1: Complete GDS mask layout for the SNEAM source wafer, showing the arrangement of multiple device geometry. The layout incorporates devices with different active diameters, n-metal–to–mesa gaps, and tether configurations. The designed mask occupies one quarter of the source wafer.

B.4 GDS mask of target fabrication

The pick and place transfer of coupons from the source wafer to the target wafer is carried out using predefined combinations established in the source mask design and correspondingly incorporated into the target mask layout. This coordinated design approach ensures that coupons with active diameters of 10 µm, 20 µm, and 30 µm are accurately placed at their designated target locations, enabling precise alignment with the corresponding bondpad structures.

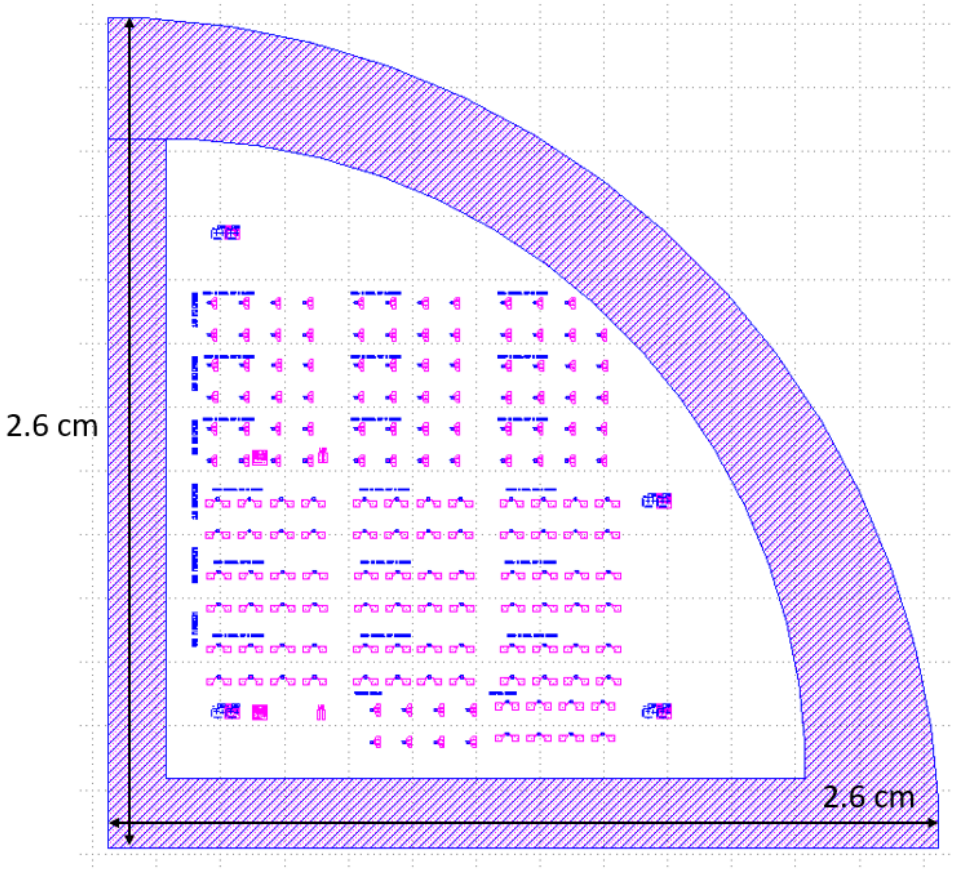


FIGURE B.4.1: Overview of the GDS mask layout for target-wafer fabrication. The mask includes definitions for the bottom reflector as well as GSG and GS bond pads to support multiple device testing and characterization. The designed mask occupies one quarter of the target wafer.

B.5 Source mask design aligned to target pattern

Figure B.5.1 illustrates the alignment of a coupon with an active diameter of 30 µm to the patterned target location using alignment markers defined on both the target wafer and the coupon. During the transfer-printing process, the coupon is first picked up from the source wafer and then translated to the target wafer, where it is positioned relative to the target alignment marker. A designed offset of 3 µm between the bottom reflector pattern on the target and the encapsulation boundary of the coupon is incorporated to facilitate alignment and to enable quantitative assessment of placement accuracy and misalignment during transfer printing.

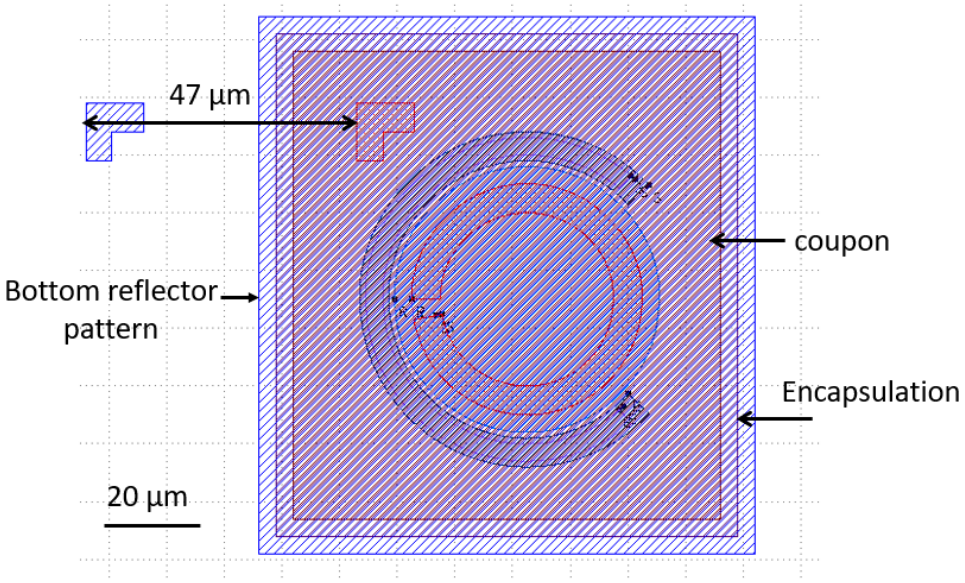


FIGURE B.5.1: Alignment of a source coupon, including the PIN device layout extracted from the GDS mask, with the patterned target location, as targeted during the transfer-printing process and observed after transfer printing.

Bibliography

[1] S. H. Yun and S. J. J. Kwok, "Light in diagnosis, therapy and surgery," Nature Biomedical Engineering **1**, 0008 (2017).

[2] ams OSRAM, "NanEYE2D RGB miniature camera module,", https://ams-osram.com/products/sensor-solutions/cmos-image-sensors/ams-naneye2d-miniature-camera-module, accessed: 26 December 2025.

[3] S. T. Sørensen, W. Messina, L. Niemitz, C. O'Dowling, P. Buszman, S. Andersson-Engels, and R. Burke, "Camera-on-tip endoscope for in vivo cardiovascular diagnostics and surgical guidance," Biomedical Optics Express **16**, 12 (2025).

[4] W. Messina, L. Niemitz, S. Sørensen, C. O'Dowling, P. Buszman, S. Andersson-Engels, and R. Burke, "Design and assembly of a miniature catheter imaging system for In Vivo heart endoscopic imaging," Sensors **24**, 6216 (2024).

[5] M. K. Konings, L. W. Bartels, H. F. Smits, and C. J. Bakker, "Heating around intravascular guidewires by resonating RF waves," Journal of Magnetic Resonance Imaging **12**, 79 (2000).

[6] R. Razavi, D. L. Hill, S. F. Keevil, M. E. Miquel, V. Muthurangu, S. Hegde, K. Rhode, M. Barnett, J. van Vaals, D. J. Hawkes, et al., "Cardiac catheterisation guided by MRI in children and adults with congenital heart disease," The Lancet **362**, 1877 (2003).

[7] T. Rogers, A. E. Campbell-Washburn, R. Ramasawmy, D. K. Yildirim, C. G. Bruce, L. P. Grant, A. M. Stine, A. Kolandaivelu, D. A. Herzka, K. Ratnayaka, et al., "Interventional cardiovascular magnetic resonance: state-of-the-art," Journal of Cardiovascular Magnetic Resonance **25**, 48 (2023).

[8] M. Pekař, J. van Rens, and M. B. van der Mark, "Electrifying catheters with light," Optics Express **25**, 8534 (2017).

[9] J. D. López-Cardona, D. S. Montero, and C. Vázquez, "Smart remote nodes fed by power over fiber in Internet of Things applications," IEEE Sensors Journal **19**, 7328 (2019).

[10] C. Algora, I. García, M. Delgado, R. Peña, C. Vázquez, M. Hinojosa, and I. Rey-Stolle, "Beaming power: Photovoltaic laser power converters for power-by-light," Joule **6**, 340 (2022).

[11] M. Matsuura, "Recent advancement in power-over-fiber technologies," Photonics **8**, 335 (2021).

[12] E. P. Putra, R. Theivindran, H. Hasnul, H. J. Lee, P. J. Ker, M. Z. Jamaludin, R. Awang, and F. A. Mohd Yusof, "Technology update on patent and development trend of power over fiber: a critical review and future prospects," Journal of Photonics for Energy **13**, 011001 (2023).

[13] R. Kashyap, "The fiber fuse - from a curious effect to a critical issue: A 25th year retrospective," Optics Express **21**, 6422 (2013).

[14] Thorlabs, Inc., "DCF13 dispersion compensating fiber specification sheet,", https://www.thorlabs.com/drawings/9c66a3063c1f547e-13DA6F0F-022B-BE6C-3D7571576B854E07/DCF13-SpecSheet.pdf, accessed: 26 December 2025.

[15] F. M. A. Al-Zubaidi, D. S. Montero, and C. Vázquez, "SI-POF supporting power-over-fiber in multi-Gbit/s transmission for In-Home networks," Journal of Lightwave Technology **39**, 112 (2021).

[16] J. D. López-Cardona, R. Altuna, D. S. Montero, and C. Vázquez, "Power over fiber in C-RAN with low power sleep mode remote nodes using SMF," Journal of Lightwave Technology **39**, 4951 (2021).

[17] J. D. López-Cardona, R. Altuna, D. Montero, and C. Vázquez, "Dispersion induced-power fading tuned by power-over-fiber on 5G NR analog radio over fiber fronthaul optical links," 2022 IEEE International Topical Meeting on Microwave Photonics (MWP) pp. 1–4 (2022).

[18] R. Pena and C. Algora, "Semiconductor materials for photovoltaic converters applied to power-by-light systems," Conference on Electron Devices, 2005 Spanish pp. 291–294 (2005).

[19] J.-G. Werthen, S. Widjaja, T.-C. Wu, and J. Liu, "Power over fiber: a review of replacing copper by fiber in critical applications," Optical Technologies for Arming, Safing, Fuzing, and Firing **5871**, 58710C (2005).

[20] O. Höhn, M. Schauerte, P. Schygulla, H. Hauser, D. Lackner, B. Bläsi, and H. Helmers, "Realization of ultrathin GaAs photonic power converters with rear-side metal grating on full 4" wafers," IEEE 49th Photovoltaics Specialists Conference (PVSC) pp. 0038–0042 (2022).

[21] S. J. Wojtczuk, "Long-wavelength laser power converters for optical fibers," Conference Record of the Twenty Sixth IEEE Photovoltaic Specialists Conference pp. 971–974 (1997).

[22] J. F. Geisz, K. L. Schulte, D. J. Friedman, R. M. France, and M. A. Steiner, "Eye-safe 1.5 and 2.0 micron laser power conversion using metamorphic InGaAs photovoltaic devices," Optical Power Delivery **13359**, 1335905 (2025).

[23] V. Andreev, V. Khvostikov, V. Kalinovsky, V. Lantratov, V. Grilikhes, V. Rumyantsev, M. Shvarts, V. Fokanov, and A. Pavlov, "High current density GaAs and GaSb photovoltaic cells for laser power beaming," 3rd World Conference on Photovoltaic Energy Conversion **1**, 761 (2003).

[24] V. P. Khvostikov, S. V. Sorokina, O. A. Khvostikova, N. S. Potapovich, A. V. Malevskaya, M. V. Nakhimovich, and M. Z. Shvarts, "GaSb photovoltaic cells for laser power conversion," AIP Conference Proceedings **2149**, 050007 (2019).

[25] V. P. Khvostikov, S. V. Sorokina, O. A. Khvostikova, R. V. Levin, B. V. Pushnyi, N. K. Timoshina, and V. M. Andreev, "GaSb laser-power ($\lambda = 1550$ nm) converters: Fabrication method and characteristics," Semiconductors **50**, 1338 (2016).

[26] M. Green, J. Zhao, A. Wang, and S. Wenham, "45% efficient silicon photovoltaic cell under monochromatic light," IEEE Electron Device Letters **13**, 317 (1992).

[27] E. Oliva, F. Dimroth, and A. W. Bett, "GaAs converters for high power densities of laser illumination," Progress in Photovoltaics: Research and Applications **16**, 289 (2008).

[28] J. Schubert, E. Oliva, F. Dimroth, W. Guter, R. Loeckenhoff, and A. W. Bett, "High-voltage GaAs photovoltaic laser power converters," IEEE Transactions on Electron Devices **56**, 170 (2009).

[29] S. Fafard, M. C. A. York, F. Proulx, M. Wilkins, C. E. Valdivia, M. Bajcsy, D. Ban, R. Arés, V. Aimez, K. Hinzer, et al., "Ultra-efficient n-junction photovoltaic cells with voc > 14v at high optical input powers," IEEE 43rd Photovoltaic Specialists Conference (PVSC) pp. 2374–2378 (2016).

[30] R. Kimovec, H. Helmers, A. W. Bett, and M. Topič, "Comprehensive electrical loss analysis of monolithic interconnected multi-segment laser power converters," Progress in Photovoltaics: Research and Applications **27**, 199 (2019).

[31] M. Delgado, I. García, M. Hinojosa, and C. Algora, "Design and characterization of multijunction photovoltaic laser power converters for nonuniform irradiance light profiles," Progress in Photovoltaics: Research and Applications **31**, 617 (2023).

[32] S. Fafard and D. Masson, "Vertical multi-junction laser power converters with 61% efficiency at 30 W output power and with tolerance to beam non-uniformity, partial illumination, and beam displacement," Photonics **10**, 940 (2023).

[33] H. Helmers, L. Wagner, C. E. Garza, S. K. Reichmuth, E. Oliva, S. Philipps, D. Lackner, and A. Bett, "Photovoltaic cells with increased voltage output for optical power supply of sensor electronics," Proceedings SENSOR 2015 pp. 519–524 (2015).

[34] P. Doguet, J. Garnier, A. Nieuwenhuys, C. Godfraind, Y. Botquin, A. Lemaire, J. Justice, A. Nonclercq, R. E. Tahry, B. Corbett, et al., "An optoelectronic implantable neurostimulation platform allowing full MRI safety and optical sensing and communication," Scientific Reports **14**, 11110 (2024).

[35] S. Fafard and D. P. Masson, "74.7% efficient GaAs-based laser power converters at 808 nm at 150 K," Photonics **9** (2022).

[36] A.-C. Wang, Y.-R. Sun, S.-Z. Yu, J.-J. Yin, W. Zhang, J.-S. Wang, Q.-X. Fu, Y.-H. Han, J. Qin, and J.-R. Dong, "Characteristics of 1520nm InGaAs multijunction laser power converters," Applied Physics Letters **119**, 243902 (2021).

[37] F. M. A. Al-Zubaidi, J. D. López Cardona, D. S. Montero, and C. Vázquez, "Optically Powered Radio-Over-Fiber Systems in Support of 5G Cellular Networks and IOT," Journal of Lightwave Technology **39**, 4262 (2021).

[38] S. Fafard and D. Masson, "67.5% efficient InP-based laser power converters at 1470 nm at 77 k," Photonics **11** (2024).

[39] V. Prajzler and M. Zikmund, "Power over fiber system using high-power laser source operating at 1470 nm with maximum power 2.0 W for powering to distance up to 5855 m," Optical Fiber Technology **88**, 104033 (2024).

[40] B. C. DeLoach, R. C. Miller, and S. Kaufman, "Sound alerter powered over an optical fiber," The Bell System Technical Journal **57**, 3309 (1978).

[41] G. Bottger, M. Dreschmann, C. Klamouris, M. Hubner, M. Roger, A. W. Bett, T. Kueng, J. Becker, W. Freude, and J. Leuthold, "An optically powered video camera link," IEEE Photonics Technology Letters **20**, 39 (2008).

[42] C. Diouf, V. Quintard, L. Ghisa, M. Guegan, A. Pérennou, L. Gautier, M. Tardivel, S. Barbot, V. Dutreuil, and F. Colas, "Design, characterization, and test of a versatile single-mode power-over-fiber and communication system for seafloor observatories," IEEE Journal of Oceanic Engineering **45**, 656 (2020).

[43] R. Hamié, L. Ghisa, A. Pérennou, V. Quintard, M. Guegan, M. Fadlallah, and A. Hamié, "Experimental characterization of an improved power-over-fiber system for seafloor applications," Engineering Research Express **1**, 015011 (2019).

[44] H. Helmers, C. Armbruster, M. von Ravenstein, D. Derix, and C. Schöner, "6-W optical power link with integrated optical data transmission," IEEE Transactions on Power Electronics **35**, 7904 (2020).

[45] J. D. López Cardona, P. C. Lallana, R. Altuna, A. Fresno-Hernández, X. Barreiro, and C. Vázquez, "Optically feeding 1.75 W with 100 m MMF in efficient C-RAN front-hauls with sleep modes," Journal of Lightwave Technology **39**, 7948 (2021).

[46] M. Matsuura, H. Furugori, and J. Sato, "60 W power-over-fiber feed using double-clad fibers for radio-over-fiber systems with optically powered remote antenna units," Optics Letters **40**, 5598 (2015).

[47] N. Tajima, D. Kamiyama, and M. Matsuura, "150-Watt power-over-fiber feed for bidirectional radio-over-fiber systems using a double-clad fiber," Optical Fiber Communications Conference and Exhibition (OFC) pp. 1–3 (2019).

[48] J. D. López-Cardona, S. Rommel, E. Grivas, D. S. Montero, M. Dubov, D. Kritharidis, I. Tafur-Monroy, and C. Vázquez, "Power-over-fiber in a 10 km long multicore fiber link within a 5G fronthaul scenario," Optics Letters **46**, 5348 (2021).

[49] C. Vázquez, J. D. López-Cardona, P. C. Lallana, D. S. Montero, F. M. A. Al-Zubaidi, S. Pérez-Prieto, and I. P. Garcilópez, "Multicore fiber scenarios supporting power over fiber in radio over fiber systems," IEEE Access **7**, 158409 (2019).

[50] M. Matsuura, A. Ikukawa, H. Kuboki, and Y. Kawamura, "Investigation of crosstalk between data signals and feed light in power-over-fiber," Photonics **9** (2022).

[51] R. Altuna, Y. Jung, P. Petropoulos, and C. Vázquez, "Power over fiber and analog radio over fiber simultaneous transmission over long distance in single mode, multicore, and hollow core fibers," Laser & Photonics Reviews **18**, 2400157 (2024).

[52] A. Ahnood, R. Cheriton, A. Bruneau, J. A. Belcourt, J. P. Ndabakuranye, W. Lemaire, R. Hilkes, R. Fontaine, J. P. D. Cook, K. Hinzer, et al., "Laser driven miniature diamond implant for wireless retinal prostheses," Advanced Biosystems **4**, 2000055 (2020).

[53] M. J. Mack, "Minimally invasive and robotic surgery," JAMA **285**, 568 (2001).

[54] A. Frank, J. Anders, J. Burghartz, B. Kootte, J. Schleipen, and P. Jutte, "An integrated optical transceiver circuit for power delivery and Bi-directional data communication in a medical catheter device," IEEE 48th European Solid State Circuits Conference (ESSCIRC) pp. 185–188 (2022).

[55] S. K. V. Sekar, M. Baskaran, H. Ma, M. Rensing, K. Gradkowski, A. Khan, C. Antony, P. D. Townsend, B. Corbett, and S. Andersson-engels, "All optically powered chip-on-tip microcamera for surgical guidance," Frontiers in Optics + Laser Science 2023 (FiO, LS) p. JTu5A.83 (2023).

[56] E. Thrush, O. Levi, W. Ha, G. Carey, L. Cook, J. Deich, S. Smith, W. Moerner, and J. Harris, "Integrated semiconductor vertical-cavity surface-emitting lasers and PIN photodetectors for biomedical fluorescence sensing," IEEE Journal of Quantum Electronics **40**, 491 (2004).

[57] J. Ingham, R. Penty, and I. White, "Bidirectional multimode-fiber communication links using dual-purpose vertical-cavity devices," Journal of Lightwave Technology **24**, 1283 (2006).

[58] N. H. Zhu, Z. Shi, Z. K. Zhang, Y. M. Zhang, C. W. Zou, Z. P. Zhao, Y. Liu, W. Li, and M. Li, "Directly modulated semiconductor lasers," IEEE Journal of Selected Topics in Quantum Electronics **24**, 1 (2018).

[59] S. Grillanda, T.-C. Hu, D. Neilson, and M. Earnshaw, "Low-voltage surface-normal electroabsorption modulators," Opt. Lett. **46**, 5425 (2021).

[60] I. Rey-Stolle, P. Martín, A. Cano, and I. García, "Germanium laser power converters at 1550 nm with efficiencies over 30%," Solar RRL **9**, e202500625 (2025).

[61] R. Kimovec, H. Helmers, A. W. Bett, and M. Topič, "Power loss mechanisms in small area monolithic-interconnected photovoltaic modules," Opto-Electronics Review **26**, 158 (2018).

[62] R. Pena and C. Algora, "Evaluation of mismatch and non-uniform illumination losses in monolithically series-connected GaAs photovoltaic converters," Progress in Photovoltaics: Research and Applications **11**, 139 (2003).

[63] L. Wagner, A. W. Bett, and H. Helmers, "On the alignment tolerance of photovoltaic laser power converters," Optik **131**, 287 (2017).

[64] M. Matsuura, "Power-over-fiber using double-clad fibers," Journal of Lightwave Technology **40**, 3187 (2022).

[65] H. Ma, H. Cheng, W. Zhang, L. Liu, and Y. Wang, "Generation of a hollow laser beam by a multimode fiber," Chinese Optics Letters **5**, 460 (2007).

[66] C. Zhao, Y. Cai, F. Wang, X. Lu, and Y. Wang, "Generation of a high-quality partially coherent dark hollow beam with a multimode fiber," Optics Letters **33**, 1389 (2008).

[67] G. Zhou, "Analytical vectorial structure of controllable dark-hollow beams close to the source," J. Opt. Soc. Am. B **26**, 2386 (2009).

[68] B. Neupane, F. Chen, W. Sun, D. T. Chiu, and G. Wang, "Tuning donut profile for spatial resolution in stimulated emission depletion microscopy," Review of Scientific Instruments **84**, 043701 (2013).

[69] I. Manek, Y. B. Ovchinnikov, and R. Grimm, "Generation of a hollow laser beam for atom trapping using an axicon," Optics communications **147**, 67 (1998).

[70] Z. Cheng-Liang, L. Xuan-Hui, and C. He, "Study of dark-hollow beams generated with different multimode fibres," Chinese Physics Letters **25**, 1676 (2008).

[71] Thorlabs, Inc., "Multimode fiber beam laboratory fact sheet,", https://www.thorlabs.com/images/TabImages/Multimode_Fiber_Beam_Lab_Fact.pdf, accessed: 26 December 2025.

[72] M. Schauerte, O. öhn, T. Wierzkowski, G. Keller, and H. Helmers, "4-junction GaAs based thin film photonic power converter with back surface reflector for medical applications," IEEE 48th Photovoltaic Specialists Conference (PVSC) pp. 1954–1959 (2021).

[73] S. Grillanda, T.-C. Hu, D. Neilson, N. Basavanhally, Y. Low, H. Safar, M. Cappuzzo, R. Kopf, A. Tate, G. Raybon, et al., "107 Gb/s ultra-high speed, surface-normal electroabsorption modulator devices," Journal of Lightwave Technology **38**, 804 (2020).

[74] S. Grillanda, N. Basavanhally, T.-C. Hu, R. Papazian, M. Cappuzzo, A. Tate, M. Earnshaw, R. Kopf, and F. Pardo, "Optical packaging of surface-normal electroabsorption modulator arrays using passive alignment," IEEE Photonics Technology Letters **37**, 265 (2025).

[75] D. A. B. Miller, D. S. Chemla, T. C. Damen, A. C. Gossard, W. Wiegmann, T. H. Wood, and C. A. Burrus, "Band-edge electroabsorption in quantum well structures: The quantum-confined Stark effect," Phys. Rev. Lett. **53**, 2173 (1984).

[76] D. S. Chemla, T. C. Damen, D. A. B. Miller, A. C. Gossard, and W. Wiegmann, "Electroabsorption by Stark effect on room-temperature excitons in GaAs/GaAlAs multiple quantum well structures," Applied Physics Letters **42**, 864 (1983).

[77] D. S. Chemla, "Quantum wells for photonics," Physics today **38**, 56 (1985).

[78] G. D. Boyd, D. A. B. Miller, D. S. Chemla, S. L. McCall, A. C. Gossard, and J. H. English, "Multiple quantum well reflection modulator," Applied Physics Letters **50**, 1119 (1987).

[79] R.-H. Yan, R. Simes, and L. Coldren, "Surface-normal electroabsorption reflection modulators using asymmetric Fabry-Perot structures," IEEE Journal of Quantum Electronics **27**, 1922 (1991).

[80] R. Yan, R. Simes, and L. Coldren, "Electroabsorptive fabry-perot reflection modulators with asymmetric mirrors," IEEE Photonics Technology Letters **1**, 273 (1989).

[81] C. C. Barron, C. J. Mahon, B. J. Thibeault, and L. A. Coldren, "Design, fabrication and characterization of high-speed asymmetric Fabry-Perot modulators for optical interconnect applications," Optical and Quantum Electronics **25**, S885 (1993).

[82] E. H. Edwards, R. M. Audet, E. T. Fei, S. A. Claussen, R. K. Schaevitz, E. Tasyurek, Y. Rong, T. I. Kamins, J. S. Harris, and D. A. B. Miller, "Ge/SiGe asymmetric fabry-perot quantum well electroabsorption modulators," Optics Express **20**, 29164 (2012).

[83] M. Whitehead, G. Parry, A. Rivers, and J. S. Roberts, "Multiple quantum-well asymmetric Fabry-Perot Etalons for high-contrast, low-insertion-loss optical modulation," Photonic Switching, Technical Digest Series p. QWD15 (1989).

[84] S. Grillanda, C. Tran, D. Che, T.-C. Hu, N. Basavanhally, R. Papazian, R. Kopf, A. Tate, M. Cappuzzo, M. Earnshaw, et al., "4× 53 Gbit/s electro-optic engine with a surface-normal electroabsorption modulator array," IEEE Photonics Technology Letters **35**, 426 (2023).

[85] E. H. Edwards, R. M. Audet, Y. Rong, S. A. Claussen, R. K. Schaevitz, E. Taşyürek, S. Ren, T. I. Kamins, J. S. Harris, D. A. Miller, et al., "Si-Ge surface-normal asymmetric Fabry-Perot quantum-confined Stark effect electroabsorption modulator," in Proc. IEEE Photonics Society Summer Topical Meetings, pp. 211–212 (2010).

[86] G. Roelkens, J. Zhang, L. Bogaert, E. Soltanian, M. Billet, A. Uzun, B. Pan, Y. Liu, E. Delli, D. Wang, et al., "Present and future of micro-transfer printing for heterogeneous photonic integrated circuits," APL Photonics **9**, 010901 (2024).

[87] B. Corbett, R. Loi, W. Zhou, D. Liu, and Z. Ma, "Transfer print techniques for heterogeneous integration of photonic components," Progress in Quantum Electronics **52**, 1 (2017).

[88] O. Moynihan, S. Ghosh, S. Chugh, K. Thomas, J. O'Callaghan, F. B. Atar, B. Roycroft, R. Patel, C. Antony, P. Townsend, et al., "Micro-transfer printed high-speed InP-based electro-absorption modulator on silicon-on-insulator," Applied Physics Letters **125**, 051102 (2024).

[89] refractiveindex.info, "Refractive index of Si_3N_4 (Luke et al.),", https://refractiveindex.info/?shelf=main&book=Si3N4&page=Luke, accessed: 26 December 2025.

[90] T. Tanigawa, T. Onishi, S. Nagai, and T. Ueda, "12.5-Gbps operation of 850-nm vertical-cavity surface-emitting lasers with reduced parasitic capacitance by BCB planarization technique," IEEE Journal of Quantum Electronics **42**, 785 (2006).

[91] D. Neilson, J. Ehrlich, A. Walker, A. Dann, M. Fisher, M. Salter, and I. Reid, "Thermally stable optical bistability in an InGaAs/InGaAlAs etalon at 1.5 µm wavelength," Electronics Letters **29**, 1374 (1993).

[92] D. Chemla, D. Miller, and P. Smith, "Nonlinear optical properties of GaAs/GaAlAs multiple quantum well material: Phenomena and applications," Optical Engineering **24**, 556 (1985).

[93] Y. H. Lee, B. Rhee, A. Chavez-Pirson, H. M. Gibbs, A. Gossard, and W. Wiegmann, "Direct measurement of dispersive nonlinearities in GaAs," Appl. Phys. Lett. **49**, 1505 (1986).

[94] S. Grillanda, T.-C. Hu, D. Neilson, and M. Earnshaw, "Power insensitive surface-normal electroabsorption modulators," Optics Letters **45**, 4472 (2020).

[95] K.-K. Law, J. Mertz, and L. A. Coldren, "Superlattice surface-normal asymmetric Fabry-Perot reflection modulators: optical modulation and switching," IEEE journal of quantum electronics **29**, 727 (1993).

[96] A. Khan, M. Baskaran, O. Moynihan, C. Antony, J. O'Callaghan, B. Roycroft, K. Thomas, E. Pelucchi, S. K. V. Sekar, S. Andersson-Engels, et al., "Half duplex transmission with asymmetric surface normal electro absorption modulator-based optical transceiver for camera-on-tip surgical endoscopes," Optics Express **33**, 31181 (2025).

[97] A. Ghods, D. Sandquist, K. Tatah, M. Dummer, G. Xu, E. Ambrosius, J. Ren, and K. Johnson, "Design, fabrication, and characterization of multi-junction micro-photovoltaic devices," Proc. SPIE **12416**, 34 (2023).